

# Advances in Nanoporous Materials

Guest Editors: Krishna Kant, Gurvinder Singh, and Mahaveer Kurkuri





---

# **Advances in Nanoporous Materials**

Journal of Nanomaterials

---

## **Advances in Nanoporous Materials**

Guest Editors: Krishna Kant, Gurvinder Singh,  
and Mahaveer Kurkuri



---

Copyright © 2016 Hindawi Publishing Corporation. All rights reserved.

This is a special issue published in "Journal of Nanomaterials." All articles are open access articles distributed under the Creative Commons Attribution License, which permits unrestricted use, distribution, and reproduction in any medium, provided the original work is properly cited.

## Editorial Board

- Domenico Acierno, Italy  
Katerina Aifantis, USA  
Nageh K. Allam, USA  
Margarida Amaral, Portugal  
Martin Andersson, Sweden  
Raul Arenal, Spain  
Ilaria Armentano, Italy  
Vincenzo Baglio, Italy  
Lavinia Balan, France  
Thierry Baron, France  
Andrew R. Barron, USA  
Hongbin Bei, USA  
Daniel Bellet, France  
Stefano Bellucci, Italy  
Enrico Bergamaschi, Italy  
Samuel Bernard, France  
D. Bhattacharyya, New Zealand  
Sergio Bietti, Italy  
Giovanni Bongiovanni, Italy  
Theodorian Borca-Tasciuc, USA  
Mohamed Bououdina, Bahrain  
Torsten Brezesinski, Germany  
C. Jeffrey Brinker, USA  
Christian Brosseau, France  
Philippe Caroff, Australia  
Victor M. Castaño, Mexico  
Albano Cavaleiro, Portugal  
Bhanu P. S. Chauhan, USA  
Shafiu Chowdhury, USA  
Jin-Ho Choy, Republic of Korea  
Kwang-Leong Choy, UK  
Yu-Lun Chueh, Taiwan  
Elisabetta Comini, Italy  
Giuseppe Compagnini, Italy  
David Cornu, France  
Miguel A. Correa-Duarte, Spain  
P. Davide Cozzoli, Italy  
Shadi A. Dayeh, USA  
Luca Deseri, USA  
Yong Ding, USA  
Philippe Dubois, Belgium  
Zehra Durmus, Turkey  
Joydeep Dutta, Oman  
Ali Eftekhari, USA  
Samy El-Shall, USA
- Ovidiu Ersen, France  
Claude Estournès, France  
Andrea Falqui, KSA  
Matteo Ferroni, Italy  
Ilaria Fratoddi, Italy  
Alan Fuchs, USA  
Miguel A. Garcia, Spain  
Siddhartha Ghosh, Singapore  
P. K. Giri, India  
Russell E. Gorga, USA  
Jihua Gou, USA  
Jean M. Greneche, France  
Smrati Gupta, Germany  
Kimberly Hamad-Schifferli, USA  
Simo-Pekka Hannula, Finland  
Michael Harris, USA  
Yasuhiko Hayashi, Japan  
F. Hernandez-Ramirez, Spain  
Michael Z. Hu, USA  
Nay Ming Huang, Malaysia  
Shaoming Huang, China  
Zafar Iqbal, USA  
Balachandran Jeyadevan, Japan  
Xin Jiang, Germany  
Rakesh Joshi, Australia  
J.-won Kang, Republic of Korea  
Hassan Karimi-Maleh, Iran  
Antonios Kelarakis, UK  
Alireza Khataee, Iran  
Ali Khorsand Zak, Iran  
Philippe Knauth, France  
Ralph Krupke, Germany  
Christian Kübel, Germany  
Prashant Kumar, UK  
Eric Le Bourhis, France  
Jun Li, Singapore  
Meiyong Liao, Japan  
Shijun Liao, China  
Silvia Licoccia, Italy  
Wei Lin, USA  
Nathan C. Lindquist, USA  
Zainovia Lockman, Malaysia  
Nico Lovergine, Italy  
Jim Low, Australia  
Jue Lu, USA
- Ed Ma, USA  
Laura M. Maestro, Spain  
Gaurav Mago, USA  
Muhamamd A. Malik, UK  
Devanesan Mangalaraj, India  
Francesco Marotti de Sciarra, Italy  
Sanjay R. Mathur, Germany  
Tony McNally, UK  
Yogendra Mishra, Germany  
Paulo Cesar Morais, Brazil  
Paul Munroe, Australia  
Jae-Min Myoung, Republic of Korea  
Rajesh R. Naik, USA  
Albert Nasibulin, Russia  
Toshiaki NatsUKi, Japan  
Koichi Niihara, Japan  
Natalia Noginova, USA  
Sherine Obare, USA  
Won-Chun Oh, Republic of Korea  
Atsuto Okamoto, Japan  
Abdelwahab Omri, Canada  
Ungyu Paik, Republic of Korea  
Piersandro Pallavicini, Italy  
Edward A. Payzant, USA  
Alessandro Pegoretti, Italy  
Ton Peijs, UK  
Oscar Perales-Pérez, Puerto Rico  
Jorge Pérez-Juste, Spain  
Alexey P. Popov, Finland  
Philip D. Rack, USA  
Peter Reiss, France  
Orlando Rojas, USA  
Marco Rossi, Italy  
Ilker S. Bayer, Italy  
Cengiz S. Ozkan, USA  
Sudipta Seal, USA  
Shu Seki, Japan  
Vladimir Šepelák, Germany  
Huaiyu Shao, Japan  
Prashant Sharma, USA  
Donglu Shi, USA  
Bhanu P. Singh, India  
Surinder Singh, USA  
Vladimir Sivakov, Germany  
Adolfo Speghini, Italy



---

Marinella Striccoli, Italy  
Xuping Sun, KSA  
Ashok K. Sundramoorthy, USA  
Angelo Taglietti, Italy  
Bo Tan, Canada  
Leander Tapfer, Italy  
Valeri P. Tolstoy, Russia  
Muhammet S. Toprak, Sweden  
R. Torrecillas, Spain  
Achim Trampert, Germany

Takuya Tsuzuki, Australia  
Tamer Uyar, Turkey  
Bala Vaidhyanathan, UK  
Luca Valentini, Italy  
Rajender S. Varma, USA  
Ester Vazquez, Spain  
Ajayan Vinu, Australia  
Ruibing Wang, Macau  
Shiren Wang, USA  
Yong Wang, USA

Magnus Willander, Sweden  
Ping Xiao, UK  
Zhi Li Xiao, USA  
Yangchuan Xing, USA  
Doron Yadlovker, Israel  
Yoke K. Yap, USA  
Kui Yu, Canada  
William Yu, USA  
Michele Zappalorto, Italy  
Renyun Zhang, Sweden

# Contents

---

## **Advances in Nanoporous Materials**

Krishna Kant, Gurvinder Singh, and Mahaveer Kurkuri  
Volume 2016, Article ID 4350952, 2 pages

## **Current Trends in Nanoporous Anodized Alumina Platforms for Biosensing Applications**

Ganesan Sriram, Pravin Patil, Mahesh P. Bhat, Raveendra M. Hegde, Kanalli V. Ajeya, Iranna Udachyan, M. B. Bhavya, Manasa G. Gatti, U. T. Uthappa, Gururaj M. Neelgund, Ho-Young Jung, Tariq Altalhi, Madhuprasad, and Mahaveer D. Kurkuri  
Volume 2016, Article ID 1753574, 24 pages

## **Nanoporous Glasses for Nuclear Waste Containment**

Thierry Woignier, Juan Primera, and Jérôme Reynes  
Volume 2016, Article ID 4043632, 10 pages

## **Surface Functionality Features of Porous Silicon Prepared and Treated in Different Conditions**

Yu. M. Spivak, S. V. Mjakin, V. A. Moshnikov, M. F. Panov,  
A. O. Belorus, and A. A. Bobkov  
Volume 2016, Article ID 2629582, 8 pages

## **Microwave-Assisted Solvent-Free Synthesis of Zeolitic Imidazolate Framework-67**

Heng Zhang, Jing Zhong, Guoxiang Zhou, Junliang Wu, Zhenyu Yang, and Xianming Shi  
Volume 2016, Article ID 9648386, 9 pages

## **Porous Gold Films Fabricated by Wet-Chemistry Processes**

Aymeric Pastre, Odile Cristini, Alexandre Boe, Katarzyna Raulin, Bertrand Grimbert, Fernand Chassagneux, Nathalie Rolland, and Remy Bernard  
Volume 2016, Article ID 3536153, 9 pages

## **Template Transfer Nanoimprint for Uniform Nanopores and Nanopoles**

Jianjun Li, Weiwei Zhang, Yujun Song, Weiting Yin, and Tao Zhang  
Volume 2016, Article ID 9354364, 7 pages

## Editorial

# Advances in Nanoporous Materials

**Krishna Kant,<sup>1</sup> Gurvinder Singh,<sup>2</sup> and Mahaveer Kurkuri<sup>3</sup>**

<sup>1</sup>*The Hebrew University of Jerusalem, Jerusalem, Israel*

<sup>2</sup>*Department of Materials Science and Engineering, Norwegian University of Science and Technology (NTNU),  
7491 Trondheim, Norway*

<sup>3</sup>*Centre for Nano & Material Sciences, Jain University, Bangalore, India*

Correspondence should be addressed to Krishna Kant; [kant.krishna@mail.huji.ac.il](mailto:kant.krishna@mail.huji.ac.il)

Received 4 August 2016; Accepted 4 August 2016

Copyright © 2016 Krishna Kant et al. This is an open access article distributed under the Creative Commons Attribution License, which permits unrestricted use, distribution, and reproduction in any medium, provided the original work is properly cited.

Nanoporous materials emerged as potentially promising materials because of their high surface area, tunability in pore sizes, and ease of functionalization, thus finding applications from energy to sensing, devices, and medicine. This special issue is devoted to the recent developments in the synthesis of nanoporous materials that include innovative synthetic routes to fabricate them, structural/morphological characterization, properties, and potential applications in various areas of interest. In the field of nanoporous material, nanoporous silicon and nanoporous thin films are discussed, namely, the influence of wet chemistry and electrochemical methods in the fabrication of these materials. Yu. M. Spivak et al. found that alteration in the surface properties of the silicon results in different features of the material. The obtained results demonstrated a new approach to a wide range adjustment of Si porosity and surface properties to address various specific goals. Also, this work highlighted the surface functionality features of porous silicon prepared and treated in different conditions. The paper by H. Zhang et al. demonstrates a solvent-free approach based on microwave technique for the design of microporous metal-organic framework. This study provides advancement in the synthetic methodology instead of employing traditional wet-chemical based approaches. This paper also opens up the new understanding for the electromagnetic wave absorption capability of metal ions which plays a key role in the successful conversion of reactants to MOFs and merits towards further investigation. A. Pastre et al. presented an integrated approach based on colloidal lithography and electroless deposition technique to

produce porous gold films. By this approach, the porosity of the materials can simply be controlled by varying the diameters of polystyrene beads and deposition materials and can be extended to a wide range of materials. The fabrication of porous gold films by an original “bottom-up” approach through combined PS beads templating and gold electroless deposition methods has been achieved. All the techniques employed in the fabrication of the PGFs are totally wet-chemistry processes. The paper titled “Template Transfer Nanoimprint for Uniform Nanopores and Nanopoles” was presented by J. Li et al. They have demonstrated a simple and large-scale process based on template transfer nanoimprinting method to fabricate Pt nanorods array. This process enables large-scale fabrication of uniform nanostructures (nanopores or nanorods) based on the template transfer process in which both robust metallic amorphous alloys and thermosetting polymers can be used as constructing materials of master moulds. Pt-based materials have already been investigated with very impressive and promising applications in the renewable energy technologies such as fuel cell. The paper by T. Woignier was very focused on the nanoporous glasses for nuclear waste containment. It addresses the problem of the synthesis of new porous matrices in which the reactivity of the chemical species in the matrix is extremely important for the physical properties of the final two-phase materials. This special issue provides a comprehensive update in the field of nanomaterials, especially highlighting the benefits and risks related to the use of nanomaterials. Finally, an extensive review article on nanoporous anodic

alumina (NAA) and various fabrication techniques and their applications in the biosensing area makes this special issue a very important milestone.

*Krishna Kant  
Gurvinder Singh  
Mahaveer Kurkuri*

## Review Article

# Current Trends in Nanoporous Anodized Alumina Platforms for Biosensing Applications

**Ganesan Sriram,<sup>1</sup> Pravin Patil,<sup>1</sup> Mahesh P. Bhat,<sup>1</sup> Raveendra M. Hegde,<sup>1</sup> Kanalli V. Ajeya,<sup>1</sup> Iranna Udachyan,<sup>1</sup> M. B. Bhavya,<sup>1</sup> Manasa G. Gatti,<sup>1</sup> U. T. Uthappa,<sup>1</sup> Gururaj M. Neelgund,<sup>2</sup> Ho-Young Jung,<sup>3</sup> Tariq Altalhi,<sup>4</sup> Madhuprasad,<sup>1</sup> and Mahaveer D. Kurkuri<sup>1</sup>**

<sup>1</sup>Centre for Nano and Material Sciences, Jain University, Jain Global Campus, Bangalore-562 112, Karnataka, India

<sup>2</sup>Department of Chemistry, Prairie View A & M University, Prairie View, TX 77446, USA

<sup>3</sup>Department of Environmental Energy Engineering, Chonnam National University, Gwangju 500-757, Republic of Korea

<sup>4</sup>Department of Chemistry, Faculty of Science, Taif University, Taif, Saudi Arabia

Correspondence should be addressed to Ho-Young Jung; [jungho@chonnam.ac.kr](mailto:jungho@chonnam.ac.kr), Madhuprasad; [madhuprasad@jainuniversity.ac.in](mailto:madhuprasad@jainuniversity.ac.in), and Mahaveer D. Kurkuri; [mahaveer.kurkuri@jainuniversity.ac.in](mailto:mahaveer.kurkuri@jainuniversity.ac.in)

Received 4 March 2016; Revised 24 June 2016; Accepted 11 July 2016

Academic Editor: R. Torrecillas

Copyright © 2016 Ganesan Sriram et al. This is an open access article distributed under the Creative Commons Attribution License, which permits unrestricted use, distribution, and reproduction in any medium, provided the original work is properly cited.

Pristine aluminum (Al) has received great deal of attention on fabrication of nanoporous anodized alumina (NAA) with arrays of nanosized uniform pores with controllable pore sizes and lengths by the anodization process. There are many applications of NAA in the field of biosensors due to its numerous key factors such as ease of fabrication, high surface area, chemical stability and detection of biomolecules through bioconjugation of active molecules, its rapidness, and real-time monitoring. Herein, we reviewed the recent trends on the fabrication of NAA for high sensitive biosensor platforms like bare sensors, gold coated sensors, multilayer sensors, and microfluidic device supported sensors for the detection of various biomolecules. In addition, we have discussed the future prospectus about the improvement of NAA based biosensors for the detection of biomolecules.

## 1. Introduction

In recent years, metal oxide based nanomaterials are emerging in various areas such as thermal barrier [1], gas sensor [2], solar cells [3], drug delivery [4], and biomedical applications [5] due to ease of preparation and possibility in tailoring chemical and physical properties. Nanoporous oxide materials possess tremendous applications in water purification [6], biosensors [7], therapeutics [8], optical sensors [9], oxygen carrier [10], battery technology [11], and bioimaging [12]. Overall, nanoporous anodized alumina (NAA) has several advantages such as high surface area to volume ratio, thermal stability, chemical stability, electrical insulation, formation of unique pore structures, high porosity, self-organized pore structure, being nontoxic and bioactive, and biocompatibility. In addition, systematic arrangement of nanopores is of great interest, especially pores with high aspect ratios between

pore diameters to pore length for various applications such as separation, drug delivery, and biosensing. Due to this, geometrical arrangements of pores with high surface area are promising candidates in biosensing for the detection of extremely rare/important biological entities.

Keller et al. have developed closely packed hexagonally arranged duplex structured NAA with pores and barrier type of oxide layer formation by anodic oxide coating through electrolytes [13]. The most popular fabrication method to synthesis NAA is electrochemical anodization, which has wide variety of applications in areas such as filtration process [14], biosensor [15, 16], drug delivery [17], corrosion resistant [18], oxygen sensor [19], catalysis [20], photocatalytic [21], cancer therapy [22], refractometric [23], interferometric [24], DNA sensor [25], bone implant [26], separation [27], and fluorescence detection [28]. The growth of porous structure depends on the ionic transport in anodic oxides under the

influence of electric field by anodic polarization in a suitable electrolyte. The pore geometry (pore shape and diameter) depends on the processing parameters such as electrolyte solution, pH, anodization voltage, current density, time of anodization, and temperature. However, precise pore diameter formation in the anodization process of pristine aluminum (Al) under applied electric field is completely not understood yet.

Al can be electrochemically anodized by two-step anodization process to get nanopores [29, 30]. In anodization process, its surface is electrochemically oxidized in an electrolyte solution which leads to the formation of an oxide layer. The anodization can be done by applying voltage between an Al electrode (anode) and Pb and/or Pt electrode (cathode) arranged parallel to each other. The electric field is equally dispersed on its surface where pores are created on the surface of NAA [31]. The highly ordered porous structures are fabricated under low temperatures with strong acid electrolyte solutions (oxalic acid, phosphoric acid, and sulfuric acid) which is called the mild anodization process. Further, these self-ordered pore arrangements with narrow size distribution and high aspect ratio can be developed by applying different potentials, for example, at 25 V with sulfuric acid [32], 40 V with oxalic acid [30], and 195 V with phosphoric acid [33] leading to the formation of pores of diameters 65, 100, and 400 nm, respectively. Despite being advantageous to form precise pores, the main disadvantage of mild anodization or self-ordered arrangement is that the rate of oxide growth is slower due to low current density and high processing time. On the other hand, hard anodization process can overcome the drawbacks of mild anodization process where higher current densities and faster processing steps are involved and the whole process is mechanically robust [34]. Recently Losic and Santos reported the fabrication of NAA by soft and hard anodization techniques for structural changes of pores and optical properties for specific sensing applications [35]. However, by using acid solutions porous structures can be created in NAA; on the other hand, by using neutral solutions barrier (nonporous) type of NAA is created [36]. Further, Lee and Park published a review on the formation of structural changes of porous and nonporous (barrier) types of NAA by anodization (Figure 1) [37].

In addition to that, NAA has been used in separation studies such as protein [38], molecular release [39], and transport [27]. This process offers self-organized growth of nanopores from top to bottom which provides highly ordered NAA structure. The fabrication of nanopores in NAA of different structures such as funnel [40], multilayered [41], hierarchical [42], and three-dimensional [43] has also been reported. Recently, Santos et al. developed NAA with inverted funnel structure; this type of multistratified structures of cylindrical nanopores varies in pore diameter from top to bottom [44]. The NAA can also be fabricated in wide variety of nanostructures such as nanotubes, nanofibers [45], and nanodots [46].

Owing to the abovementioned importance and wide range of NAA applications herein, we are reviewing fabrication and applications of NAA in biosensing arena. In this article, the most recent and current research on NAA

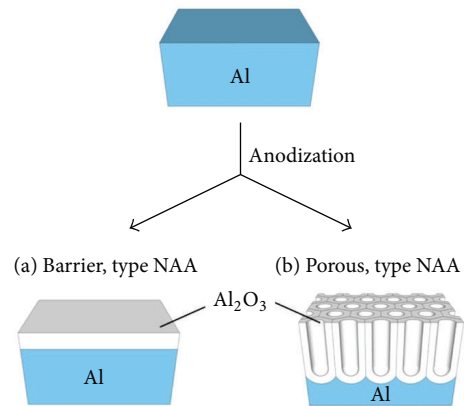


FIGURE 1: Specific diagram of formation of porous and nonporous NAA by Al through anodization process [37].

and gold coated NAA (Au-NAA) with their key role in biosensing applications have been covered. In particular, our focus is on fabrication of NAA by anodization process and their specific applications in biosensing with detailed description on fabrication conditions, working principles, and mechanism of biosensing. Finally, the future prospectus of NAA in the area of biosensing has been discussed.

## 2. Fabrication of Nanoporous Anodized Alumina (NAA)

In general, NAA can be developed by two-step anodization method (Figure 2) [47, 48]. As discussed in Introduction, by varying parameters like applied current, concentration of acid solutions, anodization time, and temperature, one can tailor the NAA properties. For example, Yin et al. used same method [63]; at first the Al film was electrochemically polished in a mixture of ethanol (EtOH) and HClO<sub>4</sub>. In the next step, Al was anodized with 0.3 M oxalic acid at 10°C and at 40 V for few hours to obtain nanoporous structures of NAA. Further, second anodization was carried out in the same way to remove the barrier layer which is created at the bottom of nanopores by using 0.5 M phosphoric acid or by using dry etchants like chlorine-based gases. In this method highly ordered nanopore arrays in thin alumina film on silicon substrate were obtained.

Similarly, Lo and Budiman fabricated NAA by using impure Al foils which can be used in large scale applications whereas the highly pure foils have limited applications in nanoelectrophotonics. The impure Al foil was taken as anode and copper as cathode [64]; further, 5 × 5 mm pieces of impure Al foil were mounted on the glass slides and these were then anodized in 0.3 M oxalic acid for about 18 h at constant voltage of 40 V. The oxidized layer was etched using 0.5 M phosphoric acid at 80°C for 1 h. The same material was anodized by using above conditions for 15 min to develop nanopores throughout the surface. Thus, obtained samples were removed and floated over saturated HgCl<sub>2</sub> and further treated with H<sub>3</sub>PO<sub>4</sub> to remove the deposited barriers to get NAA. To compare, ultrapure Al foils were used and it was found that all the properties such as growth rate and chemical

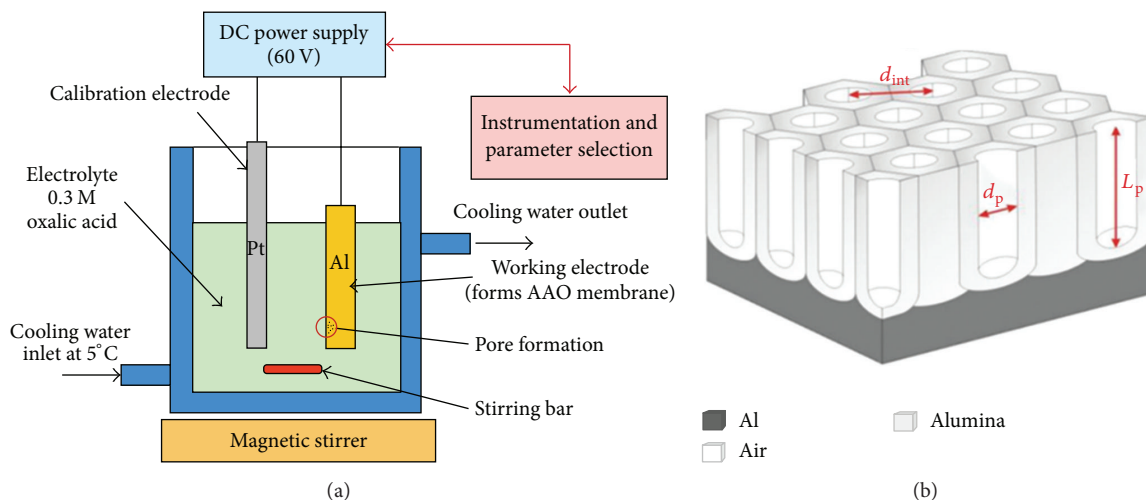


FIGURE 2: (a) Experimental set-up for fabrication of NAA by two-step anodization process and (b) the geometric structure of NAA ( $d_{int}$ : inter-pore distance,  $d_p$ : pore diameter, and  $L_p$ : pore length) [47, 48].

composition were similar with that of NAA produced from impure Al foils except the pore ordering (morphology). However, the pore consistency and order can be controlled by electropolishing the impure Al foil.

Nagaura et al. proposed a multistep anodization and leaching process to get three dimensional structured films [65], in which Al foils were used as working electrode in anodization process and carbon electrode as counter electrode. Each anodization step was followed by dipping the substrate into phosphoric acid for pore widening, which was called leaching process. The anodization was conducted in phosphoric acid solution at 10°C with stirring and varying current to get multistep structures which is followed by leaching process after every anodization step with different time interval of dipping.

Similarly, Hussain et al. fabricated uniform NAA to fabricate tungsten trioxide ( $\text{WO}_3$ ) nanowires [66]. In this process, Al foils were cleaned with acetone to remove the dirt and greases which were further subjected to annealing at 500°C for 5 h at heating rate of 10°C/min. Further, the oxides were removed by dilute oxalic acid and rinsed with deionized water. In next step, electrically polished foils were kept in a mixture of EtOH and perchloric acid at a voltage of 12 V for 3 min at 100°C. Further, two-electrode cell system was used to fabricate NAA using graphite as counter electrode. Anodization was carried out at 40 V for 120 min at 50°C in 0.3 M  $\text{H}_2\text{C}_2\text{O}_4$  electrolyte. The oxide layer of NAA substrate was removed by washing with  $\text{H}_2\text{Cr}_2\text{O}_4$  and  $\text{H}_3\text{PO}_4$  for 30 min. Further, it was again anodized at a voltage of 40 V for 120 min at 50°C in 0.3 M  $\text{H}_2\text{C}_2\text{O}_4$  acid. After this process, NAA was immersed in  $\text{H}_3\text{PO}_4$  for 90 min to increase the size of pore width. The fabricated NAA has been used as a template to fabricate  $\text{WO}_3$  nanowires by electroless deposition bath method. NAA was sonicated under the mixture of  $\text{SnCl}_2$  and HCl in the wt% of 0.3 and 2.5, respectively. However, in this mixture, dissolution of the template was due to prolonged dipping process. On the other hand, NAA was sonicated

under the mixture of  $\text{PdCl}_2$  and HCl used in the wt% of 0.1 and 1, respectively, for 3 min which is followed by dipping the template in deionized water. The deposition bath was used to form nanowires by NAA template in which sodium tungstate, hydrazine hydrate, sodium potassium tartrate, and acetic acid were used as a composition. With this,  $\text{WO}_3$  nanowires were formed in the pores of NAA.

For the formation of unidirectional NAA structures Na et al. [67] used pure 1050 Al sheets after pretreatment to clean the surface before the anodization process. Al samples were anodized in dilute  $\text{H}_2\text{SO}_4$  electrolyte solution using Pt cathode at a current density of 3 A/dm<sup>2</sup>. In the next step, anodization was carried out at different electrolyte temperatures such as 2, 10, and 15°C for 5 to 6 h. After this process, acid resistant tape was removed by acetone washing to form porous structures on surface. The thickness and average diameter of unidirectional nanopore were found to be 230–240  $\mu\text{m}$  and 6–24 nm, respectively.

In another work, the synthesis of carbon nanotubes in NAA film by  $\text{H}_2\text{SO}_4$  or  $\text{H}_2\text{C}_2\text{O}_4$  acid was achieved by Sui et al. [45]. Polished Al plate was anodized at different anodic voltages in 0.16 M  $\text{H}_2\text{C}_2\text{O}_4$  or 1.2 M  $\text{H}_2\text{SO}_4$  solution for 25 min by rigorous stirring at 15°C to get porous NAA template, which was then cleaned and kept for boiling (15 min). Pairs of alumina templates with or without boiling in water were put into tubular stove with gas flow mixture of  $\text{N}_2/\text{C}_2\text{H}_2$  at the rate of 100 mL/min at a particular temperature for 2 h. Further, Al was dissolved in 10% NaOH solution to release nanotubes and nanofibers. Immediately, these were thoroughly washed and dispersed in pure EtOH solution by sonication method to obtain pure nanopore structures in the form of carbon nanotubes on NAA.

Furthermore, Tsuchiya et al. developed self-organized NAA in neutral electrolytes [68]. Al foils (0.5 mm) were degreased by sonicating in acetone, isopropanol, and methanol followed by rinsing in deionized water and dried under nitrogen atmosphere. Anodization was done in

a conventional cell with three electrodes; Pt as counter electrode and Haber-Luggin capillary electrode with Ag/AgCl were as reference electrode. The samples were assembled in electrochemical cell by pressing against an O-ring. The electrolytes such as 1 M  $(\text{NH}_4)_2\text{SO}_4$  solution with fluoride ions and deionized water were used in this experiment. Anodization was done at high voltage potentiostat which consists of potential from open circuit potential to certain fixed potential. Further, the samples were rinsed in deionized water and dried in nitrogen stream. The pore diameter of NAA was obtained at different potentials in acid solutions ranging from 65 to 500 nm.

Fabrication of NAA with ideally ordered channel arrangements was reported by Asoh et al. [69]. In this, the electropolished master mold was placed on pure Al sheet below  $10^\circ\text{C}$  for about 4 min in a mixed solution of  $\text{HClO}_4$  and  $\text{C}_2\text{H}_5\text{OH}$ . An array of concaves on Al surface was formed. Further, anodization of Al was done by 0.3 M  $\text{H}_2\text{SO}_4$  and/or  $\text{H}_2\text{C}_2\text{O}_4$  under constant voltage. Later, anodic oxide film was removed from Al substrate in saturated  $\text{HgCl}_2$  solution. The selective removal of barrier layer (down part of oxide layer) and pore widening were done by etching the NAA membrane in 5 wt%  $\text{H}_3\text{PO}_4$  at  $30^\circ\text{C}$ . This treatment facilitates better observation of the holes at bottom oxide layer, where uniform diameter of channels (40 nm) and depth of the nanopore ( $1\ \mu\text{m}$ ) were formed.

On the other hand, Zhang et al. fabricated NAA membrane using low potential anodizing process [70]. Highly pure Al foils were cut into small pieces and annealed in a furnace in the presence of air at  $600^\circ\text{C}$ . Mixture of acids ( $\text{H}_3\text{PO}_4 : \text{HNO}_3 : \text{H}_2\text{O} = 8 : 1 : 1$ ) was taken and Al plates were polished for 30 s at  $95^\circ\text{C}$  followed by electrochemical polishing in perchloric acid and EtOH (1 : 4 ratio). Anodization was done in  $\text{H}_2\text{SO}_4$  aqueous solution under constant potential of 18 V. The Al plate was fixed in acid solution which was separated from cathode of mechanically polished copper plate. All experiments were conducted in  $3^\circ\text{C}$  cold water using ice bath. The oxide layer was produced at first anodization step and was removed by submerging the Al plate in chromic acid solution. Second anodization was conducted under same conditions by shortening the duration to 3 h. The NAA were obtained with pore diameters ranging from 6.8 to 19.3 nm at potential of 6 to 18 V.

Wang et al. fabricated NAA nanotubes using pulse anodization; the NAA nanotubes were fabricated by modified anodization process, that is, pulse anodization [71]. Al plate was sonicated in EtOH, ultrapure water, and then electropolished in a mixture of EtOH and  $\text{HClO}_4$  4 : 1 (v : v) at  $20^\circ\text{C}$  and  $5^\circ\text{C}$  for 3 min. The first anodization was done in an electrolyte solution of 0.3 M  $\text{H}_2\text{SO}_4$  at 25 V and  $6^\circ\text{C}$ . This consists of mild anodization and hard anodization pulses in 0.3 M  $\text{H}_2\text{SO}_4$  electrolyte and EtOH of concentration ranging from 0 to 25%. Wet chemical etchants were used to remove remaining Al substrates in 0.2 M  $\text{CuCl}_2$  and 6.1 M HCl solution. Through pulse anodization, the pore length and diameters of NAA were found to be 500 and 90 nm, respectively.

Friedman et al. prepared series of highly porous and pure NAA [72]. A flat cell was used with a Pt mesh counter electrode, and the Al was exposed to electrolyte at  $0.25\ \pi\text{cm}^2$ .

At first anodization step, the NAA was anodized for 2 h and kept in 5%  $\text{H}_3\text{PO}_4$ /5% chromic acid solution for overnight which is followed by etching to provide a barrier layer, thus resulting in the formation of small porous structures on the surface of Al. Further, it was reanodized at the same condition as in the first step but with shorter time interval. So, the above methods emphasize the fabrication of different types of NAA with different pore diameters and pore lengths for the detection of immobilized biomolecules on their surface. In addition, these key parameters enhance the optical properties and rapid sensitivity in the detection process of biomolecules. Consequently, the structural parameter and fabrication conditions of the NAA become crucial platform for biosensing application.

### 3. Applications of NAA in Biosensing

Recently, NAA based materials have attracted considerable attention in biosensing due to possibilities like immobilization of target molecules on nanopores, optical sensing enhancement by coating Au layer on NAA surfaces, low concentration detection, biocompatibility with living cells due to Au coating, portability, and so forth. The recent reviews on NAA based biosensing date back to 2014 [73–76]; thus, there is a huge scope for the current review article which covers latest research works and current trends in this particular field. Owing to this, it could help the readers to find recent developments and current trends in NAA based biosensing applications. The following applications are categorized based on the types of transducer for the detection of biomolecules.

### 4. NAA Biosensor

*4.1. Detection of Glucose.* The barcode system enhances the optical biosensing effect of NAA for oxazine dye and glucose using photoluminescence (PL) spectroscopy [77]. Enhancement in the PL barcode system for optical biosensor was observed for NAA structure with wide pore diameter (30–71 nm) and controlled pore length (5–12.4  $\mu\text{m}$ ). The barcodes were produced with respect to different wavelength of PL spectra. The wide pore diameter and controlled pore lengths were obtained by wet chemical etching and various anodization processing times. It was found that PL barcode system depends on the pore diameter and lengths. In a control experiment, no PL spectrum was observed for the pore length larger than 25  $\mu\text{m}$  with 5 h anodization time. In this study pore lengths, such as 5, 8, and 12.4  $\mu\text{m}$ , resulted in better PL intensities. Intensity of PL spectra was increased with wide pore diameter, due to decrease in surface thickness of substrate. However, PL intensity has been decreased while increasing the etching time for longer pore diameters. Further enhancement in PL intensity for larger pore diameter was exhibiting better sensing effect for oxazine dyes and glucose biosensors.

Furthermore, Santos et al. studied the effect of pore length and diameter of NAA for biosensing applications [78]. The study showed effect of pore diameter and pore length with respect to particular reflection in NAA. Samples

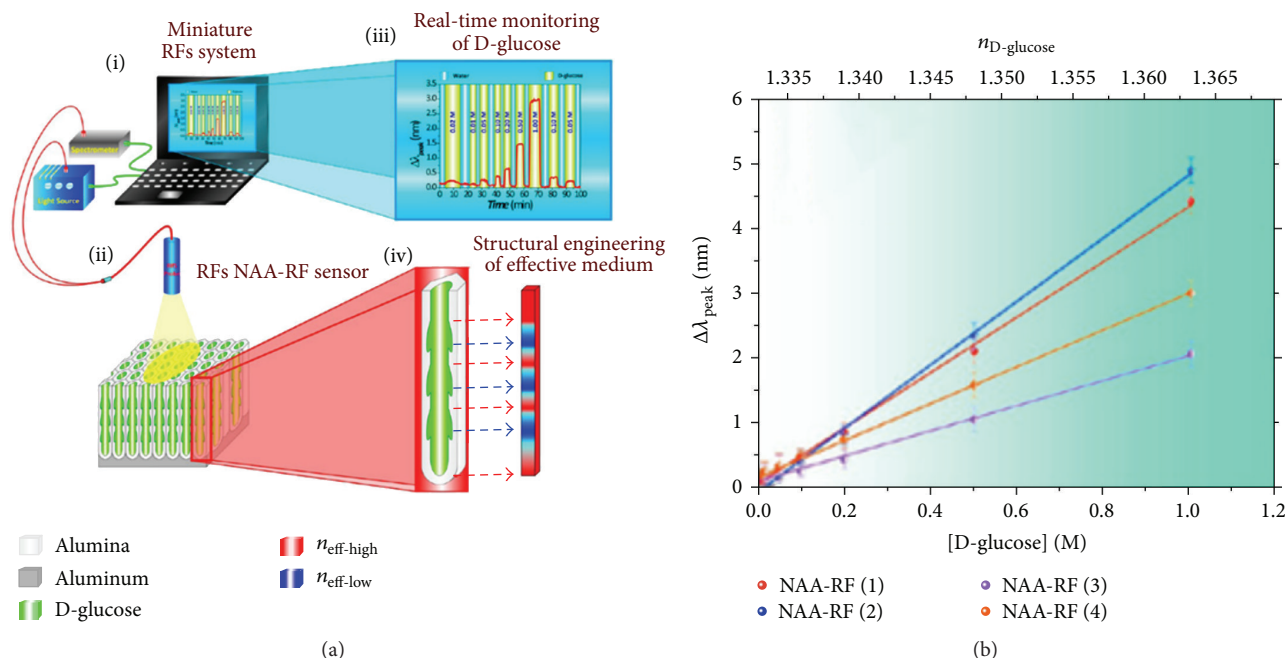


FIGURE 3: (a) Schematic diagram of sensing principle of D-glucose by NAA-RFs using reflection spectroscopy: (i) set-up of reflection spectroscopy combined with light source, spectrometer, and optical probe, (ii) optical sensing platform on NAA-RFs, (iii) real-time monitoring of D-glucose by NAA-RFs system, and (iv) structural nanopore geometry of effective medium; (b) sensing plots at different concentration of D-glucose [15].

with different pore diameters with same pore lengths were considered with same geometrical characteristics. The wider pore showed greater reflectivity due to bigger pore diameter and larger pore gives lower reflectivity due to large pore length. The reflectivity studies have been used to predict the biosensing mechanism of NAA. Furthermore, Santos et al. reported the comparison of biosensor material for the detection of D-glucose and L-cysteine using PL and reflectometric interference spectroscopy (RIfS) [79]. NAA substrate was fabricated by two-step anodization process with pore length and pore diameters of 1.8 to 12.7  $\mu\text{m}$  and 29 to 74 nm, respectively. The detection of D-glucose and L-cysteine under nonspecific and specific adsorption conditions by NAA was carried out using PL and RIfS systems. However, the better sensitivity for both the biomolecules was observed for NAA by PL due to their photoactivity compared to RIfS. Sensing of glucose and L-cysteine was achieved at low concentration by NAA, that is, 0.01 M and 0.005 M, respectively, using PL.

In another work, Kumeria et al. developed NAA rugate filters (NAA-RFs) for real-time detection of D-glucose by reflection spectroscopy with flow cell [15]. Reflection spectroscopy is one of the optical instruments with various benefits such as small size, being portable, and low cost, compared to other optical instruments. Four different types of NAA rugates, that is, NAA-RF 1, NAA-RF 2, NAA-RF 3, and NAA-RF 4, were fabricated. The detection of D-glucose in flow cell was observed by change in refractive index (RI) of NAA rugate filter with respect to adsorption of D-glucose into nanopores. The RI was measured initially by

using distilled water which was sent into flow cell followed by D-glucose solution. Further, this D-glucose was immobilized on NAA-RF 1 where RI has been increased for D-glucose and decreased for distilled water. Similar procedure was applied for other three NAA rugate filters. However, better sensitivity was found for NAA-RF 2 compared to other three NAA-RFs materials for D-glucose. The schematic diagram explains the optical system for detection of D-glucose by combining NAA-RFs and reflection spectroscopy and sensing plot for different concentration of D-glucose with respect to change in effective RI of NAA-RFs using reflection spectroscopy (Figure 3).

**4.2. Detection of Binding of Antibody and Antigen.** Takmakov et al. fabricated NAA for the detection of streptavidin through covalently bonded biotin on sensor surface using fluorescence microscopy [80]. By using aminosilane-succinimide chemistry [81], the biotin molecules were immobilized covalently on NAA surface. Fluorescence microscopy was used to detect streptavidin molecules on biotin bonded sensor surface. The fabrication process and sensing mechanism are explained as follows: Al film was coated on glass substrate through mask by ion beam coater with film thickness of around 600 nm. The anodized Al film showed pore diameter and thickness of 20 nm and 60  $\mu\text{m}$ , respectively. The biotin molecules were immobilized on sensor surface by NAA which were rinsed in 3-aminopropyltriethoxysilane (APTES) and later washed with acetone followed by drying in oven. Biotin layer was formed on sensor surface by mixing with dimethyl sulfoxide (DMSO) solution of biotin N-hydroxysuccinimide ester and acetone. The covalently

bonded biotins were analyzed on surface by FTIR. Further, biotinylated substrate was exposed to streptavidin modified Alexa Fluor 488 dye solution for 5 min. The unbound streptavidin on biotinylated substrate was removed by further washing with phosphate-buffered saline (PBS) solutions. The streptavidin bounded biotin NAA substrate was immersed into water and then analyzed by fluorescence microscope to confirm the binding of biomolecules. The streptavidin molecules were exposed to both materials in which the fluorescence contrast was high for NAA compared to Al film due to high diffusion of streptavidin into porous structured NAA. The sensing of streptavidin was carried out by using fluorescence microscopy where significant increase in fluorescent intensity was observed for NAA (black line) due to covalent bonding of streptavidin-biotin on sensor surface and moreover biomolecular diffusion process was higher in porous surface. In contrast, Al film exhibited very low intensity peaks due to improper binding of biomolecules and was having less diffusion due to nonporous structure of bare metal film.

Fu et al. developed NAA based biosensor for the detection of antigen-antibody detection using SERS method [82]. NAA was developed by the process of Al thin film coated on glass substrate with thickness of 380 nm by thermal evaporation technique and followed by anodization process. Further, silver (Ag) nanoparticles were coated on the surface of NAA to enhance the RI of medium. The immobilized antigen-antibody was obtained on modified NAA substrate by washing with APTES solution followed by GTA solution for the formation of amino and aldehyde groups, respectively. The detection of antigen-antibody recognition on NAA was observed by wave guide assisted SERS system. The obtained human IgG (antigen) was covalently bound with NAA surface followed by FITC-anti-IgG (antibody) which were allowed to immobilize with human IgG modified NAA surface. The immobilization of molecules was analyzed by change in angle dependent reflectivity on NAA surface. The angle dependent reflectivity studies were obtained by processing bare NAA substrate at angle  $44.74^\circ$ , human IgG modified NAA surface has angle of  $45.04^\circ$ , and at the end of FITC-anti IgG modified NAA the angle was  $44.42^\circ$ . The above results show that the angle dependent reflectivity increases with respect to excess binding of molecules on NAA surface. The detection of binding molecules on NAA surface was analyzed by enhanced SERS signals through Ag nanoparticles accumulation.

Kant et al. developed biosensing platform by utilizing the pore dimension of NAA to detect the immobilization of streptavidin (antibody) with biotin (antigen) by electrochemical impedance spectroscopy [49]. NAA has been fabricated with 25–65 nm and 4–18  $\mu\text{m}$  pore size and lengths, respectively. In addition, nanopore arrays were patterned on back side of substrate by photolithographic process. The streptavidin biomolecules were bound on nanopore array structure of NAA surface by soaking it in mixture of streptavidin with PBS solution. The different concentration solutions of biotin molecules were allowed to bind on streptavidin functionalized substrate. However, 0.2  $\mu\text{M}$  concentration of biotin molecules bound with streptavidin showed better

sensing performance due to decrease in pore resistance on substrates and increase in pore diameter from 25 to 65 nm. It has been found that sensitivity has not only depended on pore dimensions where size of biomolecules may also influence the enhancement of sensing performance. The size of immobilized biomolecule of streptavidin was about 4–5 nm and the size increased to 6–8 nm due to binding with biotin molecule which resulted in better performance. The electrochemical impedance spectroscopy was performed by four electrode systems to characterize the NAA biosensor. The electrochemically impedance biosensor performed by change in surface charge of NAA binding to both biomolecule and pore resistance of substrate. Two gold foils as working and counter electrodes with Ag/AgCl were used as a reference electrode. The NAA substrate was sandwiched between two cells and contacted to reference electrode from each side of cells. The working and counter electrodes were placed at the end of two cells. An equivalent circuit was used to balance the resistance and capacitance of the NAA to analyze the streptavidin bonded biotin on NAA. The sensitivity of NAA has been enhanced by decreasing pore resistance with respect to change in conductivity of sensor surface. The larger pores with longer pore length are not suitable for the detection of biomolecules. Thus, the pore resistance increased when the pore length was increased from 4.5 to 18  $\mu\text{m}$ . The pore resistance depends on the pore length and it was found that no response/sensitivity was observed for the pore length above 10  $\mu\text{M}$ . The detection limit was observed using different solutions of biotin in the range of 0.2 to 10  $\mu\text{M}$  by binding with streptavidin on NAA substrate, but in the concentration of 0.2  $\mu\text{M}$  it showed better sensitivity for the binding of biotin and streptavidin molecules on NAA substrates. The fabrication and formation of nanopore arrays on NAA surface by lithographic technique and graphs are shown in Figure 4. The graph represents the pore resistance dependent on different concentration of biotin solution with respect to different pore diameters and pore lengths obtained by NAA biosensor.

*4.3. Detection of Protein.* Alvarez et al. reported real-time detection of binding protein-A with rabbit, anti-sheep, and sheep immunoglobulin on the surface of NAA with respect to change in optical thickness using fluorescence microscopy [50]. The fabricated label-free NAA biosensor has structural dimensions of 60 nm and 6  $\mu\text{m}$  in diameter and thickness, respectively. The sensor surface modification by protein-A has been tested for interaction with rabbit, sheep, rabbit, anti-sheep and chicken's immunoglobulin. The binding interactions were carried out in PBS solution with 0.1 mg/mL biomolecules concentration for the biosensing applications. Schematic diagram in Figure 5 represents the protein-A modified sensor surface and step by step binding mechanism of rabbit anti-sheep and sheep's immunoglobulin biomolecules with protein-A. The sensitivity has been measured in terms of time versus change in optical thickness (OT) of sensor surface modified protein-A with rabbit, rabbit anti-sheep, sheep, and chicken immunoglobulin. Optical thickness has been rapidly increased with respect to time on NAA sensor surface for protein-A interacting with rabbit anti-sheep and

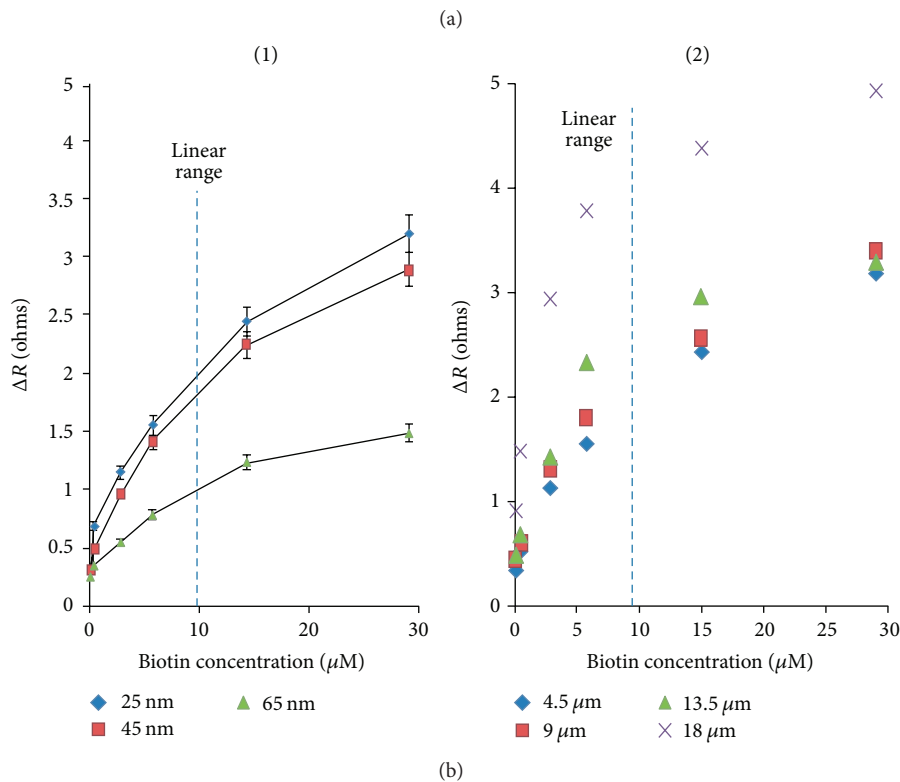
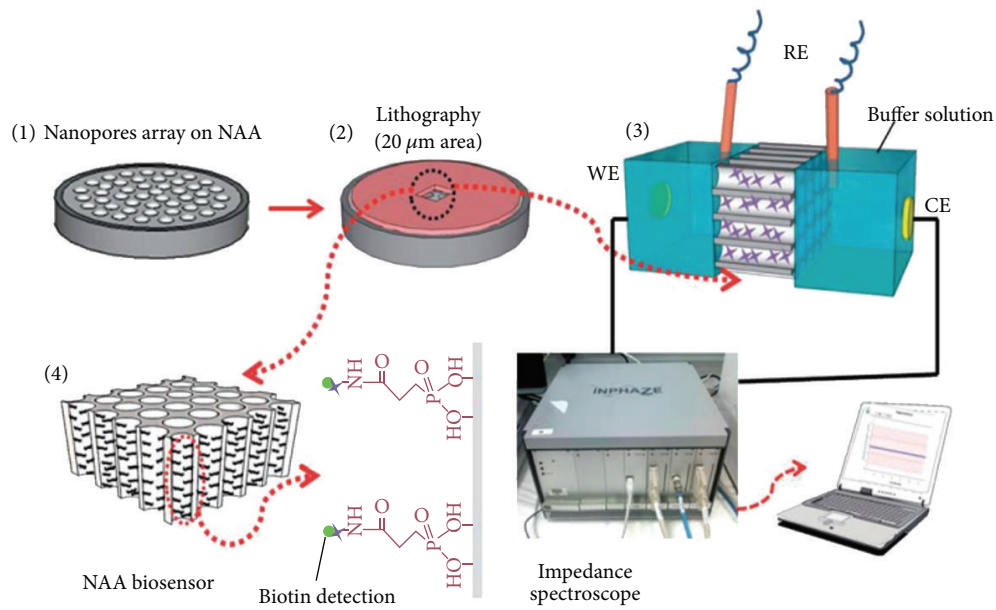


FIGURE 4: (a) Schematic representation showing fabrication process involved in the formation of NAA biosensor along with detection. (b) The graph representing changes in pore resistance with different biotin concentration and graph showing linearity between actual pore sizes with different biotin concentrations [49].

sheep immunoglobulin biomolecules. However, no binding affinity was observed for rabbit and chicken immunoglobulin biomolecules (dark base lines) due to weak interaction with sensor surface.

In addition to that, Lau et al. fabricated NAA for the detection of bovine serum albumin (BSA) through pore

widening using optical waveguide spectroscopy [83]. The immobilized BSA on NAA surface was observed for reflectivity to confirm the detection. High sensing performance was attained through the pore widening on NAA surface. The reflectivity increased with respect to increase in the sensitivity of material. The enhancement in sensing performance

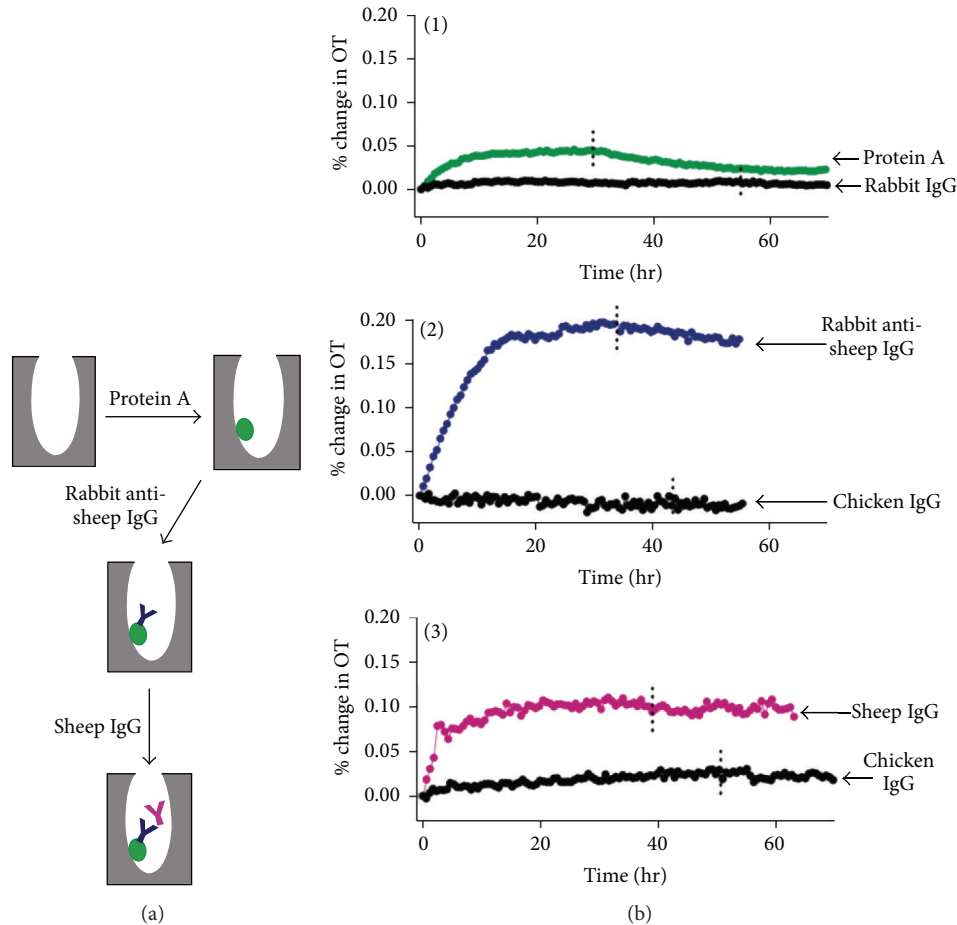


FIGURE 5: (a) The schematic diagram of binding affinity of biomolecules on NAA surface and (b) the time dependent change in optical thickness (OT) graphs showing the binding interaction of protein-A, rabbit, rabbit anti-sheep, sheep, and chicken immunoglobulin [50].

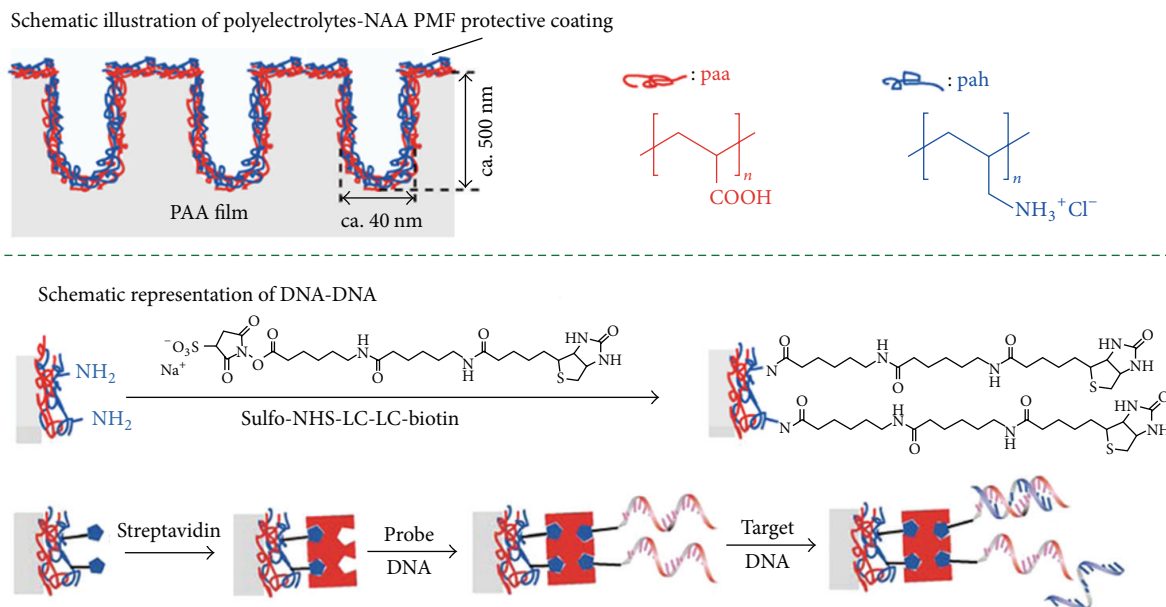
was obtained by processing film with uniform porous structure.

**4.4. Detection of DNA.** Pan and Rothberg developed immobilization of single stranded DNA (ssDNA) oligonucleotides on NAA and the fabricated materials were functionalized as a reflective biosensor to detect complementary DNA at area of  $1 \text{ nmol/cm}^2$  [84]. The fabricated structures of NAA were of  $6 \mu\text{m}$  and  $40 \text{ nm}$  in thickness and diameter, respectively. The fabricated sensor material has very high surface area which could easily accommodate DNA oligonucleotides on NAA surfaces. The detection of biomolecules was based on change in reflectivity on the surface of sensor material.

Takmakov et al. studied the ionic conductance *via* shrunk porous alumina and ssDNA biosensing by using porous material [85]. The NAA substrate was fabricated with the structural dimensions of  $60 \text{ nm}$  and  $10 \mu\text{m}$  pore diameter and depths, respectively. Further, NAA pore diameters were shrunk by hydrothermal treatment. The process involves three steps, formation of shrunk porous structures on sensor material by anodization, the reduction in the size of porous structures by hydrothermal treatment, and the detection of DNA oligomers by porous materials. The

ssDNA biomolecules were immobilized on sensor surface by aminosilane-glutaraldehyde chemistry [86]. The immobilization of ssDNA inside the sensor material decreases the pore resistance due to increase in the surface charge density of sensor material with negatively charged ssDNA. The immobilized ssDNA was hybridized with double stranded DNA (dsDNA) to increase the pore resistance. The dsDNA was denatured using urea which liberates complementary DNA strands to recover the initial pore resistance of immobilized ssDNA. The DNA detection has been achieved by the conduction variation with or without hybridization of DNA in internal nanopores of sensor material through electrical impedance studies.

Hotta et al. developed the multilayer structure polyelectrolytes coated NAA surface for the detection of DNA (single stranded probe DNA) and hybridized DNA using infrared reflection adsorption spectroscopy (IRRAS) [51]. The Al thin film was deposited on glass substrate by thermal evaporation followed by anodization to get pore diameter of  $40 \text{ nm}$ . Further, the polyelectrolyte solutions (poly (acrylic acid) and poly (allylamine hydrochloride)) were coated on NAA substrate using layer by layer coating process to form a protective layer during buffer solution immersion process.



Detection of DNA-DNA hybridization on NAA substrate by optical wave guide spectroscopy was carried out as follows: initially streptavidin was immobilized with biotin on NAA surface to detect DNA which shows increased red shift upon binding. Further, this immobilized DNA on NAA surface was bonded with noncomplementary (T2) target DNA. Thus, red shift has been increased due to complementary target DNA (T1) added with probe due to hybridization. Better sensing detection was found from complementary target DNA (T1) probe on NAA surface due to DNA hybridization which was observed using optical wave guide spectroscopy. Schematic representation of polyelectrolytes-NAA film and DNA-DNA hybridization assay using polyelectrolytes-NAA is shown in Figure 6.

**4.5. Detection of Viral Particle.** Moon et al. developed NAA to capture and align procapsid (*phi29* viral) particles using fluorescence microscopy [87]. Al foil was anodized to prepare the diameter and interpore distances of 75 and 105 nm, respectively. The pore structure was modified by coating of  $\text{Al}_2\text{O}_3$  film using atomic layer deposition (ALD) with average pore diameters of 38 nm. The surface of NAA was cleaned using 3 (trimethoxysilyl) propyl aldehyde (TMSPA/TMS) solution. Later, substrate was incubated in *phi29* viral and followed by rinsing in TMS buffer solution to remove unwanted *phi29* viral particles on surfaces. Later, DNA package on NAA substrate was tethered to capture *phi29* viral particles through polishing and centrifugation. By polishing, the chemically modified NAA substrate was incubated in procapsid solution so that high numbers of *phi29* viruses were bound into nanopores and small amounts of viruses were out of the nanopores. By centrifugation, the pore sizes were shrunk to 38 nm by ALD method: actual size of *phi29* viral particles was 45 nm. The attractive capture behavior was observed via centrifugation for *phi29* viral particles on DNA packaged

NAA substrate. The nanopore sizes were less than viral particle sizes; thus, it was easy to be captured onto substrate. The fluorescence microscopy was used to detect the viral particles on NAA substrates.

**4.6. Detection of Vitamin C.** Chen et al. developed the photonic structure of biomimetic based NAA with distributed Bragg reflector for the sensing of vitamin C molecules [52]. Different anodization process was used to fabricate NAA with distributed Bragg reflectors by galvanostatic pulse anodization process. However, excellent sensing performance of vitamin C was observed for NAA prepared with anodization period of 675 s at  $3^\circ\text{C}$  with current ratio of 6:1 compared to other anodization parameters. Schematic representation of vitamin C molecule captured by APTES and GTA solution on NAA distributed Bragg reflectors and sensing results of vitamin C molecule with respect to change in effective optical thickness (OT) are presented in Figure 7. Surface functionalization of sensor involves the APTES modified NAA distributed Bragg reflectors with internal surface hydroxylated by using  $\text{H}_2\text{O}_2$  solution, further modified with APTES using Chemical Vapor Deposition (CVD) process, and later treated with GTA solution to activate the amine groups of APTES. Thus, modified NAA distributed Bragg reflectors were used to adopt vitamin C molecules on internal surfaces. The RIS has been used to detect different solutions of vitamin C molecules on sensor surfaces with respect to change in effective optical thickness of sensor substrate.

**4.7. Detection of Enzyme.** NAA has been developed for the detection of glucose oxidase (GOx) using UV-vis spectroscopy by Darder et al. [88]. The pore diameter and thickness of NAA pores were in the range of 30–80 nm and 33–150  $\mu\text{m}$ , respectively. The GOx was immobilized on NAA surface and was fixed between two disks; the acetate

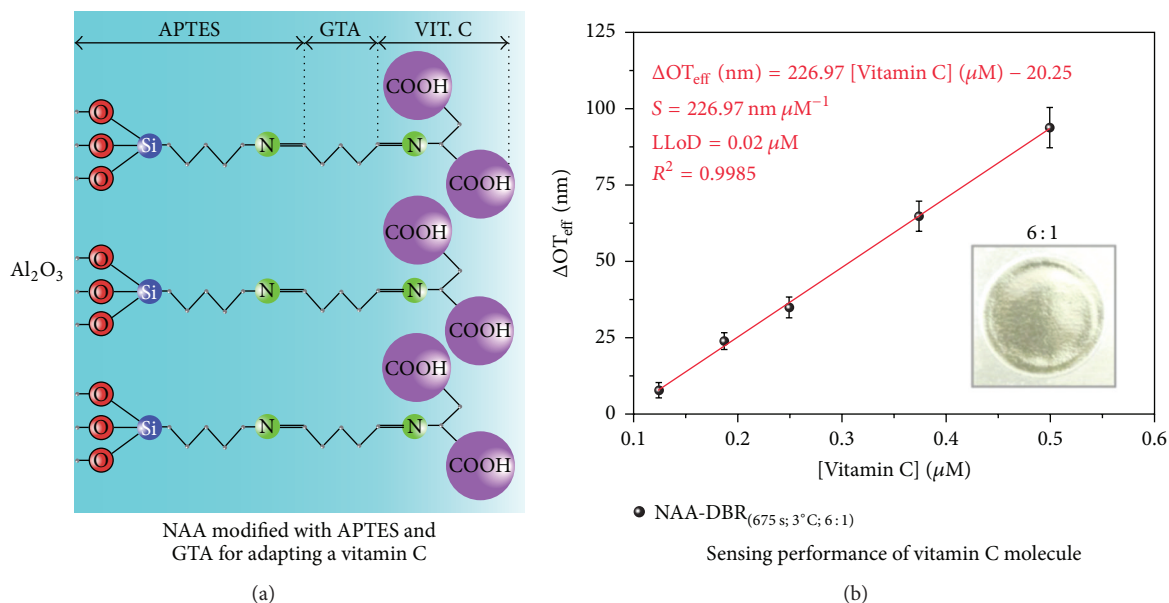


FIGURE 7: (a) NAA modified with APTES and GTA aqueous solutions for binding vitamin C molecules and (b) sensing of different concentration of vitamin C molecules using reflectometric interference spectroscopy [52].

buffer solution was filtered through NAA substrate which was placed in between the disks, followed by the GOx with acetate buffer and chitosan solutions. The lack of chitosan covering on GOx modified NAA surface may decrease the enzyme activity due to leakage of glucose oxidase from the surface. Outer protecting layer of chitosan can permeate the water molecules and allows ions to transport and bind to protein. The UV-vis spectroscopy has been used to analyze the activity of immobilized GOx. The solutions of 5 mM potassium ferrocyanide and 40 mM glucose were mixed in 0.1M Tris/HCl buffer for analysis. Later, 40  $\mu\text{M}$  GOx was added to the prior solution for enzymatic reaction. The procedure was repeated to attain the linear relationship between the absorbance and GOx reactions. The platinum electrode holds the GOx modified NAA surface for glucose determination. The increase in pore size leads to increase in the enzymatic activity and shows good response even at low concentration. The response was very less for higher thickness NAA material with decrease in pore sizes.

Recently, polyelectrolytes based layer by layer coating on NAA for the biosensor applications was explored. Krismastuti et al. fabricated layer by layer coating of polyelectrolytes on NAA for the bacterial enzyme detection of proteinase-K using interferometric reflectance spectroscopy (IRS) [53]. Three different thicknesses of NAA such as 1.3, 3.0, and 4.4  $\mu\text{m}$  with pore diameter, interpore distance, and wall thickness of  $30 \pm 1.7$ ,  $100 \pm 1.5$ , and  $70 \pm 1.8$  nm, respectively, were fabricated. The aim was to increase the thickness of porous layer to influence the easy detection of the enzyme. Polyelectrolytes like poly (sodium-4-styrenesulfonate) (PSS) and poly-L-lysine (PLL) have been used as negatively and positively charged layers, respectively, for layer by layer coating onto the sensor surface. Instead of gold coating on alumina surface polyelectrolytes were coated due to

several advantages such as ease of availability and low cost and can play a vital role in increasing the RI on sensor surface. The fabrication process of layer by layer deposition of polyelectrolytes on to the sensor surface is as follows: dust free NAA was silanized by APTES, followed by 7–10 nm thick gold film onto NAA substrate to prevent the pore blocking. The second step is layer by layer coating of polyelectrolytes using custom designed flow cell and coating was monitored by IRS. Separately PSS and PLL were taken in NaCl solution: PSS solution, followed by PLL solution at a flow rate of 0.2 mL/min, was injected alternatively into the sensor surface. Thus, multilayer coating of opposite charges of polyelectrolytes was achieved on the NAA surface. The polyelectrolytes coated NAA sensors of different thickness were used to detect bacterial enzyme of proteinase-K by IRS spectroscopy system which is shown in Figure 8. The enzyme exposure to substrate of thickness 1.3  $\mu\text{m}$  shows the effective optical thickness (EOT) of 1.9 nm and after washing sample with Mili-Q water the EOT was blue shifted to 7.1 nm. Proteinase-K enzyme was also exposed to substrate of 3.0  $\mu\text{m}$  thick which reveals that EOT was blue shifted to 1.8 nm and after washing with water it was shifted to 1.9 nm. However, proteinase-K exposure on the substrate of 4.4  $\mu\text{m}$  thick showed red shift in EOT which is due to polyelectrolytes being diffused deep inside the nanopores to form high thick sensor so that enzymes were occupied easily into porous layers and hence increasing the RI of sensor substrate, compared to those of 1.3 and 3.0  $\mu\text{m}$  thick sensor.

A simple and smart detection by using trypsin immobilized NAA through PL system was developed by Santos et al. [54]. NAA was fabricated by two-step anodization method; the average pore size and lengths were of 40 nm and 7.1  $\mu\text{m}$ , respectively. The size of trypsin biomolecule was 3.8 nm and hence molecules were easily accommodated and immobilized

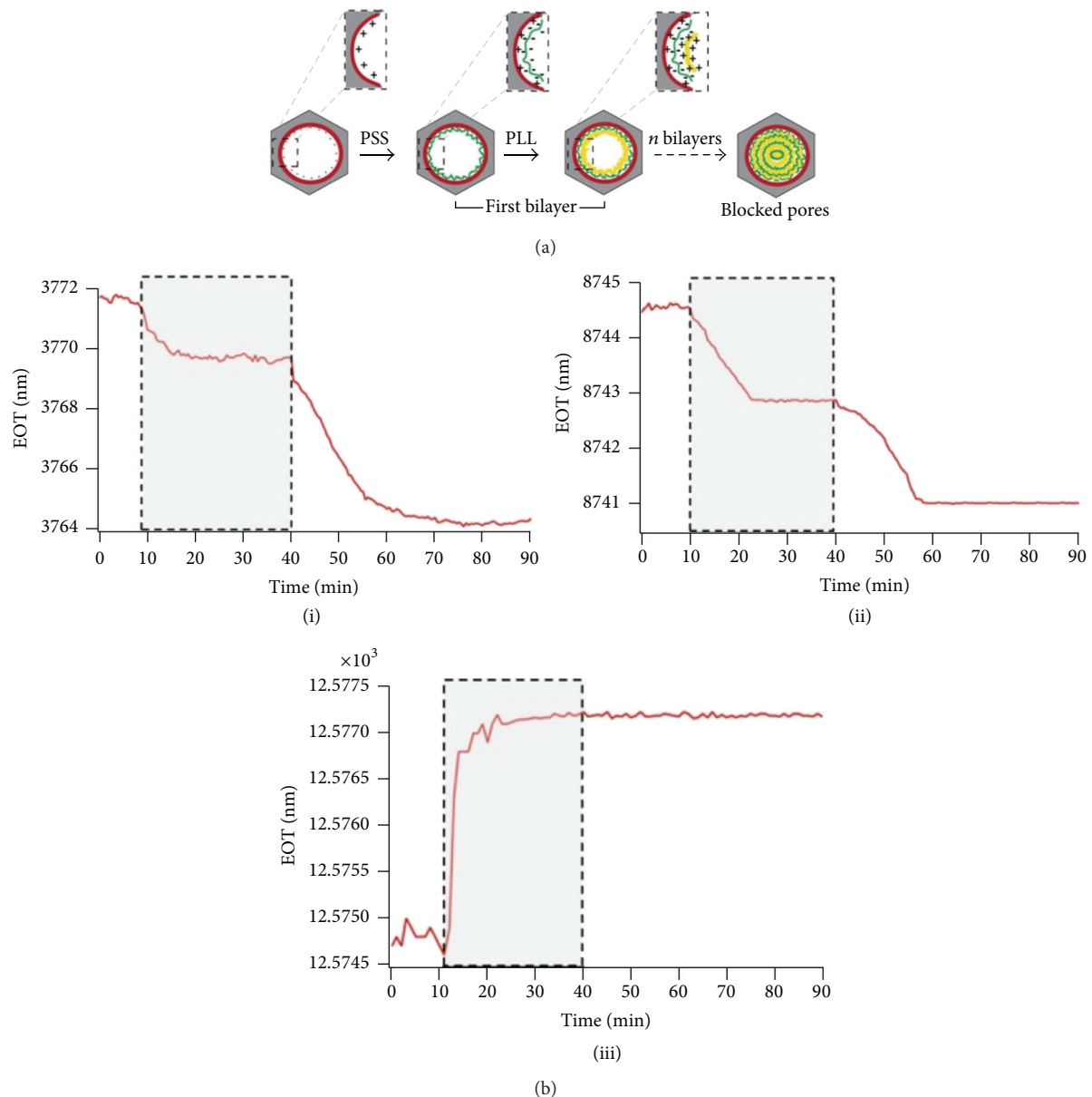


FIGURE 8: (a) Layer by layer deposition using polyelectrolytes like poly(sodium-4-styrenesulfonate) (PSS) (greenish) and poly-L-lysine (PLL) (yellowish) on NAA and (b) the effective optical thickness (EOT) plot of sensing of proteinase-K by layer by layer coated polyelectrolytes on NAA thicknesses of 1.3 (i), 3 (ii), and (iii) 4.4  $\mu\text{m}$  using IRS system [53].

on the nanopores. The process of trypsin immobilization in nanopores was made possible by silanization process: APTES and glutaraldehyde (GTA) were mixed together with NAA, and later trypsin biomolecules were allowed to bind *via* amino groups on porous substrate by the incubation process. The schematic diagram of different stages of immobilized trypsin molecules on NAA and sensitivity plot of trypsin by change in effective optical thickness with respect to different stages on NAA surface by PL spectroscopy is shown in Figure 9. The detection of immobilized trypsin has been done by observing change in effective optical thickness on sensor substrate by PL. Effective optical thicknesses of bare NAA, APTES coated NAA, GTA-modified NAA, and

immobilized trypsin on NAA were found to be 0.1, 0.6, 1.2, and 1.8%, respectively. From the above observation, it has been confirmed that there was an obvious increment in effective optical thickness of NAA.

Invertase is one type of enzyme which is used for the production of sugars and used for hydrolysis process like inverting sucrose into glucose and fructose. Thus, NAA biosensor was fabricated and applied to real-time detection of invertase enzyme using Surface Plasmon Resonance (SPR) sensor by Dhathathreyan [55]. For the enzyme immobilization, the substrate of pore diameter and inter-pore distances of 60 and 100 nm, respectively, were used. The uncontaminated NAA substrate was kept with invertase enzyme solution

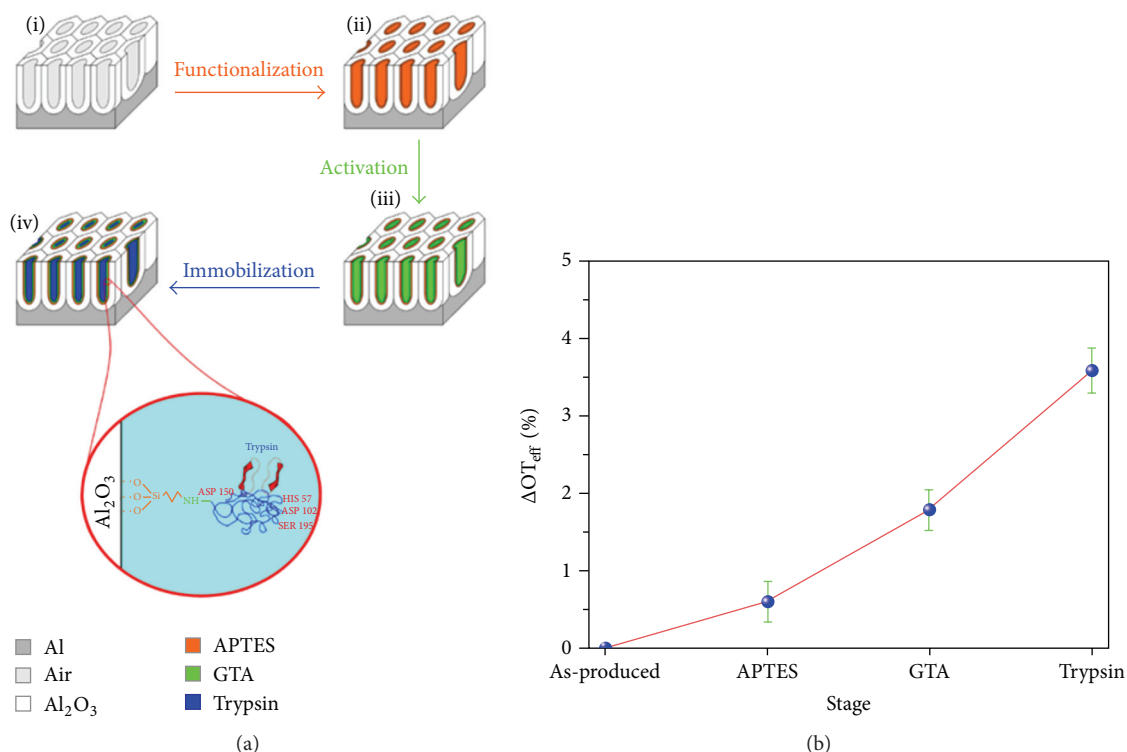


FIGURE 9: (a) The schematic representation of immobilization of trypsin on NAA, the different stages of the fabrication process of the NAA enzymatic sensor. (i) Bare NAA, (ii) APTES modified NAA, (iii) GTA-modified NAA, and (iv) trypsin immobilized NAA. (b) The effective optical thickness with respect to different surface functionalization [54].

for 1 h at required pH value. The enzyme immobilization activity was tested in the experimental flow cell by gold coated glass plate and SF10 prism set-up sealed with Teflon cell to impound tested solution. The immobilized invertase and its interaction with sucrose were analyzed by calculating the change in RI on substrate using SPR signal as shown in Figure 10.

On the other hand, gelatin-modified NAA was fabricated for the real-time detection of trypsin using RIFS by Nemati et al. [56]. Gelatin molecules play vital role for chemical sensing and better selectivity towards trypsin molecules. The NAA substrate was gold coated with 5 nm thickness using sputter deposition, and the APTES and GTA solutions were used to modify the surface of NAA for the formation of amino groups. After this, gelatin molecules were allowed to immobilize on inner surface of the pores. The different concentrations of trypsin enzyme (0.125, 0.3, 0.5, 0.6, and 1 mg mL<sup>-1</sup>) were used to analyze the sensing performance by using RIFS system. The effective optical thickness was changed with respect to different concentration of trypsin molecules. However, higher concentration of trypsin molecules (1 mg mL<sup>-1</sup>) showed fast response in RIFS. More concentration of gelatin molecules immobilized on the pores provides faster response to trypsin molecules. Hemoglobin has been used instead of gelatin as a chemical sensing element that also shows faster sensing performance. Schematic diagram of enzyme detection by gelatin-modified NAA using RIFS set-up and also different concentration of analyte solution leads to

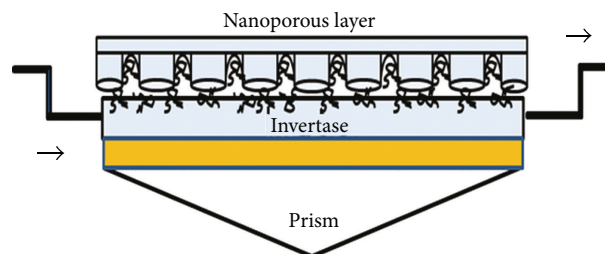


FIGURE 10: Sensing of immobilized invertase enzyme on NAA surface in flow cell of SPR [55].

change in effective optical thickness in real-time which is shown in Figure 11.

## 5. Gold Coated NAA (Au-NAA) Biosensor

**5.1. Detection of Protein.** While integrating NAA into the SPR system, the RI at the close proximity of the sensing platform plays vital role. Thus, Hierro-Rodriguez et al. have extracted the RI values of different NAA templates which are useful in developing SPR and long range SPR sensors [89]. Similarly, Kim et al. developed an Au-NAA biosensor for the label-free detection of aptamer-protein binding interaction on sensor surface using combination of localized surface plasmon resonance (LSPR) and interferometry [90]. The obtained uniform porous structured NAA substrate had pore diameters and

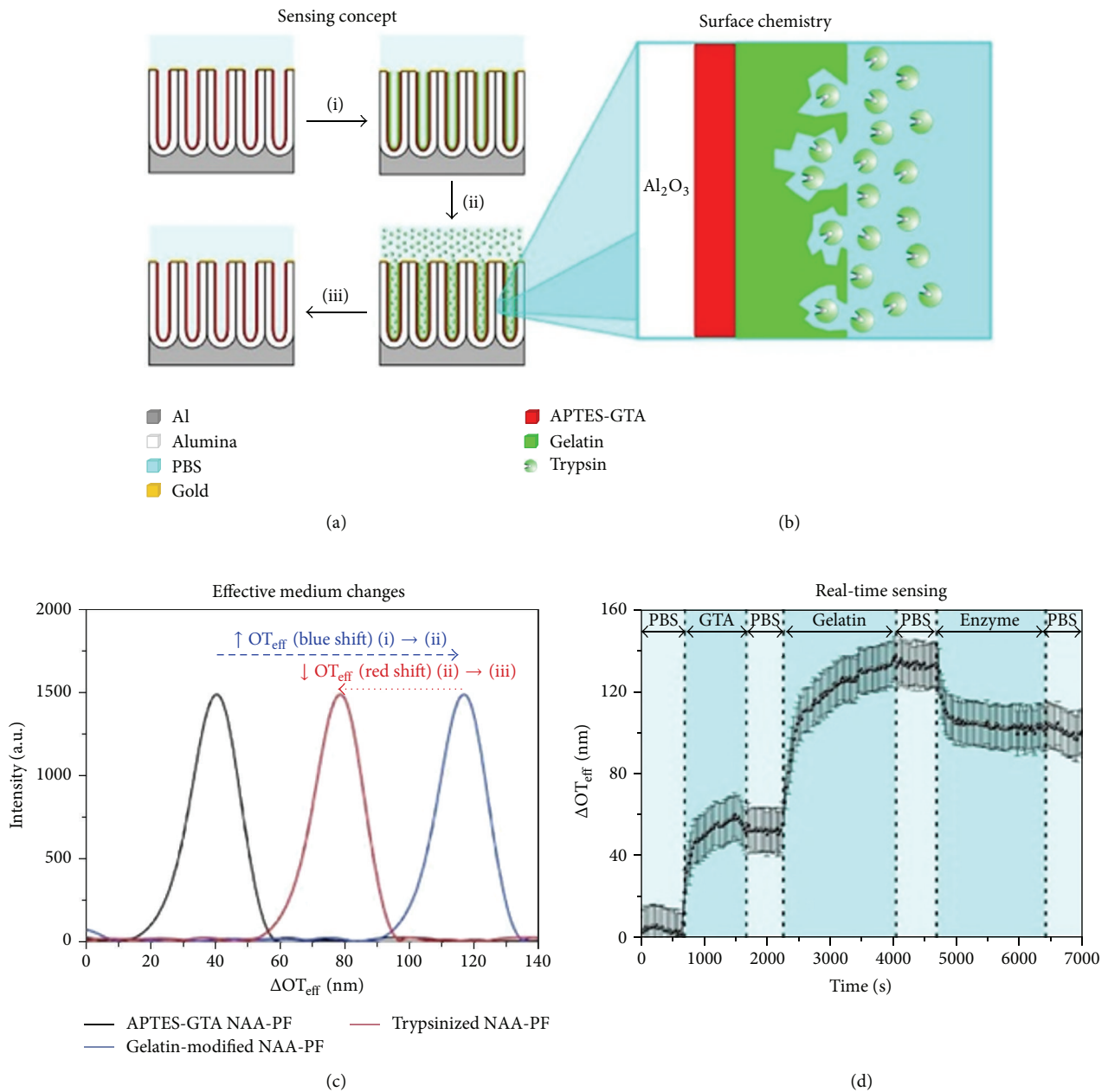


FIGURE 11: (a) Sensing of enzymes by gelatin-modified NAA using RIfS system, (b) surface chemistry used in enzymatic sensor where gelatin acts as the chemical sensing molecule for the enzyme, (c) the effective optical thickness changes in gelatin modified NAA with respect to the intensity using RIfS, and (d) real-time sensing of enzyme [56].

interpore distances of 60 and 120 nm, respectively. The size of pore diameter was reduced to 47 nm by coating of Au thin film on NAA surface by thermal evaporation technique with thickness of 15 nm for the enhancement in optical properties on their surface. The aptamer-I was immobilized on NAA surface by rinsing NAA with thiolated aptamer-I and 6-mercaptohexanol solutions. Further, aptamer-I modified NAA substrate was rinsed with mixture of thrombin and PBS solution. After processing, aptamer-II solution was interacted with aptamer-I-thrombin modified NAA surface. The RI was high for aptamer-I with NAA compared to bare Au-NAA. The obtained high concentration of aptamer-I was

immobilized on Au-NAA which was red shifted and was observed through interferometry system. Later, aptamer-I-thrombin immobilized Au-NAA surface revealed that the red shift was due to enhancement in RI of NAA. However, nonspecific binding of aptamer-I and aptamer-II on Au-NAA surface was observed whereas aptamer-I-thrombin on Au-NAA surface resulted in better binding interaction. The RI depends on the binding interaction of biomolecules on sensor surfaces. The saturation state was attained for the concentration of thrombin more than  $100 \mu\text{M}$ ; above this concentration no response was found from interferometry and LSPR signals.

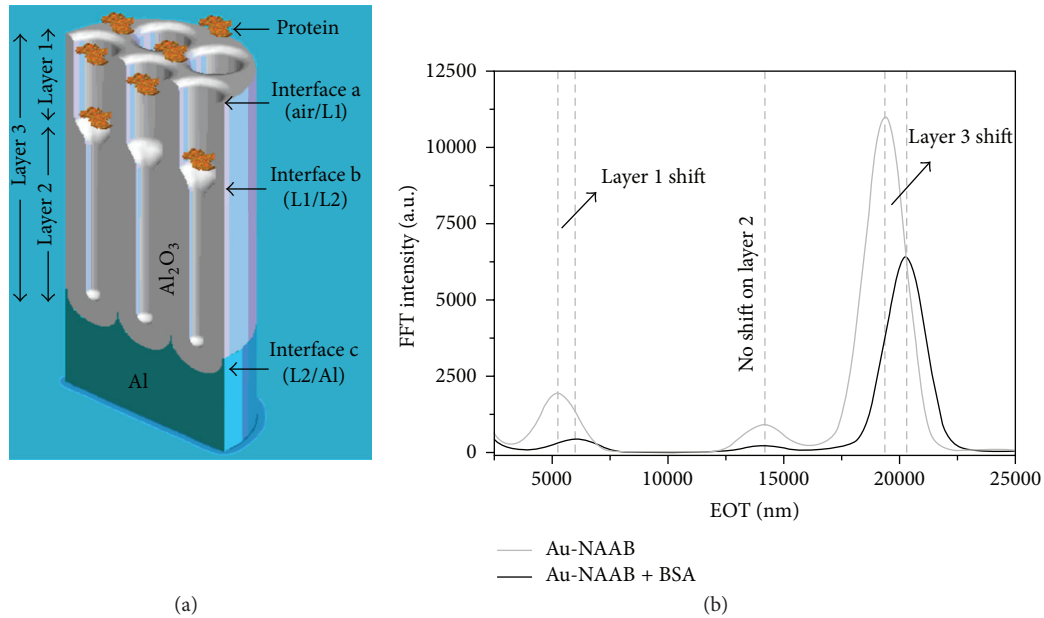


FIGURE 12: (a) The schematic diagram of Au-NAA bilayer structure and (b) effective optical thickness with and without protein on Au-NAA bilayer optical biosensor measured by fast Fourier transform [16].

In recent years, there have been increased interest on developing label-free optical biosensors based NAA. These types of label-free optical biosensors are exhibiting high throughput in medicinal applications. The Au-NAA bilayer substrate as label-free optical biosensor for BSA has been developed by Macias et al. [16]. The bilayer structure of NAA has been prepared with different porosity with pore diameter and depths of 68 nm and 1.9  $\mu\text{m}$  as well as bottom layers with 33 nm and 4.7  $\mu\text{m}$ , respectively. The design of bilayered structures was planned in such a way that the top layer can be used as entry for protein whereas low pore size bottom layer could not allow protein in this direction. The gold deposition on NAA was achieved by coating 10 nm thickness of gold film on top of the surface of NAA bilayer *via* sputtering technique. The greater sensitivity was attained by increasing the layer of gold film on sensor surface which increases the RI of NAA. Initially, sensor materials were incubated with proteins at quantity of 1 mg/mL in PBS buffer solution for 2 h at 5°C to avoid the binding on surface of gold layer. Further, samples were thoroughly washed in PBS solution to remove any free contaminants. Thus, identical procedure was carried out for protein in PBS solution for biosensing applications. It was found that the protein adsorption occurred on the surface of NAA due to electrostatic forces between protein and sensor substrate. The allowed protein was detected at the top layer using change in optical thickness between two layers. The following equation has been used to detect the protein by change in optical thickness: that is,

$$\Delta\text{EOT} = \text{EOT (after protein penetration)} - \text{EOT (before protein penetration)}, \quad (1)$$

where EOT is effective optical thickness.

The schematic diagram of fabrication and structure of Au-NAA bilayer and fast Fourier transform graph of the optical

biosensing response of Au-NAA bilayers before and after the penetration of protein into sensor structures are shown in Figure 12. As shown in Figure 12(b), the peak intensity was very less in overall gold coated NAA bilayer with infiltration of protein due to adsorption of protein in layer 1. The increase in effective RI of layer 1 will decrease the RI of overall sensor substrate. The effect of optical thickness was increased in layers 1 and 3 due to the above reason, whereas less shift in layer 2 optical thickness was observed. The same results were obtained for Au-NAA bilayer without protein where higher intensified peaks were formed. The Au-NAA bilayer with the protein (BSA) has been sensed by intensified peaks of layers 1 and 3.

In similar work, Yeom et al. fabricated Au-NAA for real-time detection of antigen (C-reactive protein) [57]. The fabricated NAA have dimensions of 100 nm pore diameter and depths of pores were 4.9  $\mu\text{m}$ . The Au-NAA materials were obtained by electron beam evaporation method. Here, gold layer coating on sensor material acts as high SPR compared to bare Ag or Au metals. The Au coated sensor substrate has produced LSPR and it plays vital role in accepting and immobilizing antibody on sensor surfaces. The immobilized antibody has been captured by Au-NAA material which was rinsed and kept for 24 h in solution of 11-mercapto-1-undecanol and EtOH. The unwanted antibody was removed by treating sensor surface with Tris-HCl solution instead of PBS solution to avoid the damage. The detection of antigen using Au-NAA works on LSPR principle in which the allowed antigens react with antibody to change RI of the sensor substrate. The biosensing mechanism has been predicted by change in the reflectivity of the sensor substrate by real-time biosensor detection method (Figure 13).

Similarly, Hiep et al. fabricated photonic structure of Au-NAA film for the detection of biomolecular interaction using interference localized surface plasmon resonance

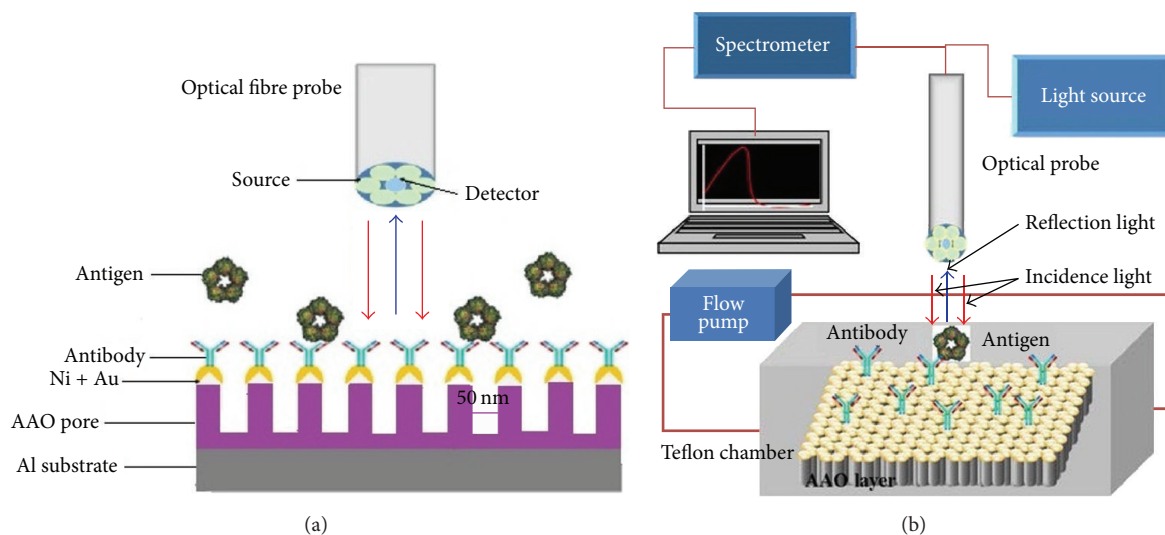


FIGURE 13: (a) The antigen detection using antibody functionalized Au-NAA and (b) set-up for the real-time detection of antigen [57].

(iLSPR) system [58]. The gold coated NAA film (Au-NAA) has thickness of 270 nm which was rinsed in 11-amino-1-undecanethiol hydrochloride solution to functionalize with free amino groups available at substrate surface. A mixture of PBS and BSA solutions was used for rinsing NAA surface. The iLSPR system was used for the detection of binding interaction of two different biomolecules on NAA surface. The RI was slightly changed due to interaction of biotin-avidin binding on NAA surface and further increased for BSA binding with avidin on sensor surface. The limit of detection for avidin using Au-NAA film by iLSPR was found to be 100 ng/mL. Schematic diagram shows iLSPR biosensor and wavelength depends on reflectance spectra changes by biotin-avidin and biotin-BSA binding interaction on Au-NAA surface (Figure 14).

**5.2. Detection of DNA.** Kim et al. fabricated “cap like” gold structures which were coated on NAA for the detection of DNA hybridization sensing mechanism using LSPR microscopic system [59]. The fabricated NAA has the diameter and thickness of 60 nm and 5  $\mu\text{m}$ , respectively. The immobilization of DNA on Au-NAA was achieved by mixing of 10  $\mu\text{M}$  thiolated DNA probe and 100  $\mu\text{M}$  6-mercaptohexanol solutions which were further applied on sensor surface. A target DNA was hybridized with probe DNA on sensor surface by PBS solution. The sensing of probe DNA and target DNAs hybridization was captured by the increment in wavelength shifts ( $\lambda_{\text{max}}$ ) and relative reflected intensity which depends on change in the concentration of target DNA on the sensor surface. The saturation state was found at the concentration of target DNA which exceeded the limit of 10  $\mu\text{M}$ . Schematic diagram shown in Figure 15 represents the working mechanism and sensing measurement of DNA hybridization on Au capped structure of NAA using LSPR system.

**5.3. Detection of Cells.** In biosensors field, researchers are trying to develop NAA with gold film coating for the detection

of biomolecules such as proteins and DNA. However, less study has been carried out on the fabrication of Au-NAA for the detection of single living cell adhesion and seeding on sensor surfaces using SERS system. Toccafondi et al. fabricated biosensor substrate, *that is*, Au-NAA, for single cell sensing with the help of SERS [91]. Fabricated Al thin film on glass substrate has thickness of 500 nm by e-beam evaporator followed by anodization process. The prepared film structure had pore diameter and depth sizes of 50 and 120 nm, respectively. Thick gold layer of 25 nm on NAA was coated by e-beam evaporator and N2a cell lines were used from mouse neuroblastoma for living cell sensing application by bare NAA and Au-NAA using SERS system. In this experiment,  $5 \times 10^4$  N2a cells were mixed in 2 mL of high glucose medium and cells were grown in this solution at 37°C with humidified CO<sub>2</sub> atmosphere. Later, cells were allowed for sensing application using bare NAA and Au-NAA. During the sensing process, different diameters (60 and 120 nm) of bare NAA were used to adhere to the N2a cells without using any adhesion solution which was due to biocompatibility and surface roughness of the material. The adhered cells were captured with fluorescent dyes by confocal fluorescence microscopy. However, the aim was to develop Au-NAA for living cell sensing applications using SERS. The excellent micro Raman scattering improvement has been achieved by cell seeded on Au-NAA. The sensing of Au-NAA material was done by laser light obtained from micro Raman spectroscopy. Enhancement in Raman peaks was observed in the presence of N2a cell due to adhesion and growth on surface of sensor material. On the other hand, Toccafondi et al. fabricated biocompatible Au-NAA for the detection of fibroblast living cells using SERS and fluorescence microscopy [92]. The SERS signals were high for the higher pore dimension. The cells were grown on Au-NAA surface due to biocompatibility of material. The living cells (NIH-3T3 cells) were incubated in Au-NAA surfaces for 2 days and grown on the surface. The better sensitivity was achieved for the bigger pores (130 nm)

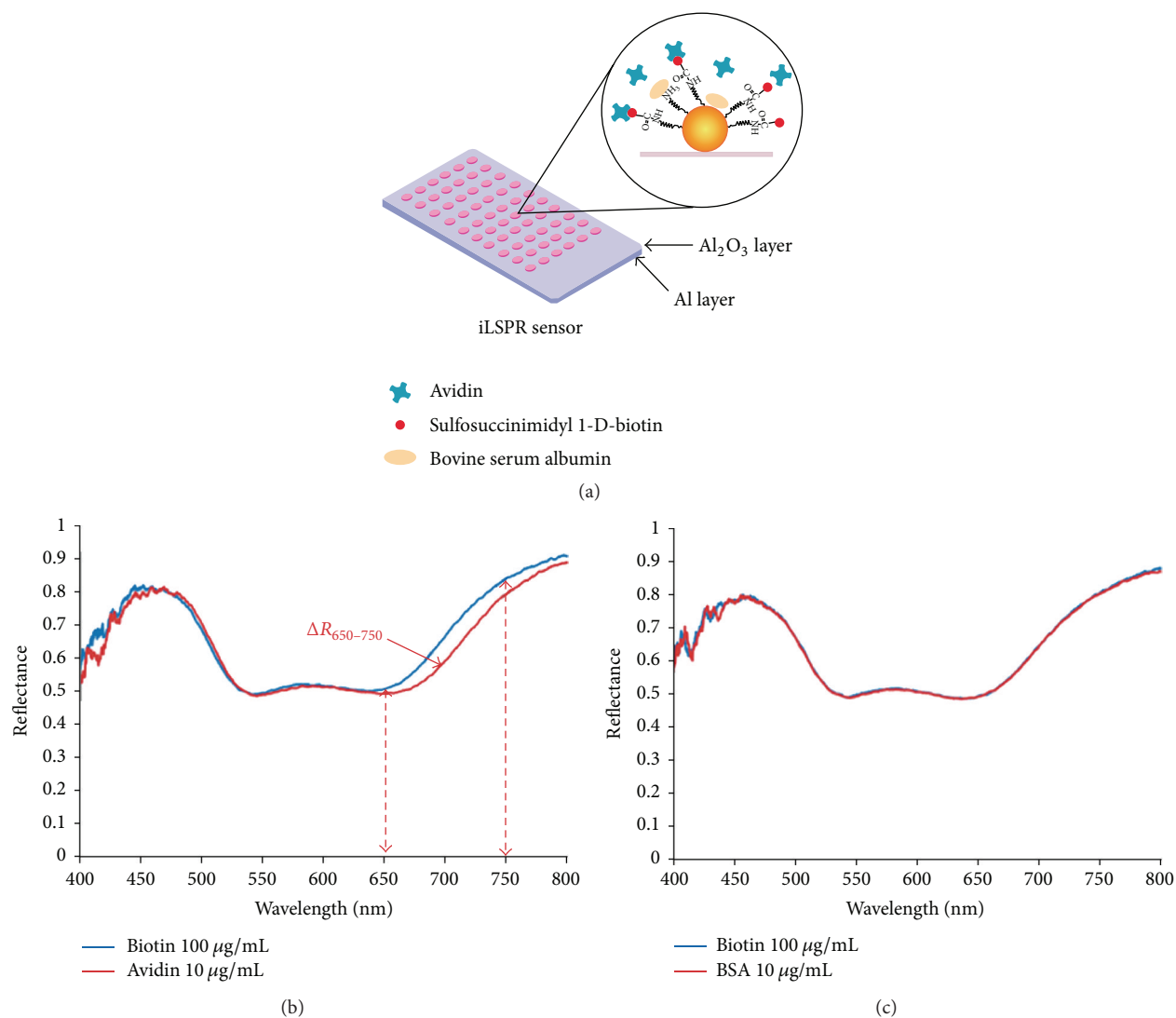


FIGURE 14: (a) Schematic representation of the iLSPR biosensor, (b) the reflection spectra which depend on the change in RI upon binding of biotin-avidin, and (c) interaction of biotin-BSA [58].

and smaller pore lengths (50 nm) of Au-NAA for living cell sensing using SERS system.

**5.4. Detection of Fluorescent Molecules.** Das et al. developed novel Au-NAA with honeycomb pore structure for the biosensor applications with fluorescent molecules such as cresyl violet, rhodamine 6G, and green fluorescent protein-mut2 using SERS system [60]. Honeycomb pore structures of NAA with the pore size and wall thickness of 15 and 36 nm, respectively, were fabricated. Three different honeycomb pore structures were fabricated: NAA1 with pore size and wall thicknesses of  $181 \pm 45$  and  $82 \pm 35$  nm (bigger pores), NAA2 of  $82 \pm 7$  and  $21 \pm 7$  nm (medium pores), and NAA3 of  $29 \pm 4$  and  $13 \pm 4$  nm (smaller pores), respectively. The SERS signals were enhanced by coating 25 nm of gold film on NAA by thermal evaporation, namely, Au-NAA1 with pore size and wall thickness of  $157 \pm 35$ ,  $104 \pm 35$  nm, and Au-NAA2 with  $59 \pm 9$ ,  $40 \pm 9$  nm, and Au-NAA3 with  $15 \pm 3$  and

$36 \pm 3$  nm, respectively. To achieve the sensing, fluorescent molecules were deposited on different Au-NAA substrates by chemisorption method and tested with the molecules of concentration  $10^6$  M. Further, cresyl violet, an organic dye, was chosen which is routinely used in nerve tissue sector for biological stain. At first, cresyl violet molecules were coated on different Au-NAA structures revealing that SERS signals were enhanced due to  $\text{NH}_2$  groups which were forcefully attached on sensor surfaces attributed to vibrational modes at  $591 \text{ cm}^{-1}$ . These molecules were strongly attached on surface of Au-NAA3 due to low porosity whereas in case of Au-NAA1 and Au-NAA2 molecules were not attached due to medium and high porosity, respectively. It was found that the enhancement in SERS measurement of Au-NAA2 compared to other two substrates due to low pore size and wall thickness. The enhancement was observed in SERS measurements for rhodamine 6G and green fluorescent protein-mut2 molecules which was due to the extensive

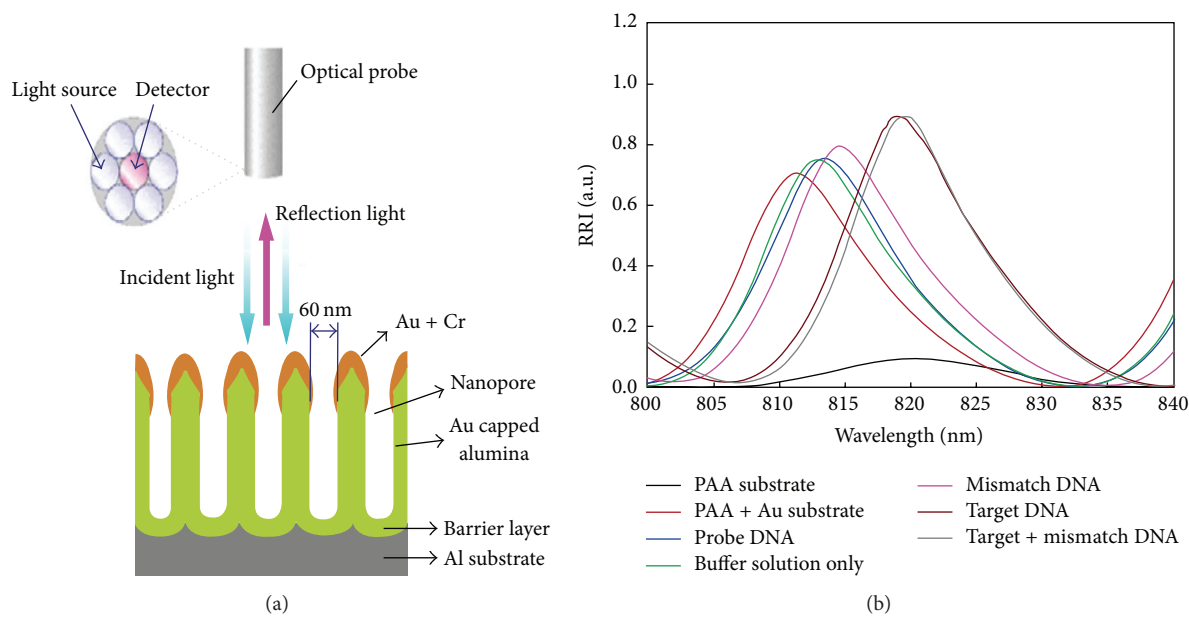


FIGURE 15: (a) DNA hybridization sensing mechanism of Au capped structure of NAA; (b) change in relative reflected intensity (RRI) of DNA hybridization detection on Au capped structure of NAA [59].

use of rhodamine 6G as a dye molecule in fluorescence microscopy. Due to the fact that molecular adsorption on metal surfaces is because of electronegativity of metals, this electronegativity is high for noble metal Au compared to Ag. Thus, the adsorption of molecules was enhanced by Au coating on sensor substrates. The rhodamine 6G molecules were deposited over surfaces of Au-NAA1 and Au-NAA2 to test in SERS systems. These molecules were strongly bound to Au surfaces and the enhancement in SERS was observed with strong intensity of vibrational modes at  $1361$  and  $1510\text{ cm}^{-1}$ . The green fluorescence protein-mut2 was a fluorescent protein which has a capability of fluorescence recovery to use in slow biological processes. The SERS spectra enhanced through the fluorescent proteins which were coated on Au-NAA2 surfaces and SERS peaks were obtained at  $1500\text{ cm}^{-1}$ . The schematic diagrams of honeycomb nanopore structure of Au-NAA and the SERS spectra are shown in Figure 16 which reveals the detection of (i) cresyl violet and (ii) rhodamine 6G using SERS.

**5.5. Detection of Binding of Alkyl Thiol.** Previously, several articles show developing of NAA for the detection of immobilized biomolecules on sensor surface by soaking the substrate in mixer of preferred buffer solutions like PBS/Tris-HCl containing biomolecules. However, biomolecules sometimes may not properly bind on the substrate with this technique. On the other hand, the biomolecules can also be immobilized onto the substrate by flowing the biomolecules taken in a mixture of buffer solutions within microfluidic channels for better binding due to higher chances of biomolecules coming in contact with the surfaces. The microfluidic system comprising sensor substrate has the advantages such as healthy binding biomolecule, less amount of sample for the detection, and rapid sensitivity in microchannels. For the

first time Kumeria and Losic developed Au-NAA comprising microfluidic channel for label-free optical biosensing for the detection of binding of alkyl thiol on sensor substrate by enhancement of reflectivity in interferometric spectroscopy signals [61]. Pore size and pore depths of fabricated NAA structures were of  $60\text{ nm}$  and  $4\text{ }\mu\text{m}$ , respectively. In addition to that, scanning electron microscopy was used to measure the interpore distance and it was about  $60\text{--}100\text{ nm}$ . The reflectance interferometric spectroscopy (RIS) signals were enhanced by the pores and surface area of internal pore structures of NAA. The fabricated controlled parameter of NAA has been coated by different metals like Au, Ag, Cr, Pt, and Ni by atomic layer deposition. However, Kumeria and Losic have not observed significant reflectance interferometric intensity signal originating from Pt, Ag, and Ni metals. The better interferometric signal has been obtained for Au and Cr metals due to enhancement of reflectivity on these thin metals. The optical biosensing performance was performed only by Au-NAA structure because Au metal has biocompatibility and chemical stability and is preferred for particular molecules binding detection for biosensing applications. The set-up comprises Au-NAA into microfluidic device with connected syringe pump and fiber optic probe. The optical biosensing showed by  $1\text{ mM}$  thiol molecules which were passed into Au-NAA substrate mounted microfluidic chip reveals higher wavelength with respect to change in effective optical thickness obtained for adsorption of molecules on Au surfaces. Furthermore, even at low concentration of molecules it has shown better sensitivity. The effective optical thickness has been increased with increase in the concentration of thiol molecules on sensor surfaces. They also analyzed real-time sensing performance of the molecule bounded with thiol group on sensor substrate which shows excellent maximum wavelength. The schematics shows the Au-NAA embedded

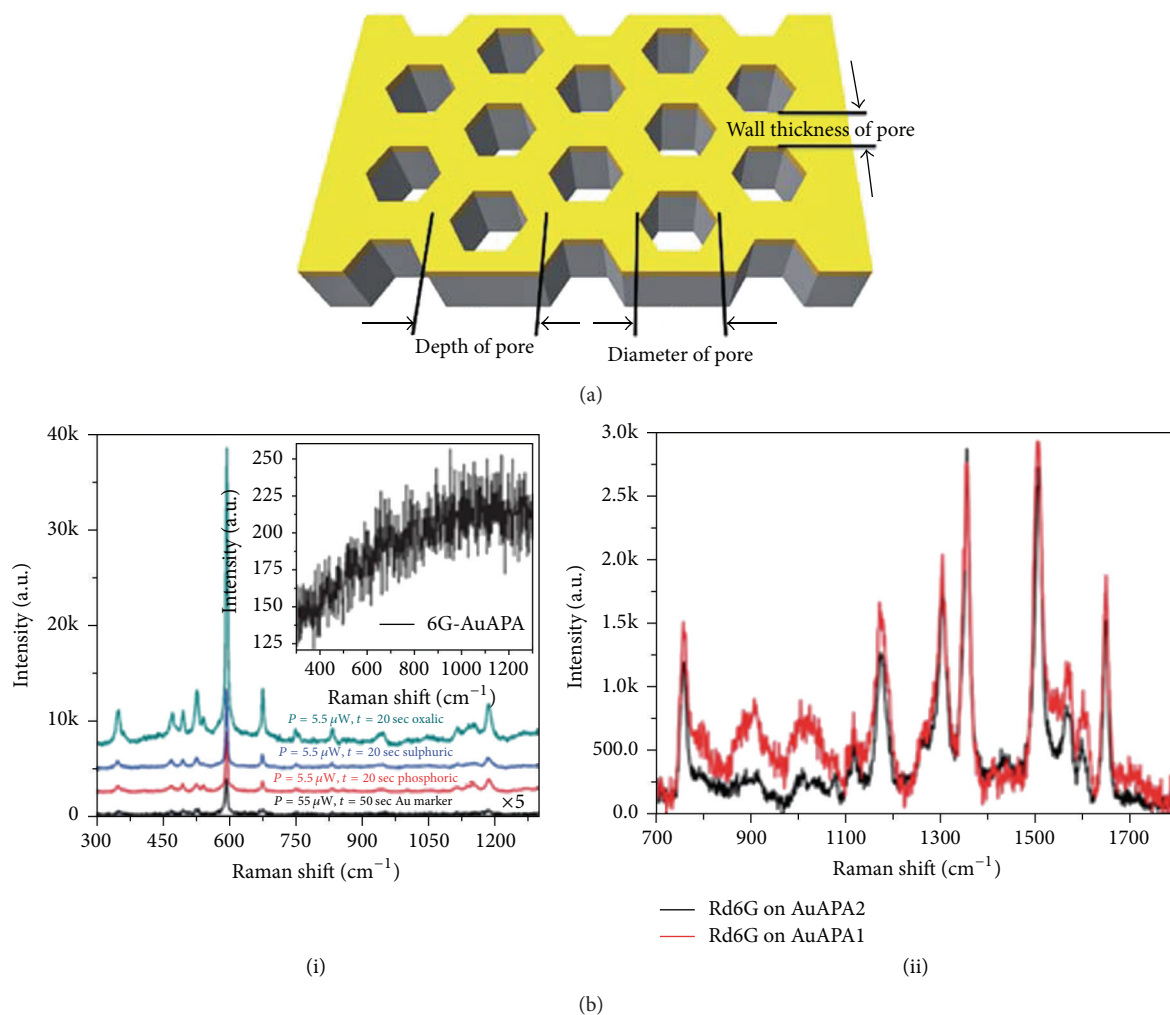


FIGURE 16: (a) Honeycomb pore structure of Au-NAA; (b) the SERS spectra for the detection of (i) cresyl violet and (ii) rhodamine 6G [60].

in microfluidic channel for detection of alkylthiol binding by optical biosensor using RIS system (Figure 17).

**5.6. Detection of Circulating Tumor Cells.** Kumeria et al. developed label-free microfluidic channel based biosensor on Au-NAA for the detection of circulating tumor cells (CTC) by reflectrometric interference spectroscopy [93–96]. Biotinylated anti-EpCAM was immobilized on the NAA surface through multiple chemical steps followed by integrating the porous NAA substrate into the microfluidic device. Spiked tumor cells in PBS and whole blood samples were injected into the device and captured with high efficiency by using interferometric spectroscopy. The fabricated NAA has pore diameter and lengths of  $32 \pm 3 \text{ nm}$  and  $4 \pm 0.2 \mu\text{m}$ , respectively. The sensor surface was coated with ultra-thin Au layer of 8 nm by thermal vapor deposition technique. Multistep surface modification was adopted: Au-NAA were soaked in 10 mM solution of mercaptoundecanoic acid (MUA) in order to bind it covalently onto the sensor surface, followed by soaking in solution containing streptavidin molecules at  $100 \mu\text{g/mL}$  concentration where streptavidin binds to MUA.

Further, the streptavidin functionalized substrate was incubated in  $50 \mu\text{g/mL}$  of anti-EpCAM antibody in PBS buffer solution. The PMMA based microfluidic chip was obtained by computer numerically controlled (CNC) micromachining method. This microfluidic chip was formed with two channels with sensing platform for Au coated NAA substrate on the glass substrate. The working principle of detection involves the use of white light emitted from optical fiber probe which was focused on anti-EpCAM modified sensor substrate incorporated in the chip and light was reflected back from the surface into the same optical fiber probe system. The change in effective optical thickness on sensor surface was attributed to the change in RI of the surface. The RIS signals were obtained after the flow of CTCs into the channels, due to binding of CTCs onto anti-EpCAM functionalized Au-NAA substrate. The effective optical thickness was increased due to continuous binding of CTCs onto anti-EpCAM coated sensor surface. The interferometric signals were changed a bit due to unbound CTCs which were removed from the surface after washing. The detection limit of CTCs was found to be less than 1000 cells/mL, which is significant in practical

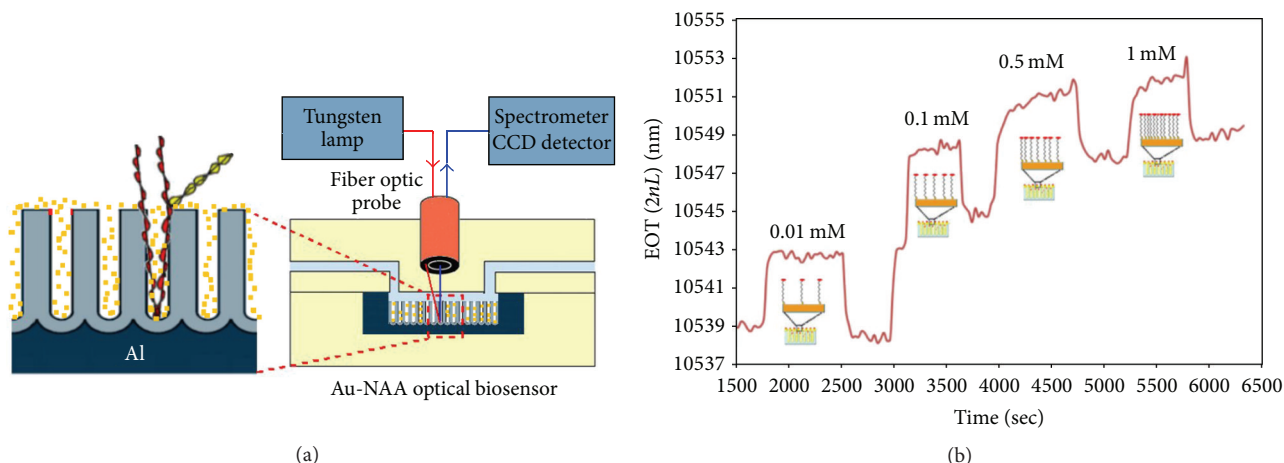


FIGURE 17: (a) Au-NAA placed in microfluidic chip as a biosensor for the detection of alkyl thiol molecule using reflective interferometric spectroscopy; (b) the real-time measurement of concentration with respect to effective optical thickness of on adsorption molecules on Au-NAA [61].

applications and clinical diagnosis. It was also observed that, when the flow rate of CTCs was higher, there was no notable increase in effective optical thickness whereas, when the flow rate was low, effective optical thickness was enhanced by slow ascend and continuing the number of CTCs increment on the sensor surface.

**5.7. Optical Properties of Au-NAA.** The optical properties of Au-NAA for the application in biosensing by using reflectance spectroscopy have been developed by Hernández-Eguía et al. [97]. NAA substrates were fabricated with various porosities in the range of 14 to 70%. The expected pore diameters were in the range 38.6 to 90 nm, on which 20 nm Au was coated by sputtering method. The prepared Au-NAA samples were analyzed by reflectance spectroscopy and Fabry-Perot interferences (FI). The interference fringes consist of NAA film and are surrounded by the incident medium of air and the substrates were observed. The FI depends on RI of the material; that is, FI was increased upon increase in RI of Au-NAA substrate, whereas, noncoated NAA samples showed decrease in FI due to less RI compared to Au-NAA. The study on controlled thickness of gold layer was performed to obtain better reflectance spectra in the infra-red region. Thus, by controlling the thickness of the gold layer on NAA surface the better performance of the material can be achieved in terms of sensitivity.

## 6. Aluminum Coated NAA (NAA/Al) Biosensor

**6.1. Detection of Protein.** Further, the improved label-free optical wave guide biosensor based NAA/Al multilayer film has been developed by Hotta et al. for the detection of BSA through optical wave guide spectroscopy [62]. The wave guide experiment was functioned by measuring the reflection spectra of multilayer thin films using Kretschmann configuration. The multilayer film was fitted with glass prism and xenon lamp was used to irradiate the light onto

prism. The incident light was slightly adjusted on prism by polarizer. Then, the reflected light was collected in photonic multichannel analyzer. A polydimethylsiloxane (PDMS) flow cell has been used to flow the analyte solution on multilayer film sensor. The irradiated light was incident on analyte solution and reflected spectra have been used for detection of analyte. The different structures of NAA/Al multilayer films were obtained by varying the substrate thickness. Al films which have been coated on glass substrate with thickness of 180 nm by thermal evaporation and films were anodized with formation of 34% porosity, and obtained pore diameter and lengths were of 39 and 220 nm, respectively (film a). Similarly, the same deposition method was used to fabricate Al film of thickness 500 nm and it was anodized with formation of 45% porosity to get cylindrical pore structured film of diameter and lengths of at 33 and 670 nm, respectively (film b). For the adsorption of BSA on NAA/Al film structures, the films were rinsed in mixture of prostate specific antigen and BSA solutions. The adsorption of BSA has been analyzed with respect to change in reflectivity on NAA/Al multilayer films. The reflectivity increased due to higher RI by increasing the concentration of BSA on film b compared to film a surface. However, it was found that film b was highly red shifted for the adsorption of BSA due to higher surface area, high porosity, and larger pore length with pore size compared to film a. Thus, the sensitivity was more for multilayer structure of film b over film a. Schematic diagram and working principle of detection of BSA on sensor substrate using optical waveguide spectroscopy and graph showing binding on substrate versus concentration of BSA in the solution phase were shown in Figure 18.

Similarly, Yamaguchi et al. fabricated NAA/Al multilayer thin film on glass substrate for detection of binding interaction of different molecules using optical wave guide sensor mechanism [98]. Thus, the sensitivity depends on change in the RI of sensor material where analyte molecules were immobilized on their surfaces. The optical wave guide

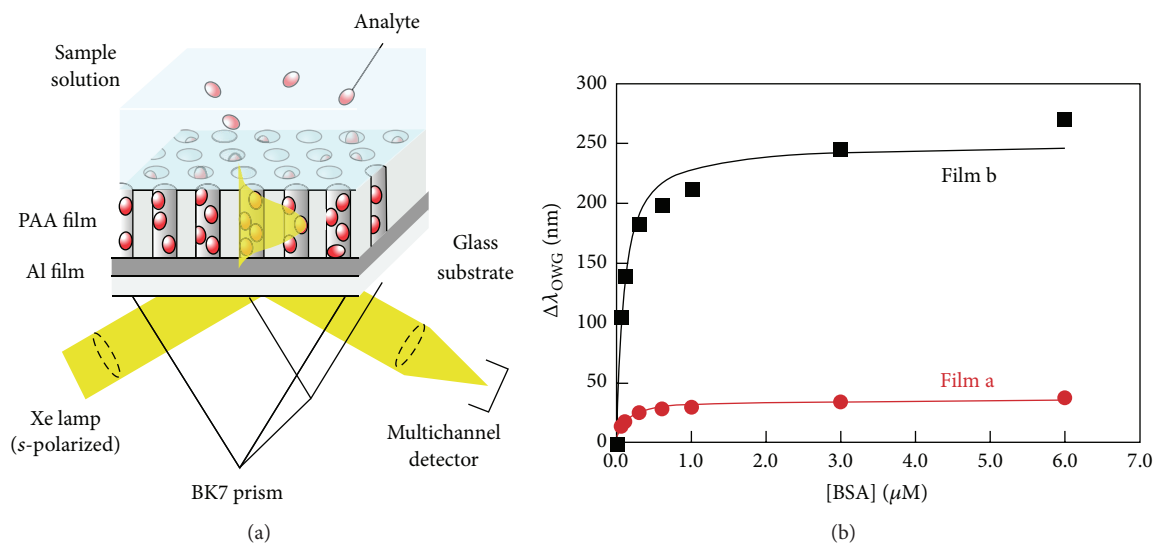


FIGURE 18: (a) Working principle for the detection of BSA by optical wave guide spectroscopy; (b) shift in the binding on substrate versus the concentration of BSA in the solution phase for film a and film b [62].

sensor got great attention as the small changes in RI of material can be detected; that is, the sensor could detect lower concentration of samples.

## 7. Platinum Coated NAA (Pt-NAA) Biosensor

**7.1. Detection of Binding of Prostate Specific Antigen.** An et al. developed Pt-NAA biosensor for the improvement of prostate specific antigen binding on sensor surface in interferometric method through pore widening [99]. Earlier same group reported pore widening method on porous Si where less sensitivity was observed [100]. However, the experiment of Pt-NAA biosensor has improved the sensitivity through fabrication of pore widening structure on NAA. The Pt-NAA was silanized by APTES solution and later this substrate was treated with Prolinker-A solution for binding of biomolecules onto the surface. The Prolinker-A modified sensor surface was bound with prostate specific antigen. The detection of antigen by pore widening on sensor surface by the prostate specific antigen solution of 100 ng/mL treated with Pt-NAA surface reveals that higher wavelength means rapid detection of binding of antigen molecules on sensor surface. The effective optical thickness has been increased with respect to pore widening on Pt-NAA biosensor surface which is due to larger antigen molecules occupied and bound to Prolinker-A on larger pore and the optical signals were enhanced to get rapid detection through interferometric spectroscopy. Overall, it was found that biosensing of NAA, Au-NAA, Al-NAA, and Pt-NAAs showed better sensitivity towards targets analyzed using different spectroscopy techniques. In NAA, targets were immobilized on their surfaces *via* binding with antigen-antibody. However, NAA shows less sensitivity compared to other substrates which has been enhanced by shrinking the pore size of Al, Au, and Pt coated NAA. Further, Au-NAA was chosen for biosensing application due to their

higher refractive index, surface plasmon, and biocompatibility compared to NAA, Al-NAA, and Pt-NAA. Au-NAA was able to detect biomolecules at very low concentration of 100 ng/mL. In the case of NAA and Al-NAA for the analysis of biomolecules, the concentration was set to be of 0.1/1 mg mL<sup>-1</sup>. The targets were immobilized by covalently binding with antigen-antibody on Au-NAA surface for rapid detection. Lastly, Pt-NAA have better sensitivity compared to Au-NAA but the cost effectiveness of platinum hinders the usage in commercialization purpose.

## 8. Conclusion

In this review, past and recent progress on surface modification and development of NAA platform by the anodization process for suitable biosensing applications have been discussed. By controlling the parameters such as applied voltage, selection of acids, anodization time, and temperature, the precise and highly porous structure of NAA substrates can be fabricated. The methods combined with analytical techniques provide great benefits in terms of technological aspects in biosensors field. Further, the sensitivity and better performance of NAA substrates can be enhanced by coating with gold nanoparticles and also by incorporating with microfluidic devices. However, some process to immobilize biomolecule on substrates requires selected buffer solutions, and some buffer solutions can damage the NAA substrate depending on the pH level, so the immobilization process may not occur on NAA surfaces which hinders the biosensing process. We believe that in future, the improvement of NAA sensor and modern NAA based sensing platforms will give better results. Further, this review reports sensing mechanism of various kinds of NAA to immobilized biomolecules at lower concentration which was examined by using several spectroscopic techniques.

## Competing Interests

The authors declare that there is no conflict of interests regarding the publication of this paper.

## Acknowledgments

The authors would like to acknowledge the DST Nanomission (SR/NM/NS-20/2014), India, DST (DST-TM-WTI-2K14-213), India, and SERB-DST (YSS/2015/000013), India, for financial support. The authors also would like to thank Jain University, Bangalore, India, for infrastructural support.

## References

- [1] I. Sorina, I. Gheorghe, M. Victor, and P. Radu Robert, "Nanostructured zirconia layers as thermal barrier coatings," *Incas Bulletin*, vol. 3, no. 3, pp. 63–69, 2011.
- [2] R. Kumar, O. Al-Dossary, G. Kumar, and A. Umar, "Zinc oxide nanostructures for NO<sub>2</sub> gas-sensor applications: a review," *Nano-Micro Letters*, vol. 7, no. 2, pp. 97–120, 2014.
- [3] K. Fan, W. Zhang, T. Peng, J. Chen, and F. Yang, "Application of TiO<sub>2</sub> fusiform nanorods for dye-sensitized solar cells with significantly improved efficiency," *The Journal of Physical Chemistry C*, vol. 115, no. 34, pp. 17213–17219, 2011.
- [4] J. Estelrich, E. Escribano, J. Queralt, and M. A. Busquets, "Iron oxide nanoparticles for magnetically-guided and magnetically-responsive drug delivery," *International Journal of Molecular Sciences*, vol. 16, no. 4, pp. 8070–8101, 2015.
- [5] G. S. Demirer, A. C. Okur, and S. Kizilel, "Synthesis and design of biologically inspired biocompatible iron oxide nanoparticles for biomedical applications," *Journal of Materials Chemistry B*, vol. 3, no. 40, pp. 7831–7849, 2015.
- [6] R. Li, L. Zhang, and P. Wang, "Rational design of nanomaterials for water treatment," *Nanoscale*, vol. 7, no. 41, pp. 17167–17194, 2015.
- [7] S. Ghoshal, A. A. Ansar, S. O. Raja et al., "Superparamagnetic iron oxide nanoparticle attachment on array of micro test tubes and microbeakers formed on p-type silicon substrate for biosensor applications," *Nanoscale Research Letters*, vol. 6, article 540, 8 pages, 2011.
- [8] J. L. Vivero-Escoto and Y.-T. Huang, "Inorganic-organic hybrid nanomaterials for therapeutic and diagnostic imaging applications," *International Journal of Molecular Sciences*, vol. 12, no. 6, pp. 3888–3927, 2011.
- [9] J. W. Kemling, A. J. Qavi, R. C. Bailey, and K. S. Suslick, "Nanostructured substrates for optical sensing," *The Journal of Physical Chemistry Letters*, vol. 2, no. 22, pp. 2934–2944, 2011.
- [10] Y. Liu, P. Kirchesch, T. Graule, A. Liersch, and F. Clemens, "Nanoparticle prepared mechanically stable hierarchically porous silica granulates and their application as oxygen carrier supports for chemical looping combustion," *Journal of Materials Chemistry A*, vol. 3, no. 22, pp. 11863–11873, 2015.
- [11] M. Ge, J. Rong, X. Fang, A. Zhang, Y. Lu, and C. Zhou, "Scalable preparation of porous silicon nanoparticles and their application for lithium-ion battery anodes," *Nano Research*, vol. 6, no. 3, pp. 174–181, 2013.
- [12] L. A. Osminkina, V. A. Sivakov, G. A. Mysov et al., "Nanoparticles prepared from porous silicon nanowires for bio-imaging and sonodynamic therapy," *Nanoscale Research Letters*, vol. 9, no. 1, article 463, 2014.
- [13] F. Keller, M. S. Hunter, and D. L. Robinson, "Structural features of oxide coatings on aluminum," *Journal of The Electrochemical Society*, vol. 100, no. 9, pp. 411–419, 1953.
- [14] A. Thormann, N. Teuscher, M. Pfannmöller, U. Rothe, and A. Heilmann, "Nanoporous aluminum oxide membranes for filtration and biofunctionalization," *Small*, vol. 3, no. 6, pp. 1032–1040, 2007.
- [15] T. Kumeria, M. M. Rahman, A. Santos, J. Ferré-Borrull, L. F. Marsal, and D. Losic, "Structural and optical nanoengineering of nanoporous anodic alumina rugate filters for real-time and label-free biosensing applications," *Analytical Chemistry*, vol. 86, no. 3, pp. 1837–1844, 2014.
- [16] G. Macias, L. P. Hernández-Eguía, J. Ferré-Borrull, J. Pallares, and L. F. Marsal, "Gold-coated ordered nanoporous anodic alumina bilayers for future label-free interferometric biosensors," *ACS Applied Materials & Interfaces*, vol. 5, no. 16, pp. 8093–8098, 2013.
- [17] K. Noh, K. S. Brammer, C. Choi, S. H. Kim, C. J. Frandsen, and S. Jin, "A new nano-platform for drug release via nanotubular aluminum oxide," *Journal of Biomaterials and Nanobiotechnology*, vol. 2, no. 3, pp. 226–233, 2011.
- [18] C. Jeong, J. Lee, K. Sheppard, and C.-H. Choi, "Air-impregnated nanoporous anodic aluminum oxide layers for enhancing the corrosion resistance of aluminum," *Langmuir*, vol. 31, no. 40, pp. 11040–11050, 2015.
- [19] C.-C. Lu, Y.-S. Huang, J.-W. Huang, C.-K. Chang, and S.-P. Wu, "A macroporous TiO<sub>2</sub> oxygen sensor fabricated using anodic aluminium oxide as an etching mask," *Sensors*, vol. 10, no. 1, pp. 670–683, 2010.
- [20] Q. Zhang, J. Xu, F. Fan et al., "Application of porous anodic alumina monolith catalyst in steam reforming of dimethyl ether: Cu/ $\gamma$ -Al<sub>2</sub>O<sub>3</sub>/Al catalyst degradation behaviors and catalytic activity improvement by pre-competition impregnation method," *Fuel Processing Technology*, vol. 119, pp. 52–59, 2014.
- [21] N. V. Gaponenko, T. I. Orekhovskaya, I. A. Nikolaenko et al., "Titanium oxide xerogel films in porous aluminum oxide for photocatalytic application," *Journal of Applied Spectroscopy*, vol. 77, no. 3, pp. 432–436, 2010.
- [22] C. S. Law, A. Santos, T. Kumeria, and D. Losic, "Engineered therapeutic-releasing nanoporous anodic alumina-aluminum wires with extended release of therapeutics," *ACS Applied Materials and Interfaces*, vol. 7, no. 6, pp. 3846–3853, 2015.
- [23] L. Wang, X. Qin, D. Ji et al., "Engineering optical properties of metal/porous anodic alumina films for refractometric sensing," *Applied Surface Science*, vol. 355, pp. 139–144, 2015.
- [24] S. D. Kulkarni, K. Choudhari, and C. Santhosh, "Optical interferometric properties of iridescent nanoporous anodic alumina," *Procedia Materials Science*, vol. 5, pp. 988–994, 2014.
- [25] J. Deng and C.-S. Toh, "Impedimetric DNA biosensor based on a nanoporous alumina membrane for the detection of the specific oligonucleotide sequence of dengue virus," *Sensors*, vol. 13, no. 6, pp. 7774–7785, 2013.
- [26] A. R. Walpole, E. P. Briggs, M. Karlsson, E. Pålsgård, and P. R. Wilshaw, "Nano-porous alumina coatings for improved bone implant interfaces," *Materialwissenschaft und Werkstofftechnik*, vol. 34, no. 12, pp. 1064–1068, 2003.
- [27] T. Kumeria, J. Yu, M. Alsawat et al., "Photoswitchable membranes based on peptide-modified nanoporous anodic alumina: toward smart membranes for on-demand molecular transport," *Advanced Materials*, vol. 27, no. 19, pp. 3019–3024, 2015.
- [28] Y. Fan, K. Hotta, A. Yamaguchi et al., "Highly sensitive real-time detection of DNA hybridization by using nanoporous

- waveguide fluorescence spectroscopy," *Applied Physics Letters*, vol. 105, no. 3, Article ID 031103, 2014.
- [29] N. N. Bwana, "Synthesis of highly ordered nanopores on alumina by two-step anodization process," *Journal of Nanoparticle Research*, vol. 10, no. 2, pp. 313–319, 2008.
- [30] H. Masuda and K. Fukuda, "Ordered metal nanohole arrays made by a two-step replication of honeycomb structures of anodic alumina," *Science*, vol. 268, no. 5216, pp. 1466–1468, 1995.
- [31] J.-H. Zhou, J.-P. He, G.-W. Zhao, C.-X. Zhang, J.-S. Zhao, and H.-P. Hu, "Alumina nanostructures prepared by two-step anodization process," *Transactions of Nonferrous Metals Society of China*, vol. 17, no. 1, pp. 82–86, 2007.
- [32] H. Masuda, F. Hasegawa, and S. Ono, "Self-ordering of cell arrangement of anodic porous alumina formed in sulfuric acid solution," *Journal of the Electrochemical Society*, vol. 144, no. 5, pp. L127–L130, 1997.
- [33] H. Masuda, M. Ohya, H. Asoh, M. Nakao, M. Nohtomi, and T. Tamamura, "Photonic crystal using anodic porous alumina," *Japanese Journal of Applied Physics*, vol. 38, no. 12, pp. L1403–L1405, 1999.
- [34] W. Lee, R. Ji, U. Gösele, and K. Nielsch, "Fast fabrication of long-range ordered porous alumina membranes by hard anodization," *Nature Materials*, vol. 5, no. 9, pp. 741–747, 2006.
- [35] D. Losic and A. Santos, *Nanoporous Alumina: Fabrication, Structure, Properties and Applications*, vol. 219 of *Springer Series in Material Science*, Springer, New York, NY, USA, 2015.
- [36] F. Li, L. Zhang, and R. M. Metzger, "On the growth of highly ordered pores in anodized aluminum oxide," *Chemistry of Materials*, vol. 10, no. 9, pp. 2470–2480, 1998.
- [37] W. Lee and S.-J. Park, "Porous anodic aluminum oxide: anodization and templated synthesis of functional nanostructures," *Chemical Reviews*, vol. 114, no. 15, pp. 7487–7556, 2014.
- [38] W. Shi, Y. Shen, D. Ge et al., "Functionalized anodic aluminum oxide (AAO) membranes for affinity protein separation," *Journal of Membrane Science*, vol. 325, no. 2, pp. 801–808, 2008.
- [39] S. Kipke and G. Schmid, "Nanoporous alumina membranes as diffusion controlling systems," *Advanced Functional Materials*, vol. 14, no. 12, pp. 1184–1188, 2004.
- [40] A. Santos, P. Formentín, J. Pallarès, J. Ferré-Borrull, and L. F. Marsal, "Structural engineering of nanoporous anodic alumina funnels with high aspect ratio," *Journal of Electroanalytical Chemistry*, vol. 655, no. 1, pp. 73–78, 2011.
- [41] F. Patel, M. A. Baig, and T. Laoui, "Processing of porous alumina substrate for multilayered ceramic filter," *Desalination and Water Treatment*, vol. 35, no. 1–3, pp. 33–38, 2011.
- [42] Y. Tokudome, K. Nakanishi, K. Kanamori, K. Fujita, H. Akamatsu, and T. Hanada, "Structural characterization of hierarchically porous alumina aerogel and xerogel monoliths," *Journal of Colloid and Interface Science*, vol. 338, no. 2, pp. 506–513, 2009.
- [43] J. Martín, M. Martín-González, J. Francisco Fernández, and O. Caballero-Calero, "Ordered three-dimensional interconnected nanoarchitectures in anodic porous alumina," *Nature Communications*, vol. 5, article 5130, 2014.
- [44] A. Santos, T. Kumeria, Y. Wang, and D. Losic, "In situ monitored engineering of inverted nanoporous anodic alumina funnels: on the precise generation of 3D optical nanostructures," *Nanoscale*, vol. 6, no. 17, pp. 9991–9999, 2014.
- [45] Y. C. Sui, B. Z. Cui, R. Guardián, D. R. Acosta, L. Martínez, and R. Perez, "Growth of carbon nanotubes and nanofibres in porous anodic alumina film," *Carbon*, vol. 40, no. 7, pp. 1011–1016, 2002.
- [46] S. Wang, G. J. Yu, J. L. Gong, D. Z. Zhu, and H. H. Xia, "Large-area uniform nanodot arrays embedded in porous anodic alumina," *Nanotechnology*, vol. 18, no. 1, Article ID 015303, 2007.
- [47] G. E. J. Poinern, X. T. Le, M. Hager, T. Becker, and D. Fawcett, "Electrochemical synthesis, characterisation, and preliminary biological evaluation of an anodic aluminium oxide membrane with a pore size of 100 nanometres for a potential cell culture substrate," *American Journal of Biomedical Engineering*, vol. 3, no. 6, pp. 119–131, 2013.
- [48] N. Verma, K. C. Singh, and J. Jindal, "Fabrication of nanomaterials on porous anodic alumina template using various techniques," *Indian Journal of Advances in Chemical Science*, vol. 3, no. 3, pp. 235–246, 2015.
- [49] K. Kant, J. Yu, C. Priest, J. G. Shapter, and D. Losic, "Impedance nanopore biosensor: influence of pore dimensions on biosensing performance," *Analyst*, vol. 139, no. 5, pp. 1134–1140, 2014.
- [50] S. D. Alvarez, C.-P. Li, C. E. Chiang, I. K. Schuller, and M. J. Sailor, "A label-free porous alumina interferometric immunosensor," *ACS Nano*, vol. 3, no. 10, pp. 3301–3307, 2009.
- [51] K. Hotta, A. Yamaguchi, and N. Teramae, "Deposition of polyelectrolyte multilayer film on a nanoporous alumina membrane for stable label-free optical biosensing," *The Journal of Physical Chemistry C*, vol. 116, no. 44, pp. 23533–23539, 2012.
- [52] Y. Chen, A. Santos, Y. Wang et al., "Biomimetic nanoporous anodic alumina distributed bragg reflectors in the form of films and microsized particles for sensing applications," *ACS Applied Materials and Interfaces*, vol. 7, no. 35, pp. 19816–19824, 2015.
- [53] F. S. H. Krismastuti, H. Bayat, N. H. Voelcker, and H. Schönherr, "Real time monitoring of layer-by-layer polyelectrolyte deposition and bacterial enzyme detection in nanoporous anodized aluminum oxide," *Analytical Chemistry*, vol. 87, no. 7, pp. 3856–3863, 2015.
- [54] A. Santos, G. Macías, J. Ferré-Borrull, J. Pallarès, and L. F. Marsal, "Photoluminescent enzymatic sensor based on nanoporous anodic alumina," *ACS Applied Materials & Interfaces*, vol. 4, no. 7, pp. 3584–3588, 2012.
- [55] A. Dhathathreyan, "Real-time monitoring of invertase activity immobilized in aluminum oxide-nanoporous," *The Journal of Physical Chemistry B*, vol. 115, no. 20, pp. 6678–6682, 2011.
- [56] M. Nemati, A. Santos, T. Kumeria, and D. Losic, "Label-free real-time quantification of enzyme levels by interferometric spectroscopy combined with gelatin-modified nanoporous anodic alumina photonic films," *Analytical Chemistry*, vol. 87, no. 17, pp. 9016–9024, 2015.
- [57] S.-H. Yeom, O.-G. Kim, B.-H. Kang et al., "Highly sensitive nano-porous lattice biosensor based on localized surface plasmon resonance and interference," *Optics Express*, vol. 19, no. 23, pp. 22882–22891, 2011.
- [58] H. M. Hiep, H. Yoshikawa, and E. Tamiya, "Interference localized surface plasmon resonance nanosensor tailored for the detection of specific biomolecular interactions," *Analytical Chemistry*, vol. 82, no. 4, pp. 1221–1227, 2010.
- [59] D.-K. Kim, K. Kerman, M. Saito et al., "Label-free DNA biosensor based on localized surface plasmon resonance coupled with interferometry," *Analytical Chemistry*, vol. 79, no. 5, pp. 1855–1864, 2007.
- [60] G. Das, N. Patra, A. Gopalakrishnan et al., "Fabrication of large-area ordered and reproducible nanostructures for SERS biosensor application," *Analyst*, vol. 137, no. 8, pp. 1785–1792, 2012.

- [61] T. Kumeria and D. Losic, "Controlling interferometric properties of nanoporous anodic aluminium oxide," *Nanoscale Research Letters*, vol. 7, article 88, 2012.
- [62] K. Hotta, A. Yamaguchi, and N. Teramae, "Nanoporous waveguide sensor with optimized nanoarchitectures for highly sensitive label-free biosensing," *ACS Nano*, vol. 6, no. 2, pp. 1541–1547, 2012.
- [63] A. Yin, M. Tzolov, D. Cardimona, L. Guo, and J. Xu, "Fabrication of highly ordered anodic aluminium oxide templates on silicon substrates," *IET Circuits, Devices and Systems*, vol. 1, no. 3, pp. 205–209, 2007.
- [64] D. Lo and R. A. Budiman, "Fabrication and characterization of porous anodic alumina films from impure aluminum foils," *Journal of the Electrochemical Society*, vol. 154, no. 1, pp. C60–C66, 2007.
- [65] T. Nagaura, F. Takeuchi, and S. Inoue, "Fabrication and structural control of anodic alumina films with inverted cone porous structure using multi-step anodizing," *Electrochimica Acta*, vol. 53, no. 5, pp. 2109–2114, 2008.
- [66] T. Hussain, A. T. Shah, K. Shehzad et al., "Formation of self-ordered porous anodized alumina template for growing tungsten trioxide nanowires," *International Nano Letters*, vol. 5, no. 1, pp. 37–41, 2015.
- [67] H.-C. Na, T.-J. Sung, S.-H. Yoon et al., "Formation of unidirectional nanoporous structures in thickly anodized aluminum oxide layer," *Transactions of Nonferrous Metals Society of China*, vol. 19, no. 4, pp. 1013–1017, 2009.
- [68] H. Tsuchiya, S. Berger, J. M. Macak, A. G. Muñoz, and P. Schmuki, "A new route for the formation of self-organized anodic porous alumina in neutral electrolytes," *Electrochemistry Communications*, vol. 9, no. 4, pp. 545–550, 2007.
- [69] H. Asoh, K. Nishio, M. Nakao, A. Yokoo, T. Tamamura, and H. Masuda, "Fabrication of ideally ordered anodic porous alumina with 63 nm hole periodicity using sulfuric acid," *Journal of Vacuum Science & Technology B*, vol. 19, no. 2, pp. 569–572, 2001.
- [70] F. Zhang, X. Liu, C. Pan, and J. Zhu, "Nano-porous anodic aluminium oxide membranes with 6–19 nm pore diameters formed by a low-potential anodizing process," *Nanotechnology*, vol. 18, no. 34, Article ID 345302, 2007.
- [71] Y. Wang, A. Santos, A. Evdokiou, and D. Losic, "Rational design of ultra-short anodic alumina nanotubes by short-time pulse anodization," *Electrochimica Acta*, vol. 154, pp. 379–386, 2015.
- [72] A. L. Friedman, D. Brittain, and L. Menon, "Roles of pH and acid type in the anodic growth of porous alumina," *The Journal of Chemical Physics*, vol. 127, no. 15, Article ID 154717, 2007.
- [73] J. Ferré-Borrull, J. Pallarès, G. Macías, and L. F. Marsal, "Nanostructural engineering of nanoporous anodic alumina for biosensing applications," *Materials*, vol. 7, no. 7, pp. 5225–5253, 2014.
- [74] T. Kumeria, A. Santos, and D. Losic, "Nanoporous anodic alumina platforms: engineered surface chemistry and structure for optical sensing applications," *Sensors*, vol. 14, no. 7, pp. 11878–11918, 2014.
- [75] A. Santos, T. Kumeria, and D. Losic, "Nanoporous anodic aluminum oxide for chemical sensing and biosensors," *TrAC—Trends in Analytical Chemistry*, vol. 44, pp. 25–38, 2013.
- [76] A. Santos, T. Kumeria, and D. Losic, "Nanoporous anodic alumina: a versatile platform for optical biosensors," *Materials*, vol. 7, no. 6, pp. 4297–4320, 2014.
- [77] A. Santos, V. S. Balderrama, M. Alba et al., "Nanoporous anodic alumina barcodes: toward smart optical biosensors," *Advanced Materials*, vol. 24, no. 8, pp. 1050–1054, 2012.
- [78] A. Santos, V. S. Balderrama, M. Alba et al., "Tunable fabry-pérot interferometer based on nanoporous anodic alumina for optical biosensing purposes," *Nanoscale Research Letters*, vol. 7, no. 1, article 370, pp. 1–10, 2012.
- [79] A. Santos, T. Kumeria, and D. Losic, "Optically optimized photoluminescent and interferometric biosensors based on nanoporous anodic alumina: a comparison," *Analytical Chemistry*, vol. 85, no. 16, pp. 7904–7911, 2013.
- [80] P. Takmakov, I. Vlasiouk, and S. Smirnov, "Application of anodized aluminum in fluorescence detection of biological species," *Analytical and Bioanalytical Chemistry*, vol. 385, no. 5, pp. 954–958, 2006.
- [81] I. Vlasiouk, A. Krasnoslobodtsev, S. Smirnov, and M. Germann, "'Direct' detection and separation of DNA using nanoporous alumina filters," *Langmuir*, vol. 20, no. 23, pp. 9913–9915, 2004.
- [82] C. Fu, Y. Gu, Z. Wu, Y. Wang, S. Xu, and W. Xu, "Surface-enhanced Raman scattering (SERS) biosensing based on nanoporous dielectric waveguide resonance," *Sensors and Actuators B: Chemical*, vol. 201, pp. 173–176, 2014.
- [83] K. H. A. Lau, L.-S. Tan, K. Tamada, M. S. Sander, and W. Knoll, "Highly sensitive detection of processes occurring inside nanoporous anodic alumina templates: a waveguide optical study," *Journal of Physical Chemistry B*, vol. 108, no. 30, pp. 10812–10818, 2004.
- [84] S. Pan and L. J. Rothberg, "Interferometric sensing of biomolecular binding using nanoporous aluminum oxide templates," *Nano Letters*, vol. 3, no. 6, pp. 811–814, 2003.
- [85] P. Takmakov, I. Vlasiouk, and S. Smirnov, "Hydrothermally shrunk alumina nanopores and their application to DNA sensing," *Analyst*, vol. 131, no. 11, pp. 1248–1253, 2006.
- [86] M. P. Nicholas, L. Rao, and A. Gennerich, "Covalent immobilization of microtubules on glass surfaces for molecular motor force measurements and other single-molecule assays," *Methods in Molecular Biology*, vol. 1136, pp. 137–169, 2014.
- [87] J.-M. Moon, D. Akin, Y. Xuan, P. D. Ye, P. Guo, and R. Bashir, "Capture and alignment of phi29 viral particles in sub-40 nanometer porous alumina membranes," *Biomedical Microdevices*, vol. 11, no. 1, pp. 135–142, 2009.
- [88] M. Darder, P. Aranda, M. Hernández-Vélez, E. Manova, and E. Ruiz-Hitzky, "Encapsulation of enzymes in alumina membranes of controlled pore size," *Thin Solid Films*, vol. 495, no. 1–2, pp. 321–326, 2006.
- [89] A. Hierro-Rodriguez, P. Rocha-Rodrigues, F. Valdés-Bango et al., "On the anodic aluminium oxide refractive index of nanoporous templates," *Journal of Physics D: Applied Physics*, vol. 48, no. 45, Article ID 455105, 2015.
- [90] D.-K. Kim, K. Kerman, H. M. Hiep et al., "Label-free optical detection of aptamer-protein interactions using gold-capped oxide nanostructures," *Analytical Biochemistry*, vol. 379, no. 1, pp. 1–7, 2008.
- [91] C. Toccafondi, R. La Rocca, A. Scarpellini, M. Salerno, G. Das, and S. Dante, "Thin nanoporous alumina-based SERS platform for single cell sensing," *Applied Surface Science*, vol. 351, pp. 738–745, 2015.
- [92] C. Toccafondi, S. Thorat, R. La Rocca et al., "Multifunctional substrates of thin porous alumina for cell biosensors," *Journal of Materials Science: Materials in Medicine*, vol. 25, no. 10, pp. 2411–2420, 2014.
- [93] T. Kumeria, M. D. Kurkuri, K. R. Diener, L. Parkinson, and D. Losic, "Label-free reflectometric interference microchip

- biosensor based on nanoporous alumina for detection of circulating tumour cells,” *Biosensors and Bioelectronics*, vol. 35, no. 1, pp. 167–173, 2012.
- [94] M. D. Kurkuri, F. Al-Ejeh, J. Y. Shi et al., “Plasma functionalized PDMS microfluidic chips: towards point-of-care capture of circulating tumor cells,” *Journal of Materials Chemistry*, vol. 21, no. 24, pp. 8841–8848, 2011.
- [95] P. Patil, Madhuprasad, T. Kumeria, D. Losic, and M. Kurkuri, “Isolation of circulating tumour cells by physical means in a microfluidic device: a review,” *RSC Advances*, vol. 5, no. 109, pp. 89745–89762, 2015.
- [96] B. Thierry, M. Kurkuri, J. Y. Shi, L. E. M. P. Lwin, and D. Palms, “Herceptin functionalized microfluidic polydimethylsiloxane devices for the capture of human epidermal growth factor receptor 2 positive circulating breast cancer cells,” *Biomicrofluidics*, vol. 4, no. 3, Article ID 032205, 2010.
- [97] L. P. Hernández-Eguía, J. Ferré-Borrull, G. Macias, J. Pallarès, and L. F. Marsal, “Engineering optical properties of gold-coated nanoporous anodic alumina for biosensing,” *Nanoscale Research Letters*, vol. 9, no. 1, article 414, 2014.
- [98] A. Yamaguchi, K. Hotta, and N. Teramae, “Optical waveguide sensor based on a porous anodic alumina/aluminum multilayer film,” *Analytical Chemistry*, vol. 81, no. 1, pp. 105–111, 2009.
- [99] H. C. An, J. Y. An, and B.-W. Kim, “Improvement of sensitivity in an interferometry by controlling pore size on the anodic aluminum oxide chip pore-widening technique,” *Korean Journal of Chemical Engineering*, vol. 26, no. 1, pp. 160–164, 2009.
- [100] A. Janshoff, K.-P. S. Dancil, C. Steinem et al., “Macroporous p-type silicon fabry-perot layers. Fabrication, characterization, and applications in biosensing,” *Journal of the American Chemical Society*, vol. 120, no. 46, pp. 12108–12116, 1998.

## Research Article

# Nanoporous Glasses for Nuclear Waste Containment

Thierry Woignier,<sup>1,2</sup> Juan Primera,<sup>3,4</sup> and Jérôme Reynes<sup>5</sup>

<sup>1</sup>Aix Marseille Université, Université d'Avignon, CNRS, IRD, IMBE, 13397 Marseille, France

<sup>2</sup>IRD-Campus Agro Environnemental Caraïbes, Le Lamentin, 97232 Martinique, France

<sup>3</sup>Departamento de Física, FEC, LUZ, Maracaibo 4011, Venezuela

<sup>4</sup>Escuela Superior Politécnica del Litoral (ESPOL), Facultad de Ciencias Naturales y Matemáticas, Departamento de Física, Campus Gustavo Galindo, Km 30.5 Via Perimetral, P.O. Box 09-01-5863, 090150 Guayaquil, Ecuador

<sup>5</sup>Laboratoire Charles Coulomb, Université Montpellier 2, Place E. Bataillon, 34095 Montpellier Cedex 5, France

Correspondence should be addressed to Thierry Woignier; [thierry.woignier@univ-montp2.fr](mailto:thierry.woignier@univ-montp2.fr)

Received 25 February 2016; Revised 23 June 2016; Accepted 10 July 2016

Academic Editor: Mahaveer Kurkuri

Copyright © 2016 Thierry Woignier et al. This is an open access article distributed under the Creative Commons Attribution License, which permits unrestricted use, distribution, and reproduction in any medium, provided the original work is properly cited.

Research is in progress to incorporate nuclear waste in new matrices with high structural stability, resistance to thermal shock, and high chemical durability. Interactions with water are important for materials used as a containment matrix for the radio nuclides. It is indispensable to improve their chemical durability to limit the possible release of radioactive chemical species, if the glass structure is attacked by corrosion. By associating high structural stability and high chemical durability, silica glass optimizes the properties of a suitable host matrix. According to an easy sintering stage, nanoporous glasses such as xerogels, aerogels, and composite gels are alternative ways to synthesize silica glass at relatively low temperatures ( $\approx 1,000$ – $1,200^\circ\text{C}$ ). Nuclear wastes exist as aqueous salt solutions and we propose using the open pore structure of the nanoporous glass to enable migration of the solution throughout the solid volume. The loaded material is then sintered, thereby trapping the radioactive chemical species. The structure of the sintered materials (glass ceramics) is that of nanocomposites: actinide phases ( $\sim 100$  nm) embedded in a vitreous silica matrix. Our results showed a large improvement in the chemical durability of glass ceramic over conventional nuclear glass.

## 1. Introduction

A number of materials have been considered to incorporate hazardous nuclear wastes such as ceramics, cements, metal matrices, and glasses [1–8]. Presently, the two best candidate materials are crystalline ceramics and glasses. Fixation of radioactive wastes in glasses has been shown to be a viable technological alternative for effective management of nuclear wastes. The advantages of the method are that a large number of elements can be incorporated into the glass structure and a small volume of solid waste is produced as a result [9]. In this process, the radioactive elements are mixed and melted with a glass frit [10]. However, to ensure long-term storage, long-life nuclear waste (actinides) has to be incorporated in a matrix with excellent chemical durability [11, 12]. Research is in progress to propose new matrices with high structural stability, good mechanical properties, and high chemical

durability. Titania-based minerals and zirconia-based glass ceramics, in which the crystalline phases are embedded in an aluminosilicate glass matrix, are possible candidates [3–5]. They consist of a highly durable crystalline phase homogeneously dispersed in a glass matrix that also has good chemical durability [6–8]. The titanite and zirconolite phases suggest that these matrices are highly corrosion resistant.

The properties of silica glasses, including good durability and mechanical strength and the ability to incorporate large concentrations of dopants, make them ideal candidates as matrices for the storage of nuclear waste. The main disadvantage of silica glasses for this kind of use is their high processing temperature of  $\sim 2,000^\circ\text{C}$ . However, it has been shown that the sol-gel process is an appropriate low temperature process to obtain glasses at around  $1,000^\circ\text{C}$ , not by melting but by sintering of a nanoporous amorphous silica gel [13–20]. In this paper, we compare different nanoporous silica

networks as possible host matrices for actinides and assess the feasibility of fixing actinides in silica glass. We characterize different families of porous glasses and examine the advantages and drawbacks of the different porous matrices. We focus on the mechanical properties and the permeability of the porous materials. These features depend on the pore volume, which can be adjusted using different parameters and processes including silica content, sintering, drying, and composite approach.

## 2. State of the Art

**2.1. Porous Glasses by Foaming or Leaching of Glasses.** The classical procedure for making glass includes a high temperature step that ensures that the raw materials are dissolved and have reacted. At that point, the amorphous structure of the liquid is preserved by quenching the melt. Standard glass is generally the result of a multistep process including melting the different oxides at a high temperature followed by refining and finally quenching. One possible way to prepare porous glass is to nucleate the bubbles inside the melt and then to quench it. The resulting glass is generally called “foamed glass” [21, 22]. The bubbles are obtained through the decomposition of carbonates during melting, but this process is not suitable for the preparation of high durability glass for the fixation of nuclear wastes. Another example of porous glass obtained in the standard way is microphase separated and leached “Vycor” glass [14, 23–25]. In this process, sodium borosilicate glass is heat-treated to induce phase separation. An acidic corrosion treatment will dissolve the “weak” borate phase and create continuous porosity in the silicate phase. The nanoporous glass can then be further sintered into vitreous silica glass at a temperature close to 1,200°C, instead of the 2,000°C required by the standard procedure [25]. The authors of this precursor method were the first to suggest confining nuclear wastes in the porosity [14]. The nuclear waste was fixed in the porous structure, after which the pores are collapsed. However this kind of glass is not pure silica but contains 3–5 percent of boron [14]. As boron is much more soluble in water than silica, its presence reduces the chemical durability of the glass.

**2.2. Standard Sol-Gel-Glass Route.** The high temperature step in the melting process for glass is avoided when the sol-gel route is used. The first step is the formation of a gel which generally involves the hydrolysis reaction of an organometallic compound ( $\text{Si}(\text{OR})_4$ ), dissolved in alcohol in the presence of water. By condensation reactions, two silanol groups give rise to siloxane bonds ( $\text{SiOSi}$ ) [13]. These two reactions lead to noncrystalline materials.

Different types of silica gels for the synthesis of glass are described in the literature [13, 15, 19, 20, 26, 27]. However, for impregnation experiments, the porous network has to be able to resist capillary stresses during the soaking steps. In porous materials, the mechanical properties depend on the load bearing fraction of the solid and decrease with an increase in pore volume [28]. On the other hand, pore volume increases permeability and improves waste loading [16]. A compromise is thus needed between the mechanical properties and

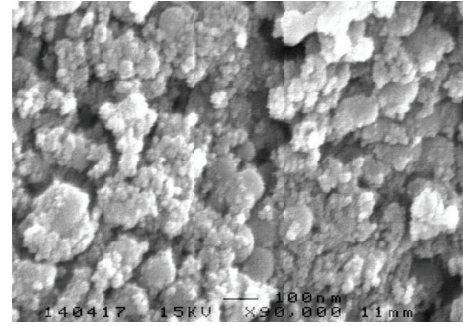


FIGURE 1: Scanning electron microscopy of xerogels.

permeability by controlling pore volume. The mechanical properties of the materials can be increased in different ways: (1) by collapsing the pore volume by drying, (2) by sintering, and (3) by using the composite approach.

**2.3. Collapsing the Pore Volume.** The result of gelation is a two-phase medium containing the solid network and the liquid (alcohol and water). Drying can be carried out at ambient temperature, but during the drying stage considerable shrinkage occurs which transforms the wet gel into a hard, dry, but nanoporous solid (pore range is close to 10 nm) called “xerogel.”

The drying procedure is crucial and must be extremely slow because otherwise it can lead to capillary phenomena that can destroy the gel network and break up the solid network. Alternative drying methods represent a favorable compromise between the capillary forces and the mechanical resistance of the gel network (strengthening the gel by reinforcement, reducing the surface tension, enlarging the pores, etc.) [13, 17]. To summarize, xerogels samples can be synthesized by careful control of the drying parameters. Xerogels (Figure 1) are porous glasses whose pore volume ranges from 30 to 70% and which mainly comprise micropores due to the collapse of the larger pores.

**2.4. Aerogels and Sintered Aerogels.** The goal of supercritical drying is to eliminate these capillary forces. The magnitude of the stresses depends on the interfacial energy of the liquid, and it is possible to eliminate capillary stresses if the pressure and the temperature go beyond the critical point of the liquid [29, 30]. The supercritical solvent is then isothermally evacuated by condensation outside the autoclave. After supercritical drying, the “aerogel” (Figure 2) is a solid material, amorphous but extremely porous (80–99% porosity) and very brittle [29].

One (among others) possible application of these very porous materials is as a glass precursor. The silica aerogels can be easily transformed into silicate glasses by a sequence of sintering treatments [15, 26, 31]. Sintering enhances the mechanical properties of aerogels. Depending on the duration of the heat treatment, microporosity is progressively eliminated [25, 32].

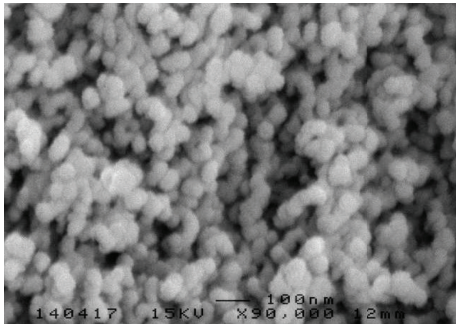


FIGURE 2: Scanning electron microscopy of aerogels.

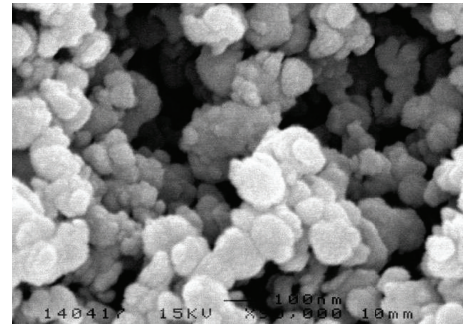


FIGURE 3: Scanning electron microscopy of typical composite aerogel.

**2.5. The Composite Approach.** Another important parameter is permeability. High permeability is usually an advantage because it means that the fluid and hence the chemical species of interest can easily migrate in the porous network and homogeneous distribution of the chemical species can be expected as a result. In ceramic science, it is generally accepted that the inclusion of particles or fibers improves the mechanical properties of composite ceramics and also modifies the porous structure (Figure 3). It is possible to adjust the density, the mechanical properties, the pore size distribution, and the permeability of the composite aerogels by adding silica powder (silica soot like aerosil OX50) to the monomer solution just before gelation [15, 31, 33].

To summarize, mechanical properties, capillary forces, and permeability are the most important parameters for filling the nanoporous glass network. These different kinds of porous materials can all be considered nanoporous glass even though the “glassy” state is achieved in very different ways. They will be tested as host matrix for nuclear waste containment. The actinides are simulated by lanthanides nitrates (Nd and Ce) in water, which diffuses by capillarity in the porous network. Guest molecules were deposited on the surface of the skeleton when the liquid was further evaporated. The mean pore size and the pore size distribution need to be tailored to facilitate homogeneous dispersion of doping molecules within the texture.

### 3. Experimental

**3.1. Nanoporous Glass Synthesis.** The silica porous glasses were synthesized from previously reported sol-gel techniques [13, 29, 33]. The silica gels were made from tetraethoxysilane (TEOS) hydrolyzed with distilled water and with ethanol as solvent. The mixture was stirred and aged one week at room temperature. After gelation the alcogels were transformed into xerogels or sintered aerogels.

For the xerogel samples, porosity is partially eliminated by controlled and slow drying [13]. These xerogels samples covered density between 0.5 and 1.6 g·cm<sup>-3</sup>.

Some gels are transformed into aerogels by supercritical drying performed at 305°C and 13 MPa [29]. The sintering of silica aerogels at high temperature (>1000°C) has been described previously [15, 26]. Depending on the duration of the heat treatment, the pores collapse and the bulk density

increases. These sintered aerogels porosity ranged from 95% to 0% (density between 0.1 and 2.2 g·cm<sup>-3</sup>).

Composite aerogels were synthesized using the same protocol as for previously published ones [16, 33]. TEOS was hydrolyzed with 15 mole of water (HCl 10<sup>-2</sup> M) per mole of TEOS for 1 h under stirring. Pyrogenic silica (aerosil OX 50) was added under stirring. The pH was adjusted to 4.5, which led to gelation in a few minutes. The proportion of aerosil with respect to the total silica weight ranged from 5% to 70%. The composite wet gels were transformed into composite aerogels by supercritical drying with ethanol. The density range is 0.25–0.5 g·cm<sup>-3</sup>.

**3.2. Experimental Techniques.** Bulk density ( $\rho$ ) was determined from direct measurements of weight and from the geometric dimensions of samples. Porosity ( $\phi$ ) was calculated from bulk density and skeletal density ( $\rho_s$ ). The skeletal density, measured by helium pycnometry, was  $\rho_s = 2 \text{ g/cm}^3$  [23].

Elastic modulus ( $E$ ) and rupture modulus ( $\sigma$ ) were measured by the three-point bending technique using an Instron 1196 mechanical testing machine (24 N load cell) [15, 28].

Toughness ( $K_{IC}$ ) was measured by the Single Edge Notched Beam technique [34] and  $a_c$  the critical flaw size was calculated from

$$a_c = \frac{(K_{IC}/\sigma)^2}{1.21\pi}. \quad (1)$$

Permeability ( $D$ ) was measured using a method of impregnation based on Archimedes' principle [8]. The samples are dipped in water and, during impregnation, the thickness of the penetrating water,  $h(t)$ , increases with time. We previously showed [8] that

$$D = \frac{\eta\phi h^2(t)}{2\Delta P \cdot t}, \quad (2)$$

where  $\Delta P$  is capillary pressure and  $\eta$  is water viscosity. We calculated  $D$  from the slope of the straight line  $h^2(t) = f(t)$ .  $D$  has the dimension of a surface and was expressed in nm<sup>2</sup>. The details of the technique are given in [16].

Microstructure was analysed by scanning electron microscopy (JEOL 1200EX 100 kV). A Jeol (JSM-66300F)

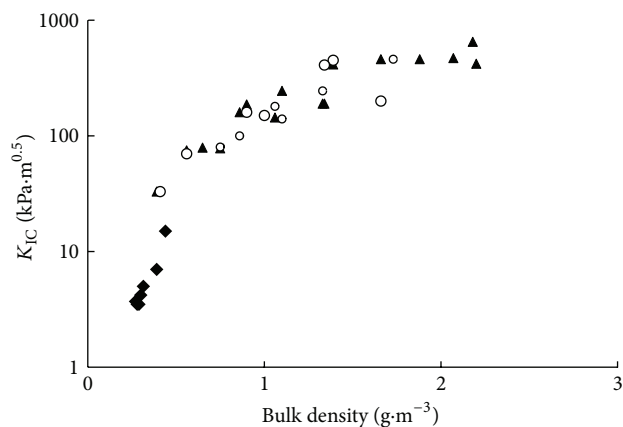


FIGURE 4: Toughness versus density for xerogels (circles), sintered aerogels (triangles), and composites aerogels (diamonds).

microscope was used to get the back-scattered electron micrographs.

The sintering was characterized by dilatometer (Adamel Lhomargy DII0.2) experiments in the temperature range 25–1300°C.

The crystalline phases were characterized by X-rays diffraction ( $\text{CuK}\alpha$ ) with a Phillips PW 1830.

The chemical durability of the glass ceramics was measured with a conventional Soxhlet device [15]. The test was conducted at 100°C, after 28 days of leaching. The normalized mass loss ( $\text{g}\cdot\text{m}^{-2}$ ) was calculated from analysis of the leachates.

#### 4. Physical Properties of Nanoporous Glasses

**4.1. Mechanical Properties.** Figure 4 shows that sintered aerogels, composites aerogels, and xerogels have quite similar toughness. However, sintered aerogels and composite aerogels are capable of resisting filling with an aqueous solution, whereas xerogels are generally not [16]. There are two explanations for these different behaviors: the xerogels network is locally damaged by the stresses that occur during drying. The assumption of damage to the structure is deduced from the reduced stiffness of xerogels compared to composite and sintered aerogels previously measured [35].

The xerogels flaw sizes are almost one order of magnitude higher than the composite and sintered aerogels flaws size (Figure 5). These flaws are created during drying, because of the large shrinkage. Flaws inside the structure act as stress concentrators and capillary stresses are locally amplified by this effect. The second explanation is linked to the smaller mean pore size of the xerogels structure (10 nm) compared to that of aerogels (10–100 nm) and composites aerogels (50–200 nm). During drying, xerogel is subjected to a compression force that tends to eliminate the larger pores [13]; drying shifts the pore size distribution toward the smaller pores and the capillary forces increase in smaller pores. Larger capillary forces and larger critical flaw sizes explain why the xerogels break during filling with aqueous solution.

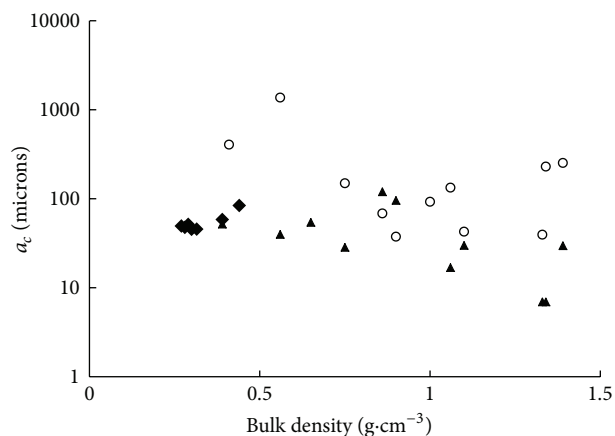


FIGURE 5: Critical flaw size versus density for xerogels (circles), sintered aerogels (triangles), and composites aerogels (diamonds).

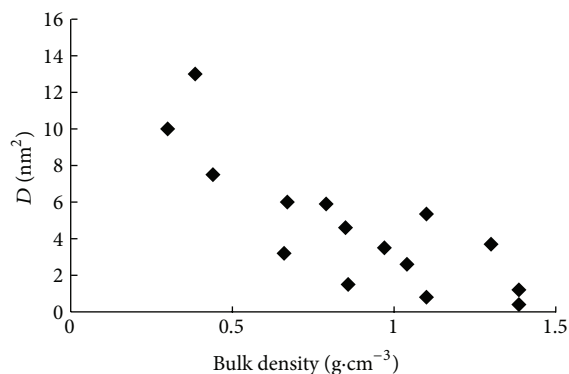


FIGURE 6: Permeability of the sintered aerogels versus the density.

The toughness of the set of sintered aerogels increased by 2 orders of magnitude (Figure 4), over the whole range of density. During the sintering process, densification is induced by viscous flow, which tends to reduce the volume of the whole sample, eliminating the smallest pores [36, 37]. Because of the mechanical improvement and the elimination of the micropores, the sintered aerogels are able to resist impregnation by a liquid [26].

In the composite approach, it is possible to adjust the pore volume by adding silica powder (such as aerosil) just before gelation [16, 33]. The addition of aerosil increases bulk density and hence the mechanical properties (Figure 4). Aerosil addition also affects the aggregation process, the pore structure [38], and pore size distribution [33]. It homogenizes the pore structure and increases the mean pore diameter to the mesoporosity range (50–200 nm) leading to lower capillary forces than in the xerogels.

In conclusion, drying, sintering, and the composite approach will improve the mechanical properties. However, xerogels samples usually cracked during filling with liquids certainly because of the presence of flaws, which weaken the gel network, and the small pores, which enhance capillary forces during filling. We can thus conclude that this set of samples is not an appropriate host for nuclear wastes.

**4.2. Permeability.** The second important porous feature of the host matrix is permeability. Permeability ( $D$ ) was measured by a method based on Archimedes' principle [16]. Previous study has shown that  $D$  decreases with sintering [15] and these new results confirm the previous data (Figure 6). The results are in agreement with the empirical Carman-Kozeny relation:  $D \propto (1 - \rho r) r_h^2$  [13, 15], where  $r_h$  is the mean pore size (hydraulic radius).

According to this relation, because of the decrease in the mean pore size and the increase in relative density,  $D$  decreases. So a compromise in density needs to be found for the use of sintered aerogels as host matrices. Bulk density has to be high enough to obtain a matrix with acceptable mechanical properties but not too high, to have significant permeability. The permeability of the composite aerogels set was measured using the same method (Figure 7) but, in contrast to the sintered aerogels, permeability of composite aerogel increased with an increase in density.

This counterintuitive result (with respect to the Carman-Kozeny relation) is due to the fact that while the addition of aerosol particles increases density it also increases mean pore size [33]. The net result is an increase in  $D$ .

The composite aerogels set combines improvement of the mechanical properties and an increase in permeability. This method is easy to use and produces host matrices with a large porous volume that is accessible and can be rapidly impregnated by water. Next, we tested the different porous networks as host matrices for long lived nuclides.

## 5. Loading of Gel Derived Porous Glass by Simulating Oxides

Although there are a number of fission product radionuclides with high activity ( $^{137}\text{Cs}$  and  $^{90}\text{Sr}$ ) and a long half-life ( $^{99}\text{Tc}$ , 200,000 years;  $^{129}\text{I}$ ,  $1.6 \cdot 10^7$  years) in nuclear wastes, actinides account for most of the radiotoxicity because, after several hundred years, the radiotoxicity is dominated by  $^{239}\text{Pu}$  (half-life = 24,100 years) and  $^{237}\text{Np}$  (half-life = 2,000,000 years). Thus, most of the long-term risk is directly related to the fate of these two actinides in the environment. Generally nuclear wastes are provided in salt form in aqueous solutions and, in the trapping approach [14–17, 31], the nanopore structure is used to allow migration of the liquid species (salt in solution) throughout the whole porous volume. Because of the fine pore structure, we would expect ourselves to be able to prepare a nanocomposite using a very simple process. Soaking of the porous network by surrogate solutions then needed to be tested. We chose Nd and Ce because of their different affinity with silica which produces different kinds of glass ceramics, simulating the possible behavior of the actinides in the presence of silica.

In a previous work [15], we showed that partial sintering is required to resist capillary forces, and heat treatment has two effects: it increases the mechanical strength of the aerogels and removes the smallest pores to reduce the effects of capillary phenomena. As explained above, the final density must avoid the formation of cracks but retain a sufficiently large porosity to allow the migration of the liquid through

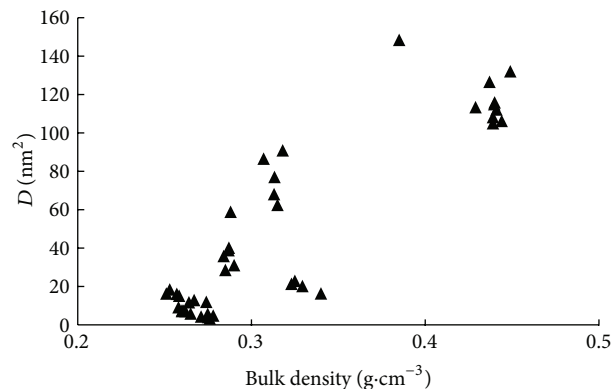


FIGURE 7: Permeability of the composite aerogels versus the density.

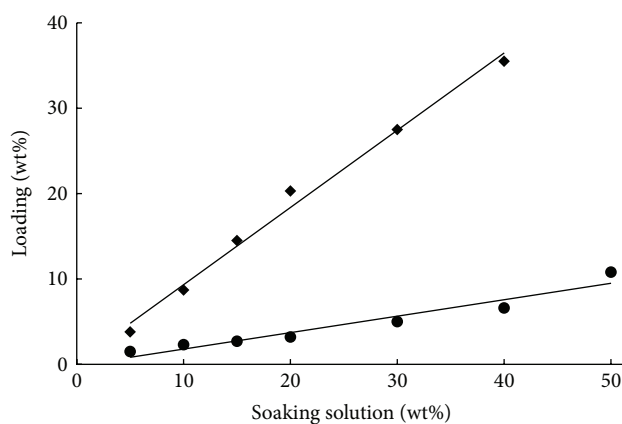


FIGURE 8: Loading with  $\text{Nd}_2\text{O}_3$  for sintered aerogels (circles) and composite aerogels (diamonds).

the whole volume of the sintered aerogels. The compromise was a bulk density close to  $1 \text{ g}\cdot\text{cm}^{-3}$  (almost 50% of the pore volume). Cerium and neodymium nitrates were dissolved in water. After soaking in an oven the sintered aerogels were dried and calcined at  $600^\circ\text{C}$  for two hours to decompose the neodymium nitrate. Further heating at  $1,100^\circ\text{C}$  fully sintered the gel structure [15, 26, 39].

The dense solid consisted of a silica matrix in which the surrogate oxide was trapped. The difference in weight before soaking and after sintering enables measurement of the “waste loading” in weight percent. Figure 8 shows that waste loading increased with the concentration of the simulate solution. Waste loading close to 10 weight percent can be achieved with this process [15] but the loading was twice lower than expected (calculated from the pore volume and the concentration of the solution). We concluded that, during the preliminary sintering step to achieve density close to  $1 \text{ g}\cdot\text{cm}^{-3}$ , part of the porosity closed and the soaking solution was unable to invade the whole porosity. Another approach proposed by Aravind et al. [17] is to incorporate surrogate ( $\text{Nd}_2\text{O}_3$ ) in the alcogel just before drying. The results of this study showed that high waste loading was obtained (30%).

Another way to improve the loading rate is to use a highly permeable porous structure that is more accessible

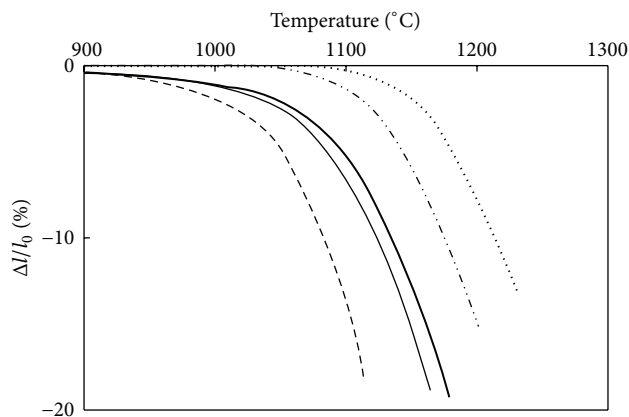


FIGURE 9: Sintering curves of composite aerogels (---), loaded with 5% (—), 10% (—), and 13%  $\text{CeO}_2$  (---); and 13%  $\text{Nd}_2\text{O}_3$  (···).

to the soaking solutions. This goal was achieved using the composite aerogel set. After soaking, drying, and calcination, the composite aerogels samples were fully sintered in the temperature range 1,100–1,250°C. Because composite aerogel has a higher pore volume than sintered aerogels, higher waste loading (35%) can be achieved with this process (Figure 8). However, high surrogate loading should cause thermomechanical stress. We discuss this problem in Section 7 of the paper.

## 6. Sintering Behavior

Dilatometer data (Figure 9) show that the sintering increases rapidly around 1000–1200°C, in the vicinity of the silica glass transition. Above 1000°C the sintering mechanism is a viscous flow process characteristic of amorphous materials [26, 39]. The sintering process is affected by the loading rate and Figure 9 shows the shrinkage curves of samples loaded with various  $\text{CeO}_2$  and  $\text{Nd}_2\text{O}_3$  concentrations.

The curves ( $\Delta l/l_0$ ) show that a high loading increases the temperature range in which shrinkage is large. This temperature is close to 1,050°C for the composite aerogel sample without loading, 1150°C for the sample containing 10% of  $\text{Nd}_2\text{O}_3$ , and 1,250°C for the composite aerogel loaded with 13% of  $\text{Nd}_2\text{O}_3$ .

Loading by surrogate solution prevents sintering, because the crystalline phases ( $\text{CeO}_2$  and  $\text{Nd}_2\text{O}_3$ ) are not involved in the viscous flow mechanism responsible for sintering of amorphous materials. The effect on the sintering temperature is more pronounced for Nd than for Ce because the samples loaded with Nd present three different crystalline phases: neodymium mono-silicate ( $\text{Nd}_2\text{SiO}_5$ ), di-silicate ( $\text{Nd}_2\text{Si}_2\text{O}_7$ ), and neodymium sesquioxide ( $\text{Nd}_2\text{O}_3$ ). Consequently the sintering step has to be adjusted to the composition of the loaded porous glass and can vary by 200°C.

## 7. Characterization of the Waste Glass Ceramics

We have shown that these porous matrices can be filled with the surrogate solution and fully sintered, demonstrating that

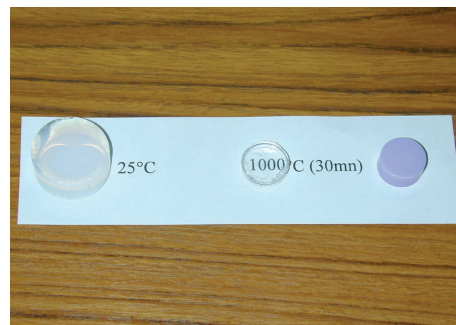


FIGURE 10: Aerogels sample (left), sintered aerogel (middle), and Nd loaded material (right).

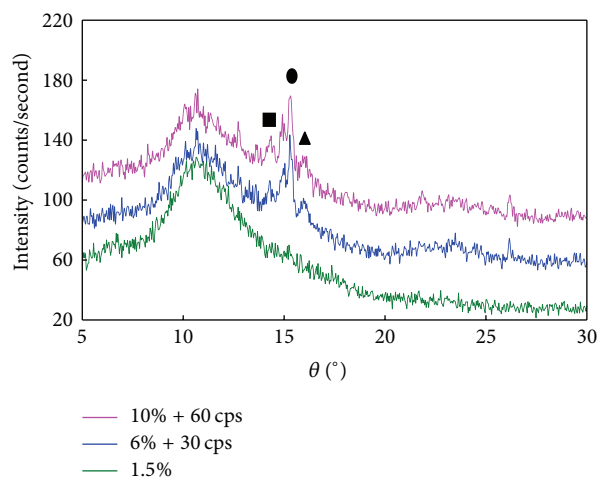


FIGURE 11: X-ray spectra of the ( $\text{SiO}_2\text{-Nd}_2\text{O}_3$ ) glass ceramic:  $\text{Nd}_2\text{SiO}_5$  (triangle),  $\text{Nd}_2\text{Si}_2\text{O}_7$  (square), and  $\text{Nd}_2\text{O}_3$  (circle).

rapid containment of actinides in silica is possible. After sintering, the nanocomposite solids consist of a silica matrix in which the actinide surrogate is trapped. The waste loadings we studied are in the range of 5–35% but loading higher than 50% can be achieved with these processes [17, 31].

**7.1. Structure.** Figure 10 shows an aerogel on the left. After complete sintering the aerogel is transformed in silica glass (middle) or in glass ceramic (right).

The final structure of the nanocomposite materials is that of glass ceramics. The X-ray spectra show that the sintered material loaded with Ce is a biphasic compound ( $\text{SiO}_2\text{-CeO}_2$ ) [40]. The sample loaded with Nd presents three different crystalline phases, neodymium mono-silicate ( $\text{Nd}_2\text{SiO}_5$ ) and di-silicate ( $\text{Nd}_2\text{Si}_2\text{O}_7$ ) but also neodymium sesquioxide ( $\text{Nd}_2\text{O}_3$ ) (Figures 11 and 12).

High Nd content favors the presence of neodymium mono-silicate ( $\text{Nd}_2\text{SiO}_5$ ). These structural differences are the result of the affinity of Ce and Nd for Si. In the case of Ce, the formation of a binary glass in a melting process is difficult; Ce generally forms  $\text{CeO}_2$  crystallites [41]. Moreover the crystalline phases of cerium silicates like  $\text{Ce}_2\text{Si}_2\text{O}_7$  are not stable at temperatures below 1,400°C [42, 43].

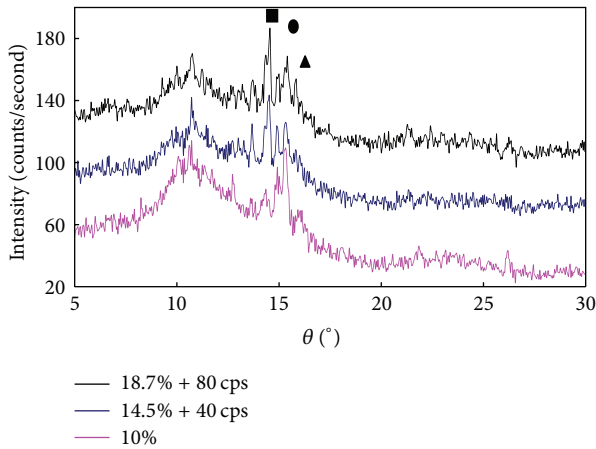


FIGURE 12: X-ray spectra of the  $(\text{SiO}_2\text{-Nd}_2\text{O}_3)$  glass ceramic:  $\text{Nd}_2\text{SiO}_5$  (triangle),  $\text{Nd}_2\text{Si}_2\text{O}_7$  (square), and  $\text{Nd}_2\text{O}_3$  (circle).

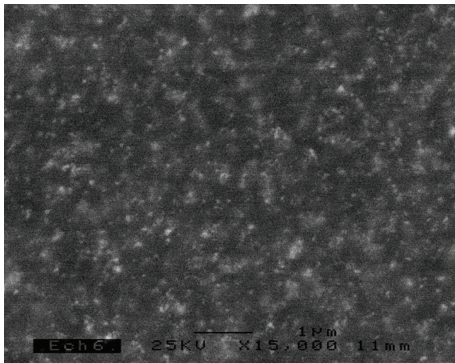


FIGURE 13: Back-scattered electron microscopy of the glass ceramic loaded with of  $\text{Nd}_2\text{O}_3$ .

In the case of Nd, glasses with a weight percent between 2 and 5 have been obtained [44, 45]. The phase diagram also shows that the different Nd silicates ( $\text{Nd}_2\text{SiO}_5$  and  $\text{Nd}_2\text{Si}_2\text{O}_7$ ) are stable at room temperature ( $\text{Nd}_2\text{O}_3$ ) [46, 47].

**7.2. Electron Microscopy.** Back-scattered electron microscopy (Figures 13 and 14) showed that the surrogate oxides were homogeneously distributed in the silica matrix.

The size of the surrogate domain ranged from 20 to 200 nm and the nanocomposites consisted of a silica matrix in which lanthanides oxides are trapped.

**7.3. Thermomechanical Properties.** The mechanical properties of the different glass ceramics are important in validating the process. The mechanical behavior of matrices containing nuclear wastes should be as high as possible because fracturing of the matrix will increase the corrosion rate (i.e., increase the contact surface between the solid and water). The rupture strength decreases progressively with the Nd loading and the weakening is important when Ce loading is higher than 10–15% [48]. Figure 15 compares the experimental data of the elastic modulus with calculated data given by the Reuss model [49].

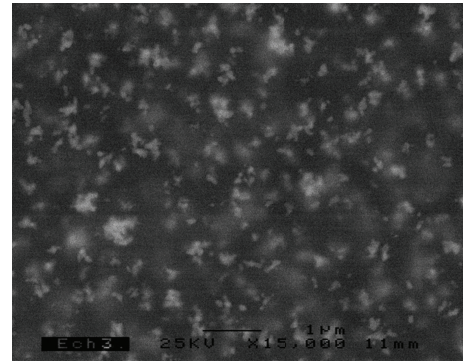


FIGURE 14: Back-scattered electron microscopy of the glass ceramic loaded with of  $\text{CeO}_2$ .

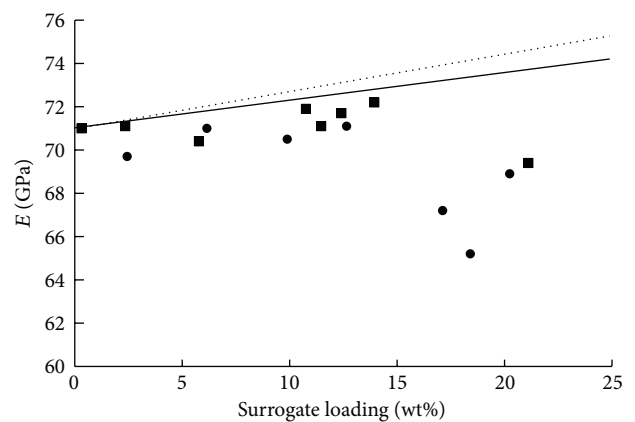


FIGURE 15: Evolution of the elastic modulus versus the loading rate for  $\text{Nd}_2\text{O}_3$  (square),  $\text{CeO}_2$  (circle) and Reuss models or  $\text{Nd}_2\text{O}_3$  (dotted line) and  $\text{CeO}_2$  (full line).

The model predicts the evolution of Young's modulus of composite materials as a function of the volume fraction and elastic properties of the different phases. The model assumes the stresses are transferred from a phase to another which requires both a close contact between matrix and particles and no microcracking. The model straight line was calculated with the elastic moduli of the silica glass (73 GPa [50]),  $\text{CeO}_2$  (184 GPa [51]), and  $\text{Nd}_2\text{O}_3$  (418 GPa [52]). Figure 15 shows that for loading higher than 15% the experimental data are clearly lower than the model prediction which confirms a weakening of the composite structure. This weakening of the material is the result of the large differences between the thermal expansion coefficients of the compounds present in the glass ceramics; the thermal expansion coefficient of vitreous silica ( $0.5 \cdot 10^{-6}/^\circ\text{C}$ ) is lower than that of  $\text{CeO}_2$  ( $11.5 \cdot 10^{-6}/^\circ\text{C}$ ) and  $\text{Nd}_2\text{O}_3$  ( $12 \cdot 10^{-6}/^\circ\text{C}$ ) crystallites [47]. After sintering and cooling, local stresses can occur at the boundary of the  $\text{CeO}_2$  and  $\text{Nd}_2\text{O}_3$  crystallites because of major differences in thermomechanical properties. The net result is the formation of microcracks that weaken the glass ceramics. Some authors tried to improve waste loading between 20 and 50% [17, 31]. However this approach could lead to microcracks in glass ceramics and the microflaws would encourage aqueous

TABLE 1: Normalized Ce, Nd, and Si mass loss ( $\text{g}\cdot\text{m}^{-2}$ ) versus corrosion time.

Days	SiO <sub>2</sub> Si mass loss ( $\text{g}\cdot\text{m}^{-2}$ )	SiO <sub>2</sub> -CeO <sub>2</sub> Si mass loss ( $\text{g}\cdot\text{m}^{-2}$ )	SiO <sub>2</sub> -CeO <sub>2</sub> Ce mass loss ( $\text{g}\cdot\text{m}^{-2}$ )	SiO <sub>2</sub> -Nd <sub>2</sub> O <sub>3</sub> Si mass loss ( $\text{g}\cdot\text{m}^{-2}$ )	SiO <sub>2</sub> -Nd <sub>2</sub> O <sub>3</sub> Nd mass loss ( $\text{g}\cdot\text{m}^{-2}$ )
7	0.124	0.250	n.m.	1.17	0.01
14	0.252	0.436	n.m.	2.89	0.025
21	0.34	0.656	0.108	5.91	0.15
28	0.442	1.012	0.162	9.33	0.31

corrosion and hence lead to the diffusion of actinides in the environment. Once again a compromise needs to be found for “efficient” waste loading in the range 10–15%. This loading rate is acceptable and corresponds to the nuclear waste content in existing borosilicate nuclear waste glass [10, 52].

**7.4. Chemical Durability.** Chemical durability ensures resistance to aqueous corrosion. In general, glass corrosion in aqueous solutions is governed by diffusion-controlled ion exchange and dissolution of the glass network itself [52–55]. Corrosion could be favored by the presence of thermomechanical stresses [55] and by the solubility of the silica in regions with different curvature [56]. Moreover saturation of the solution can affect the processes. We have seen that the Nd glass ceramic have a more complicated structure than Ce glass ceramic. As a result, different chemical durability behaviors are to be expected.

As explained in the introduction, vitreous silica has high chemical durability. This is thus necessary to compare the mechanisms of alteration of the Nd and Ce glass ceramics with those of silica and the usual borosilicate glass. The chemical durability of the glass ceramics was measured with a conventional Soxhlet device [15], and we measured the Ce, Nd, and Si mass losses [40] (Table 1).

The normalized silica loss characterizes the destruction of the glass network by the glass former dissolution. The dynamic corrosion rate ( $V_0$ ) of pure silica is equal to  $0.015 \text{ g}\cdot\text{m}^{-2}$  per day, 100 times lower than the corrosion rate of the usual nuclear waste glass for which  $V_0$  is equal to  $2 \text{ g}\cdot\text{m}^{-2}$  per day [53, 54].  $V_0$  for the glass ceramics loaded with the Ce was  $0.035 \text{ g}\cdot\text{m}^{-2}$  per day and  $0.25 \text{ g}\cdot\text{m}^{-2}$  per day with Nd: evidence of the better chemical durability of glass ceramics compared to that of nuclear waste glass. The corrosion rate of the Nd glass ceramic is 8 times higher than SiO<sub>2</sub>. It has been shown that the sol-gel-glass process allows the synthesis of binary neodymium silica glasses with neodymium content as high as 5% [44, 45], less durable than SiO<sub>2</sub>.

Long-term aqueous corrosion results [48] also suggest that in these new matrices a limit of solubility is attained that prevents alteration of the material, which is not the case of standard nuclear waste glass in which the process of corrosion is never stopped in water [8, 57, 58]. In the literature, the corrosion of the Nd glass ceramics has also been studied through soxhlet experiments [9, 23]. These authors also found a poor corrosion effect but unfortunately the data are not comparable because of the lower temperature they used for the process (60–70°C) and a shorter experiment (only lasting

two days) which does not allow the chemical durability to be characterized in saturation conditions.

## 8. Conclusion

Borosilicate glass is a solid in which a wide range of nuclear waste can be dissolved and successful industrial-scale technologies have been developed. However research is now investigating new containment matrices with high chemical durability, because it is important to limit the possible release of radionuclides if the matrix is destroyed by aqueous erosion. This paper describes different matrices aimed at rendering hazardous materials less dangerous including fixing the hazardous material in the nanopores of porous glasses and vitrifying the nanoporous material containing the less hazardous material.

The composite silica approach is likely the best compromise to confine actinides. A high pore volume is available for impregnation and network permeability is increased and rapid containment of surrogate actinide oxides in silica has been demonstrated. Surrogate elements are embedded in the silica matrix. The main advantages of the process are the high chemical durability of the silica matrix and the good mechanical resistance.

In addition to the problem of the synthesis of new porous matrices, the influence of the reactivity of the surface and of the pore structure on the physical and chemical properties of the invading species is the subject of much ongoing research. We have presented two examples in which the reactivity of the chemical species in the matrix is extremely important for the physical properties of the final two-phase materials. It should also be underlined that this process enables the synthesis of nanocomposite materials, which cannot be achieved by melting. Sintering preserves the initial heterogeneous structure.

## Competing Interests

The authors declare that they have no competing interests.

## References

- [1] F. P. Glasser, “The role of ceramics, cement and glass in the immobilization of radioactive wastes,” *British Ceramic Transactions*, vol. 84, pp. 1–8, 1985.
- [2] I. W. Donald, B. L. Metcalfe, and R. N. J. Taylor, “The immobilization of high level radioactive wastes using ceramics and glasses,” *Journal of Materials Science*, vol. 32, no. 22, pp. 5851–5887, 1997.

- [3] V. M. Oversby and A. E. Ringwood, "Leaching studies on synroc AT 95°C and 200°C," *Radioactive Waste Management*, vol. 2, no. 3, pp. 223–237, 1982.
- [4] G. R. Lumpkin and R. C. Ewing, "Geochemical alteration of pyrochlore group minerals: pyrochlore subgroup," *American Mineralogist*, vol. 80, no. 7-8, pp. 732–743, 1995.
- [5] P. J. McGlin, K. P. Hart, E. H. Loi, and E. R. Vance, "Ph dependence of the aqueous dissolution rates of perovskite and zirconolite at 90°C," *Materials Research Society Symposium Proceedings*, vol. 353, pp. 847–854, 1995.
- [6] P. J. Hayward, "The use of glass ceramics for immobilising high level wastes from nuclear fuel recycling," *Glass Technology*, vol. 29, no. 4, pp. 122–136, 1988.
- [7] P. Loiseau, D. Caurant, N. Baffier, L. Mazerolles, and C. Fillet, "Development of zirconolite-based glass-ceramics for the conditioning of actinides," in *Scientific Basis for Nuclear Waste Management XXIV*, K. P. Hart and G. P. Lumpkin, Eds., vol. 663 of *MRS Proceedings*, pp. 179–189, Materials Research Society, Warrendale, Pa, USA, 2001.
- [8] P. Frugier, C. Martin, I. Ribet, T. Advocat, and S. Gin, "The effect of composition on the leaching of three nuclear waste glasses: R7T7, AVM and VRZ," *Journal of Nuclear Materials*, vol. 346, no. 2-3, pp. 194–207, 2005.
- [9] R. C. Ewing, "Nuclear waste form glasses: the evaluation of very long term behaviour," *Materials Technology: Advanced Performance Materials*, vol. 16, pp. 30–36, 2001.
- [10] N. Jacquet-Francillon, R. Bonniaud, and C. Sombret, "Glass as a material for the final disposal of fission products," *Radiochimica Acta*, vol. 25, no. 3-4, pp. 231–240, 1978.
- [11] V. M. Oversby and A. E. Ringwood, "Leaching studies on synroc at 95°C and 200°C," *Radioactive Waste Management*, vol. 2, no. 3, pp. 223–237, 1982.
- [12] I. W. Donald, B. L. Metcalfe, and R. N. J. Taylor, "The immobilization of high level radioactive wastes using ceramics and glasses," *Journal of Materials Science*, vol. 32, no. 22, pp. 5851–5887, 1997.
- [13] J. F. Brinker and G. W. Scherer, *Sol-Gel Science*, Academic Press, New York, NY, USA, 1990.
- [14] J. H. Simmons, P. B. Macedo, A. Barkatt, and T. A. Litovitz, "Fixation of radioactive waste in high silica glasses," *Nature*, vol. 278, no. 5706, pp. 729–731, 1979.
- [15] T. Woignier, J. Reynes, J. Phalippou, J. L. Dussossoy, and N. Jacquet-Francillon, "Sintered silica aerogel: a host matrix for long life nuclear wastes," *Journal of Non-Crystalline Solids*, vol. 225, pp. 353–357, 1998.
- [16] J. Reynes, T. Woignier, and J. Phalippou, "Permeability measurement in composite aerogels: application to nuclear waste storage," *Journal of Non-Crystalline Solids*, vol. 285, no. 1–3, pp. 323–327, 2001.
- [17] P. R. Aravind, L. Sithara, P. Mukundan, P. Krishna Pillai, and K. G. K. Warriar, "Silica alcogels for possible nuclear waste confinement—a simulated study," *Materials Letters*, vol. 61, no. 11-12, pp. 2398–2401, 2007.
- [18] A. Deptula, M. Milkowska, W. Lada et al., "Sol-gel processing of silica nuclear wastes glasses," *New Journal of Glass and Ceramics*, vol. 1, no. 3, pp. 105–111, 2011.
- [19] G. W. Scherer, "Sintering of low density glasses: experimental study," *Journal of the American Ceramic Society*, vol. 60, no. 5-6, pp. 239–243, 1977.
- [20] P. F. James, "The gel to glass transition: chemical and microstructural evolution," *Journal of Non-Crystalline Solids*, vol. 100, no. 1–3, pp. 93–114, 1988.
- [21] J. G. Zwissler and M. A. Adams, *Fracture Mechanics of Ceramics*, Edited by R. C. Bradt, A. G. Evans, D. P. H. Hasselman and F. F. Lange, Plenum Press, New York, NY, USA, 1983.
- [22] F. Pernot, P. Baldet, F. Bonnel, J. Zarzycki, and P. Rabischong, "Development of phosphate glass-ceramics for bone implants," *Ceramics International*, vol. 9, no. 4, pp. 127–131, 1983.
- [23] P. Debye and R. L. Cleland, "Flow of liquid hydrocarbons in porous vycor," *Journal of Applied Physics*, vol. 30, no. 6, pp. 843–849, 1959.
- [24] K. Kuhne and W. Skatulla, "Physikalische und chemische Untersuchungen an Gläsern," *Silikattechn*, vol. 10, pp. 105–119, 1959.
- [25] T. Elmer H, "Porous and reconstructed glasses," in *Engineered Materials Handbook*, vol. 4, pp. 427–432, ASM International, Materials Park, Ohio, USA, 1992.
- [26] T. Woignier, J. Phalippou, and M. Prassas, "Glasses from aerogels—part 2 the aerogel-glass transformation," *Journal of Materials Science*, vol. 25, no. 7, pp. 3118–3126, 1990.
- [27] E. D. Zanotto, "The formation of unusual glasses by sol-gel processing," *Journal of Non-Crystalline Solids*, vol. 147-148, pp. 820–823, 1992.
- [28] T. Woignier, J. Phalippou, H. Hdach, G. Larnac, F. Pernot, and G. W. Scherer, "Evolution of mechanical properties during the alcogel-aerogel-glass process," *Journal of Non-Crystalline Solids*, vol. 147-148, pp. 672–680, 1992.
- [29] J. Phalippou, T. Woignier, and M. Prassas, "Glasses from aerogels-part 1: the synthesis of monolithic silica aerogels," *Journal of Materials Science*, vol. 25, no. 7, pp. 3111–3117, 1990.
- [30] J. L. Gurav, I.-K. Jung, H.-H. Park, E. S. Kang, and D. Y. Nadargi, "Silica aerogel: synthesis and applications," *Journal of Nanomaterials*, vol. 2010, Article ID 409310, 11 pages, 2010.
- [31] P. R. Aravind, P. Shajesh, P. Mukundan, P. Krishna Pillai, and K. G. K. Warriar, "Non-supercritically dried silica-silica composite aerogel and its possible application for confining simulated nuclear wastes," *Journal of Sol-Gel Science and Technology*, vol. 46, no. 2, pp. 146–151, 2008.
- [32] R. Sempere, D. Bourret, T. Woignier, J. Phalippou, and R. Jullien, "Scaling theory and numerical applications of aerogel sintering," *Physical Review Letters*, vol. 71, no. 20, pp. 3307–3312, 1993.
- [33] M. Toki, S. Miyashita, T. Takeuchi, S. Kanbe, and A. Kochi, "A large-size silica glass produced by a new sol-gel process," *Journal of Non-Crystalline Solids*, vol. 100, no. 1–3, pp. 479–482, 1988.
- [34] S. Sakka and T. Adachi, "Stability of sol-gel derived porous silica monolith to solvents," *Journal of Materials Science*, vol. 25, no. 7, pp. 3408–3414, 1990.
- [35] G. W. Scherer, D. M. Smith, X. Qiu, and J. M. Anderson, "Compression of aerogels," *Journal of Non-Crystalline Solids*, vol. 186, pp. 316–320, 1995.
- [36] G. W. Scherer, "Sintering of low-density glasses: I. Theory," *Journal of the American Ceramic Society*, vol. 60, no. 5-6, pp. 236–239, 1977.
- [37] T. Woignier, J. Phalippou, J. Quinson F, M. Pauthe, M. Repellin-Lacroix, and G. W. Scherer, "The sintering of silica aerogels studied by thermoporometry," *Journal of Sol-Gel Science and Technology*, vol. 2, no. 1, pp. 277–281, 1994.
- [38] C. Marlière, T. Woignier, P. Dieudonné, J. Primera, M. Lamy, and J. Phalippou, "Two fractal structures in aerogel," *Journal of Non-Crystalline Solids*, vol. 285, no. 1–3, pp. 175–180, 2001.
- [39] W. G. Scherer, "Sintering of low density glasses: II experimental study," *Journal of the American Ceramic Society*, vol. 60, pp. 239–243, 1977.

- [40] T. Woignier, J. Reynes, J. Phalippou, and J. L. Dussossoy, "Nuclear waste storage in gel-derived materials," *Journal of Sol-Gel Science and Technology*, vol. 19, no. 1-3, pp. 833-837, 2000.
- [41] R. G. Haire, Z. Assefa, and N. Stump, "Fundamental science of elements in selected immobilization glasses: significance for TRU disposal schemes," *Materials Research Society Symposium Proceeding V*, vol. 506, pp. 153-160, 1998.
- [42] J. Felsche and W. Hirsiger, "The polymorphs of the rare-earth pyrosilicates  $R.E._2Si_2O_7$ , [R.E.: La, Ce, Pr, Nd, Sm]," *Journal of the Less-Common Metals*, vol. 18, no. 2, pp. 131-137, 1969.
- [43] H. A. M. Van Hal and H. T. Hintzen, "Compound formation in the  $Ce_2O_3$ - $SiO_2$  system," *Journal of Alloys and Compounds*, vol. 179, no. 1-2, pp. 77-85, 1992.
- [44] I. M. Thomas, S. A. Payne, and G. D. Wilke, "Optical properties and laser demonstrations of Nd-doped sol-gel silica glasses," *Journal of Non-Crystalline Solids*, vol. 151, no. 3, pp. 183-194, 1992.
- [45] E. J. A. Pope and J. D. Mackenzie, "Sol-gel processing of neodymia-silica glass," *Journal of the American Ceramic Society*, vol. 76, no. 5, pp. 1325-1328, 1993.
- [46] R. O. Miller and D. E. Rase, "Phase equilibrium in the system  $Nd_2O_3$ - $SiO_2$ ," *Journal of the American Ceramic Society*, vol. 47, no. 12, pp. 65-654, 1964.
- [47] N. A. Toropov, "Determination of phase diagrams using diffusion techniques," in *Proceedings of the Transactions of the 7th International Ceramic Congress*, pp. 435-442, London, UK, 1960.
- [48] T. Woignier, J. Reynes, and J. Phalippou, "Sintering of silica aerogels for glass synthesis: application to nuclear waste containment," in *Aerogels Handbook*, M. A. Aegerter, N. Leventis, and M. M. Koebel, Eds., *Advances in Sol-Gel Derived Materials and Technologies*, chapter 29, pp. 665-680, Springer, New York, NY, USA, 2011.
- [49] I. Warshaw and R. Roy, "Thermal-expansion measurements from nonindexed high-temperature X-ray powder patterns," *Journal of the American Ceramic Society*, vol. 44, no. 8, pp. 421-422, 1961.
- [50] N. P. Bansal and D. R. Doremus, *Handbook of Glass Properties*, Academic Press, New York, NY, USA, 1986.
- [51] E. Keler and A. B. Andreeva, "Stabilization of zirconia with combined additives and a study of a solid solution stability," *Ogneupory*, vol. 5, pp. 224-230, 1963.
- [52] L. Werme, I. K. Björner, G. Bart et al., "Chemical corrosion of highly radioactive borosilicate nuclear waste glass under simulated repository conditions," *Journal of Materials Research*, vol. 5, no. 5, pp. 1130-1146, 1990.
- [53] W. Lutze, G. Malow, R. C. Ewing, M. J. Jercinovic, and K. Keil, "Alteration of basalt glasses: implications for modelling the long-term stability of nuclear waste glasses," *Nature*, vol. 314, no. 6008, pp. 252-255, 1985.
- [54] J. L. Nogue, *Les mécanismes de corrosion des verres de confinement des produits de fission [Ph.D. thesis]*, Université de Montpellier, Montpellier, France, 1984.
- [55] B. C. Bunker, "Molecular mechanisms for corrosion of silica and silicate glasses," *Journal of Non-Crystalline Solids*, vol. 179, pp. 300-308, 1994.
- [56] R. K. Iler, *The Chemistry of Silica*, John Wiley & Sons, New York, NY, USA, 1979.
- [57] B. Grambow, "A general rate equation for nuclear waste glass corrosion," *Materials Research Society Symposium Proceedings*, vol. 44, pp. 15-21, 1985.
- [58] J.-C. Petit, J.-C. Dran, G. D. Mea, and A. Paccagnella, "Dissolution mechanisms of silicate minerals yielded by intercomparison with glasses and radiation damage studies," *Chemical Geology*, vol. 78, no. 3-4, pp. 219-227, 1989.

## Research Article

# Surface Functionality Features of Porous Silicon Prepared and Treated in Different Conditions

Yu. M. Spivak,<sup>1</sup> S. V. Mjakin,<sup>2</sup> V. A. Moshnikov,<sup>1</sup> M. F. Panov,<sup>1</sup>  
A. O. Belorus,<sup>1</sup> and A. A. Bobkov<sup>1</sup>

<sup>1</sup>Department of Micro- and Nanoelectronics, Saint Petersburg Electrotechnical University "LETI", 5 Professor Popova Street, Saint Petersburg 197376, Russia

<sup>2</sup>Department of Theory of Materials Science, Saint Petersburg State Technological Institute (Technical University), 26 Moskovsky Prospect, Saint Petersburg 190013, Russia

Correspondence should be addressed to Yu. M. Spivak; [ymspivak@etu.ru](mailto:ymspivak@etu.ru)

Received 10 December 2015; Revised 10 March 2016; Accepted 13 March 2016

Academic Editor: Mahaveer Kurkuri

Copyright © 2016 Yu. M. Spivak et al. This is an open access article distributed under the Creative Commons Attribution License, which permits unrestricted use, distribution, and reproduction in any medium, provided the original work is properly cited.

Hydrophilic layers of porous silicon are prepared by single- or two-step anodization and characterized by evaluating their surface hydrophilicity and contents of functional groups using IR spectroscopy and adsorption of acid-base indicators with different  $pK_a$  values. The surface functional composition of the synthesized samples is shown to be adjustable depending on the anodization current density. The surface of samples obtained at anodization current density  $30 \text{ mA/cm}^2$  is predominantly occupied with  $pK_a$  2.5 corresponding to  $\equiv\text{Si-OH}$  groups. The increase of current density to  $80 \text{ mA/cm}^2$  results in the increase of surface functional nonuniformity with the formation of versatile centers, primarily Lewis acidic sites corresponding to Si atoms, as indicated by selective indicator adsorption in agreement with the disappearance of Si-H bonds in IR spectra and overall surface disordering according to SEM and AFM data.

## 1. Introduction

Porous silicon (por-Si) is a promising material for sensors, biosensors, and specific medical purposes [1–4]. Biomedical applications of por-Si involve the use as a carrier for target delivery of single or combined drugs [5–9], photosensitive agents in photodynamic therapy and in tissue engineering [10], various biodetectors, and biomedical imaging [11] including tumor visualization, as well as eye diseases. Modified por-Si layers can be used in biosensors [1, 2, 4, 12–17] for various applications including the determination of glucose, DNA, antibodies, bacteria, and viruses [12–14]. This application area involves different types of sensors, including electric, electrochemical, optical, and labeling devices [15–17]. Biosensor application of por-Si also includes the use in passive platforms for the deposition of biological cultures and active elements interaction with the biological environment [15, 18, 19]. A highly developed porous structure of por-Si facilitates the development of highly efficient

parallel biochips for the analysis of several cultures in one platform. Furthermore, por-Si is a promising material for nanocontainers in targeted drug delivery [3–9, 20]. The main advantages of por-Si nanocontainers include high sorption or carrier capacity due to a large surface area, pore volume and concentration, high stability, biocompatibility, versatility of modifications and characteristics, inexpensive synthesis processes, and easy exploration in target applications [4, 9, 20–23]. Moreover, por-Si nanocontainers are efficient for *in vivo* applications since they dissolve in an organism with the rate adjustable by varying the porosity and surface chemistry [4, 24–26] and yield only a nontoxic orthosilicic acid that affords a controllable drug release from such nanocontainers.

In this way, por-Si nanoparticles can be used for effective delivery of antiviral drugs to infected cells. In [27] a significant increase of Streptocidum (saliphenylhalamide, SaliPhe) solubility was achieved by encapsulating this antibiotic into thermally hydrocarbonized por-Si (THCPSi) nanoparticles subsequently releasing this drug to inhibit influenza infection

*in vitro* and reduce the number of progeny viruses in influenza-infected cells. In addition to increased solubility, the considered por-Si based nanosystems were shown to provide improved drug delivery properties, including high stability *in vitro* and low cytotoxicity [27]. The preparation of biodegradable por-Si nanoparticles functionalized with antibodies that target cancer cells and containing a hydrophobic anticancer drug camptothecin described in [7] afforded a successful targeting and selective destruction of cancer cells.

A highly promising application area relates to the development of systems for a simultaneous delivery of different therapeutic agents, for example, low molecular weight drugs, and with relatively large peptides [6], such as hydrophobic indomethacin in combination with hydrophilic human peptide YY3-36 (PYY3-36). The authors argue that the startup sequence of the two drugs in por-Si nanoparticles affects the release rate of each drug. PYY3-36 was found to provide a significant improvement of por-Si nanoparticles cytological compatibility and possess a biological activity and ability to penetrate the intestinal cells after the release from nanoparticulate por-Si carrier.

Depending on the type of carried drugs and their chemical composition, particularly specific functional groups (hydroxyl groups, amino groups, etc.) in their molecules, the nanocontainer surface should meet the corresponding requirements such as hydrophilic or hydrophobic nature, presence of certain adsorption centers (functional groups), and charge. By adjusting the technological conditions, it is possible to adjust geometric characteristics of the porous texture and the composition of the porous silicon surface. It is significant for delivering various therapeutic agents, from small drugs to large molecular peptides/protein therapeutics [4]. Particularly, the hydrophilic-hydrophobic, acid-base, and donor-acceptor properties determined by the presence of specific centers and functional groups on the surface significantly affect such properties as wettability, permeability of pores to certain substances (that in turn determines the selection of solvents or dispersion media), and interaction with physiological liquids and drugs.

Furthermore, the phase composition and morphology of porous silicon surface are also highly important. These properties are known to markedly vary depending on the source material and electrochemical processing conditions parameters [9, 20, 21, 28–30]. XANES and IR spectroscopy investigations [29] revealed that the ratio between oxide and silicon phases in the surface layer is higher for por-Si obtained at low-resistance substrates of n-Si compared with p-por-Si samples due to the concentration and type of substrate doping impurities. Furthermore, XANES and XPS studies indicated a considerable variation of por-Si phase composition, particularly the content of  $\alpha$ -Si,  $\alpha$ -Si:H, and nanocrystalline silicon (nc-Si) phases in depth of the porous layer [21, 30]. The surface layer is enriched with a mixture of silicon dioxide, nonstoichiometric silicon oxide (up to 48%), and hydrogenated amorphous silicon while the percentage of nc-Si grows with depth (e.g., to 62% at the depth of 60 nm).

In addition to the specific composition of functional groups, their general acid-base properties as well as the charge state of por-Si surface are also very important factors

that should be considered when choosing the conditions for obtaining porous silicon; they significantly affect the interaction mechanism between por-Si carrier surface and grafted therapeutic agents or other substances.

An effective approach to the study of adsorption centers and functional groups on the surface of solids using a selective adsorption of acid-base indicators with different  $pK_a$  values was suggested in [31, 32]. This method is extremely sensitive and allows distinguishing the functional groups of the same chemical composition differing only in the electron density distribution and therefore in their acid-base and donor-acceptor properties characterized by their  $pK_a$  values. Earlier the considered technique was successfully applied in the study of various oxide materials [31, 32]; however it was never used in respect of porous silicon.

This research work is aimed at the study of possibilities to control the surface composition of por-Si useful for target drug delivery by the variation of its synthesis parameters via electrochemical anodization in an Unno-Imai cell.

## 2. Experimental

**2.1. Preparation of Porous Silicon Layers.** Por-Si layers were prepared by electrochemical anodization of monocrystalline silicon in an Unno-Imai [33]. The application of Unno-Imai method is determined by a more uniform electric field distribution over the anodized sample in the case of a double-chamber cell compared with a single-chamber one due to a direct electric contact between the silicon plate cathode side and electrolyte in the second consecutively connected cell (chamber). This approach provides an increased uniformity of the porous layer characteristics over the plate surface and simplifies the plate preparation for anodization because a preliminary formation of a highly doped or metal layer on the nonprocessed side of the plate is not required in this case.

KEF-5 silicon (111, n-type conductivity, doped with phosphorus, electric resistance 5 Ohm-cm) was used as a source substrate material. All the samples were subjected to the same pretreatment procedures before and posttreatment procedures after the electrochemical anodization.

The electrochemical anodization was carried out using an aqueous electrolyte comprising HF aqueous solution with addition of isopropyl alcohol [4, 34]. Porous silicon was prepared via a single- and two-stage anodization with the variation of current density  $J$  and anodization time  $t$ . The process conditions are summarized in Table 1.

**2.2. Characterization Methods.** The morphology and texture of the obtained por-Si samples were characterized by SEM (Phenom) and AFM (Ntegra Terma, NT-MDT) methods.

The composition of functional groups on por-Si surface was studied by FTIR reflectance spectroscopy using a Nicolet-6700 installation in a mode specifically useful for the characterization of semiconductors [4, 21, 29, 35, 36] involving both integrated (over a large surface) and local (in the areas up to 10  $\mu\text{m}$ ) ones. This characterization was performed for samples obtained under different conditions in single- and two-phase synthesis as well as for samples prepared under the

TABLE 1: Conditions of por-Si layers preparation.

Series of samples	Current density $J$ , mA/cm <sup>2</sup>	$t$ , min	Number of prepared samples	Notes
I	30	15	8	Single-stage anodization
II	80	15	8	Single-stage anodization
III	Stage 1: 80	Stage 1: 30	2	Two-stage anodization
IV	Stage 2: 30	Stage 2: 60	2	Two-stage anodization, storage in ambient conditions for 2 years

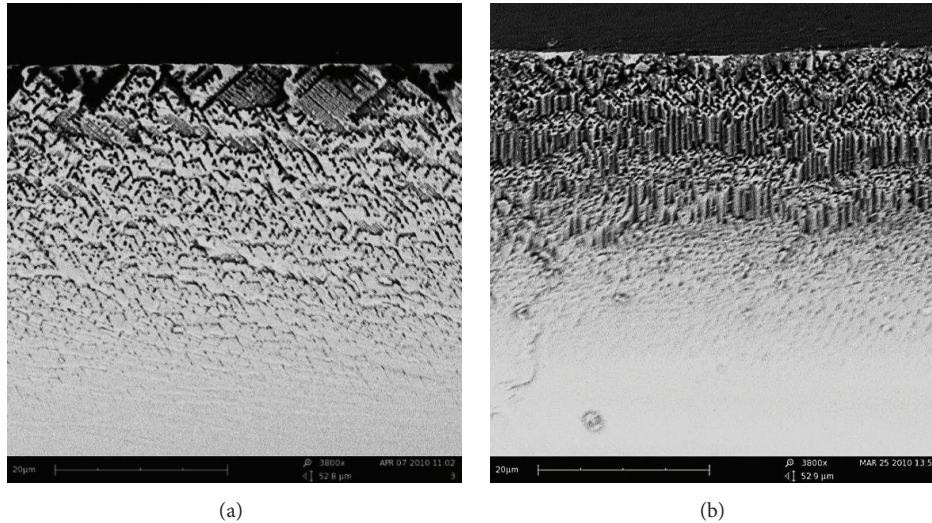


FIGURE 1: Texture of obtained por-Si illustrated by SEM data of splits for samples synthesized at (a)  $j = 30 \text{ mA/cm}^2$ ,  $t = 60 \text{ min}$  and (b)  $j = 80 \text{ mA/cm}^2$ ,  $t = 30 \text{ min}$ .

same conditions straight upon the synthesis and after 2-year storage in ambient conditions.

Furthermore, in order to precisely analyze the surface functionality of the samples, they were also studied using a selective adsorption of acid-base indicators with different  $\text{pK}_a$  values. This method described in detail in [31, 32] affords a highly sensitive determination and distinguishing surface centers, including functional groups of the same chemical composition differing only in the electron density distribution and, consequently, in their acid-base and donor-acceptor properties. In this paper we determined the content of the acid centers on the surface of the synthesized samples: the typical silicon surface Lewis acid centers (Si atoms) and Bronsted acid centers (groups  $\equiv\text{Si}-\text{OH}$ ), close to the neutral centers (group  $=\text{Si}(\text{OH})_2$ ) and the main centers (the group  $-\text{Si}(\text{OH})_3$ ).

### 3. Results and Discussion

**3.1. Effect of Synthesis Parameters on por-Si Morphology and Texture.** SEM data for splits of por-Si samples prepared under anodization conditions corresponding to each stage of series III separately and after the complete two-stage anodization as well as for a sample synthesized in a single stage within the time equal to the overall anodization time for

series III at current density  $80 \text{ mA/cm}^2$  are shown in Figures 1 and 2.

The textural characterization of these samples suggests that in the considered conditions a system of channels is formed involving meso- and macropores predominantly spread along a (100) crystallographic direction. The samples prepared at the current density  $80 \text{ mA/cm}^2$  are featured with the presence of pores directed rectangularly to the surface plane that probably accounted for the applied electric field geometry and competing processes at anodization.

As shown in Figure 2, two-stage anodization with the variation of current density in the considered conditions provides the formation of two por-Si layers with a well-defined boundary. The textural features of por-Si layers prepared in a two-stage mode (Figure 2(a)) resemble that for the samples synthesized in a single-phase mode in the similar conditions (Figures 1(a) and 1(b)). The formation of more loose and highly developed surface for samples prepared in two stages is probably determined by the second-stage features involving not only the formation of por-Si layer with modified texture during the anodization front movement inside the substrate but also a certain additional etching of the top por-Si layer.

AFM data (Figure 3) indicate that the increase in the anodization current density leads to the increase of the

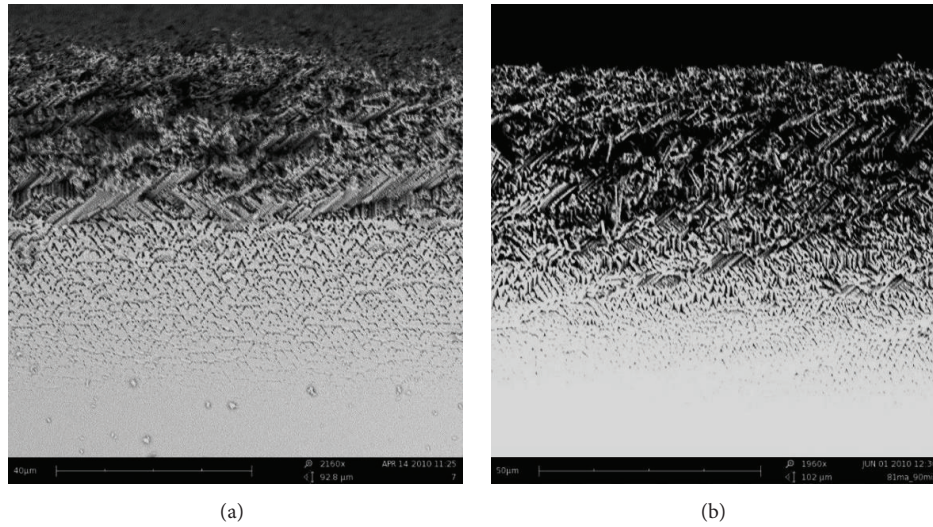


FIGURE 2: SEM data for splits of por-Si samples prepared (a) in two-stage (stage 1:  $j = 80 \text{ mA/cm}^2$ ,  $t = 30 \text{ min}$ ; stage 2:  $j = 30 \text{ mA/cm}^2$ ,  $t = 60 \text{ min}$ ) and (b) single-stage anodization ( $j = 80 \text{ mA/cm}^2$ ,  $t = 90 \text{ min}$ ).

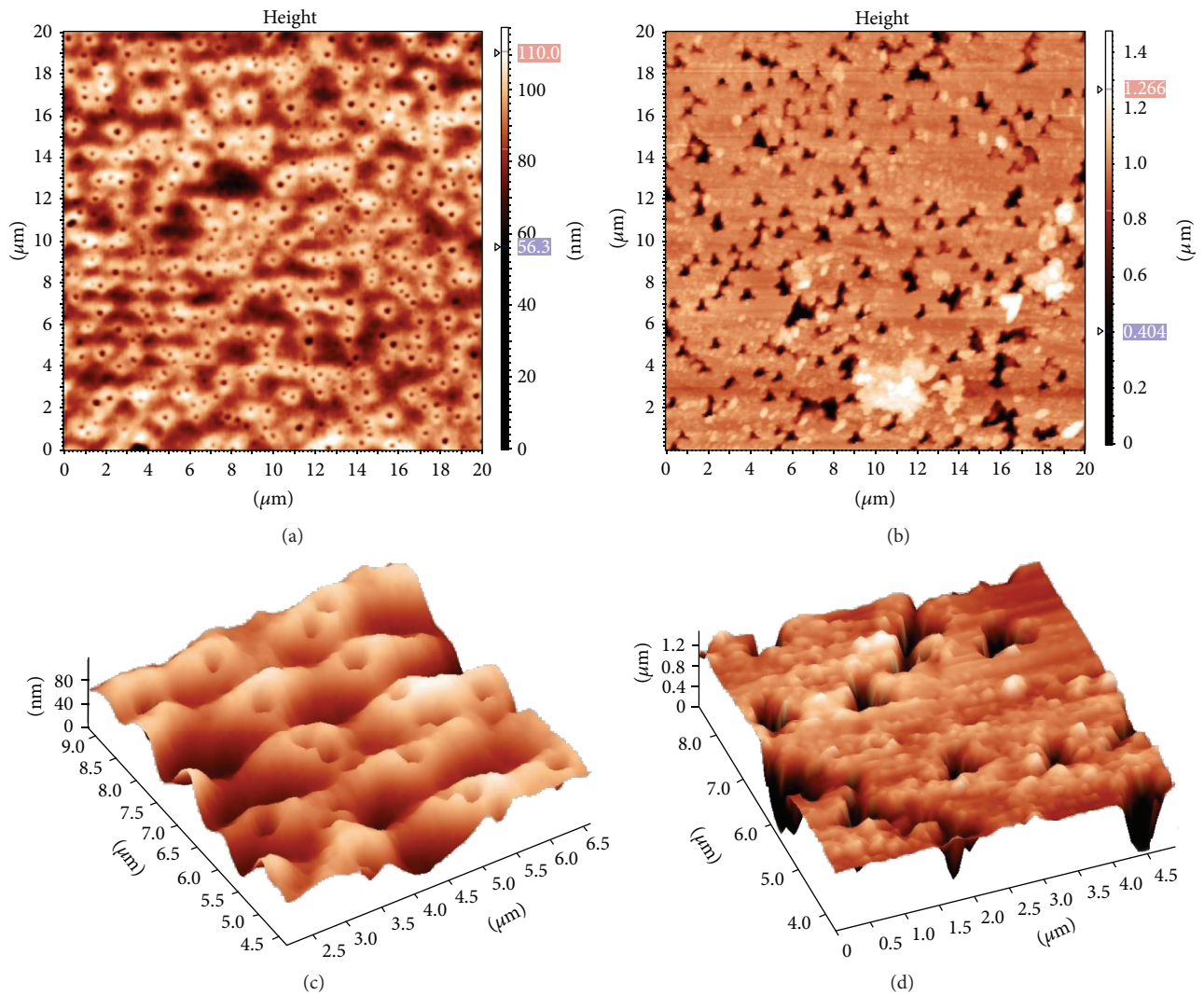


FIGURE 3: Morphology of por-Si layers according to AFM data: (a), (c) series I ( $j = 30 \text{ mA/cm}^2$ ); (b), (d) series II ( $j = 80 \text{ mA/cm}^2$ ).

resulting pore size and a significant surface flattening between the pores.

**3.2. IR Spectroscopy Data on the Composition of Functional Groups on the Surface of Porous Silicon.** IR reflectance spectroscopy analyses were carried out for por-Si samples prepared via a single-stage anodization in two different modes: (a)  $j = 80 \text{ mA/cm}^2$ ,  $t = 30 \text{ min}$  and (b)  $j = 30 \text{ mA/cm}^2$ ,  $t = 60 \text{ min}$ , as well as via a two-stage process involving consecutively performed stages (a) and (b). For the latter samples IR spectra were recorded straight upon the synthesis and after 2-year storage in ambient conditions (series III and IV in Table 1, resp.). IR spectra of the studied samples are illustrated in Figures 4 and 5. The observed absorption bands are interpreted in accordance with reference data [29, 37–39] and summarized in Table 2.

The comparative analysis of the considered data indicates the following: IR spectra of all the studied por-Si samples involve absorption bands at 2958, 2927, and 2856  $\text{cm}^{-1}$  suggesting the presence of carbon-containing complexes on their surface. The amount of carbon-containing complexes grows with the increase of anodization current density (Figure 4). According to [36], the appearance of carbon-containing species on por-Si surface is determined by the electrochemical oxidation of an alcohol component of electrolyte yielding C=O groups reacting with surface hydroxyls. The sample obtained in a single stage at  $j = 30 \text{ mA/cm}^2$  and  $t = 60 \text{ min}$  is featured with a significantly reduced content of such species (among the discussed bands, only peaks at 2927 and 2856  $\text{cm}^{-1}$  corresponding to stretching antisymmetric vibrations of CH– in  $\text{CH}_2$  and CH, resp., are present in their spectra) compared with the sample prepared at higher current density. For the sample prepared using a two-stage synthesis their amount is further decreased. These data are in agreement with the conclusions that anodization at the second stage results in the formation of a new por-Si layer inside the silicon plate below the already formed layer (anodization front spreads inside the substrate) and etching of the top layer (Figure 2(a)). The content of nano- and mesopores also drops consequently resulting in the decrease of alcohol and its electrochemical oxidation products.

In the range 3100–3700  $\text{cm}^{-1}$  a broad absorption band is observed corresponding to surface hydroxyls (O–H bonds). The surface of obtained por-Si samples is featured with hydrophilicity (as suggested by the absence of bands at 948 and 644  $\text{cm}^{-1}$  intrinsic to Si–H bonds in the spectra of samples straight after preparation) mostly prominent in the case of anodization current density 30  $\text{mA/cm}^2$ .

The presence of absorption bands numbers 7 and 8 (1056–1160  $\text{cm}^{-1}$ ) responsible for antisymmetric stretching vibrations of SiO– in O–SiO and C–SiO is typical for the oxidation of a highly developed surface of por-Si.

2-year storage (samples of the series IV) results in the increase of peaks indicated by number 4 (the most intensive peak in this region corresponding to  $\text{O}_3\text{SiH}$  group) and number 5 (SiH–SiO<sub>2</sub> group) that in combination with a high intensity of antisymmetric stretching bands of SiO– in O–SiO and C–SiO probably reflects the oxide layer growth on

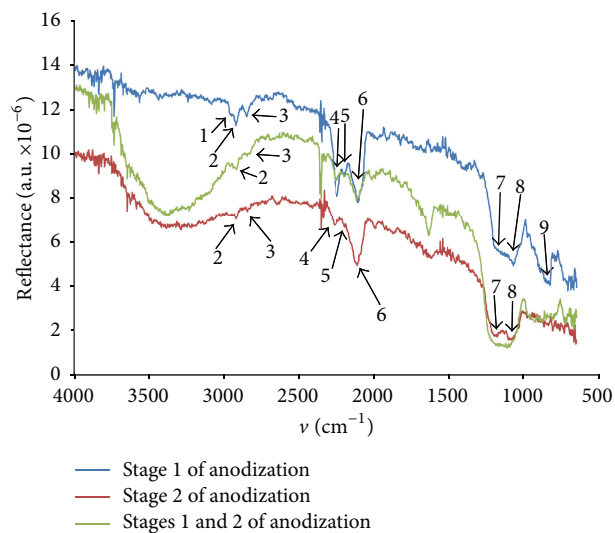


FIGURE 4: IR spectra of por-Si layers prepared straight before the characterization in the following conditions: the blue color: single-stage syntheses:  $j = 80 \text{ mA/cm}^2$ ,  $t = 30 \text{ min}$ ; the red color:  $j = 30 \text{ mA/cm}^2$ ,  $t = 60 \text{ min}$ ; the green color: two-stage synthesis, series III: stage 1:  $j = 80 \text{ mA/cm}^2$ ,  $t = 30 \text{ min}$ ; stage 2:  $j = 30 \text{ mA/cm}^2$ ,  $t = 60 \text{ min}$ .

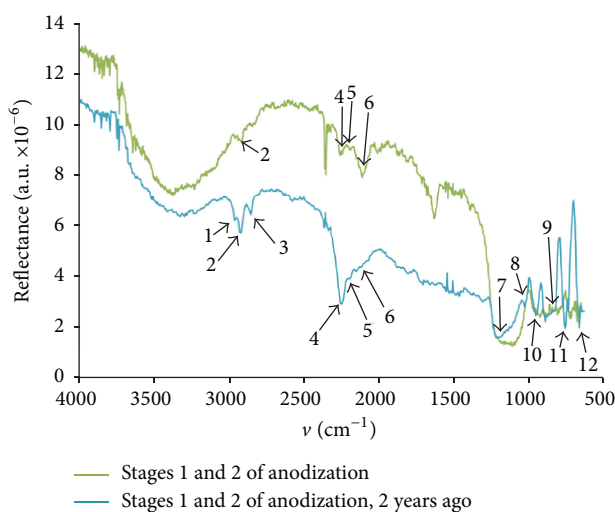


FIGURE 5: IR spectra of por-Si layers prepared by two-stage process straight before the characterization (green line) and stored within 2 years after the synthesis in the same conditions (blue line).

por-Si surface. A long time storage also led to the increase of bands 1–3 relating to carbon-containing complexes while the band at 3600–3200  $\text{cm}^{-1}$  decreased (as shown by the increased reflection in this region). The reduced absorption relating to O–H groups in this region can be attributed to the interaction of hydroxyls with alcohol-containing residues of the electrolyte and products of electrochemical oxidation of alcohols diffusing to the surface and forming carbon-containing species. Thus, redistribution of chemical bonds on por-Si surface proceeds in the course of storage. In

TABLE 2: IR absorption peaks in the por-Si samples interpreted according to [29, 37–39].

Number*	Band position, $\text{cm}^{-1}$	Interpretation
1	2958	Antisymmetric stretching vibrations of CH– in $\text{CH}_3$
2	2927	Antisymmetric stretching vibrations of CH– in $\text{CH}_2$
3	2856	Antisymmetric stretching vibrations of CH– in CH
4	2250	SiH– in $\text{O}_3\text{–SiH}$
5	2190	SiH– in $\text{SiO}_2\text{–SiH}$
6	2106	SiH– in $\text{Si}_2\text{H–SiH}$
7-8	1056–1160	Antisymmetric stretching vibrations of SiO– in O–SiO and C–SiO
9	827	Symmetric stretching vibrations of SiO in O–Si–O
10	948	SiH– in $\text{Si}_2\text{–H–SiH}$
11	760	Si–C
12	664	SiH– deformation vibrations

\* It corresponds to the relating numbers of absorption bands in Figures 4 and 5.

TABLE 3: Data of por-Si surface characterization by the adsorption of acid-base indicators with different  $\text{pK}_a$  values.

$\text{pK}_a$	Indicator	Supposed type of surface centers	Content of surface centers, nmole/ $\text{cm}^2$ (on both sides of $\sim 1 \times 1$ cm plates)	
			Series I Anodization current density 30 mA/ $\text{cm}^2$ , more uniform surface	Series II Anodization current density 80 mA/ $\text{cm}^2$ , less uniform surface
2.5	m-Nitroaniline	Acidic hydroxyls $\equiv\text{Si–OH}$	28,5	25,2
6.4	Bromocresol purple	Almost neutral hydroxyls $=\text{Si}(\text{OH})_2$	7,24	24,9
8.8	Thymol blue	Basic hydroxyls $-\text{Si}(\text{OH})_3$	1,17	10,1
14.2	Ethylene glycol	Si atoms	6,1	356

contrast with the fresh por-Si, the samples subjected to a 2-year ageing are featured with a growing surface passivation with hydrogen as indicated by the appearance of bands at  $948 \text{ cm}^{-1}$  (SiH– in  $\text{Si}_2\text{–H–SiH}$ ) and  $644 \text{ cm}^{-1}$  (SiH pendulum oscillations). It should be also noted that IR reflectance spectrum of por-Si after 2-year storage is more complicated in the region  $1000\text{–}600 \text{ cm}^{-1}$  compared with the same material straight after the synthesis.

**3.3. Indicator Adsorption Data on the Surface Functional Composition.** A detailed analysis of the surface functional composition using the selective adsorption of acid-base indicators with different  $\text{pK}_a$  values was carried out for hydrophilic por-Si layers obtained at two different anodization current values (series I and II). The results summarized in Table 3 indicate that the surface of samples prepared at the current density  $30 \text{ mA}/\text{cm}^2$  is predominantly occupied with Bronsted acidic centers with  $\text{pK}_a$  2.5 corresponding to  $\equiv\text{Si–OH}$  groups. The increase of current density to  $80 \text{ mA}/\text{cm}^2$  results in a drastic decrease in the content of these centers (in agreement with the observed decrease of hydrophilicity) and prevailing of Lewis acidic centers with  $\text{pK}_a$  14.2 probably formed by silicon atoms, in combination with a certain

increase in the concentration of Bronsted neutral ( $\text{pK}_a$  6.4) and basic ( $\text{pK}_a$  8.8) centers likely relating to  $=\text{Si}(\text{OH})_2$  and  $-\text{Si}(\text{OH})_3$  groups, respectively. Probably the synthesis performed in more “severe” conditions with a significantly higher current density results in “loosening” of the surface layer with multiple disruption of bonds to form versatile centers, including surface silicon atoms as well as “double” and “triple” hydroxyl groups.

## 4. Conclusions

Porous silicon layers are prepared by single- and two-stage anodization of monocrystalline n-type silicon (111) with the variation of anodization current density, number of synthesis stages, and their conditions as well as storage time after the preparation.

IR reflectance spectroscopy revealed the presence of absorption bands at 2958, 2927, and  $2856 \text{ cm}^{-1}$  indicating the presence of carbon-containing complexes on por-Si surface with the content of these species depending on the synthesis conditions. A broad absorption band corresponding to surface hydroxyls (O–H bonds) is also observed in the region  $3100\text{–}3700 \text{ cm}^{-1}$ .

The surface of obtained por-Si samples is found to possess hydrophilic properties (as suggested by the absence of bands at 948 and 644  $\text{cm}^{-1}$  intrinsic to Si–H bonds in the spectra of samples straight after preparation) mostly prominent in the case of anodization current density 30  $\text{mA}/\text{cm}^2$ .

The characterization of the prepared por-Si samples by adsorption of acid-base indicators with different  $\text{pK}_a$  values indicated a possibility for the control over their surface functional composition via the variation of the synthesis conditions. The surface of samples obtained at anodization current density 30  $\text{mA}/\text{cm}^2$  is predominantly occupied with  $\text{pK}_a$  2.5 corresponding to  $\equiv\text{Si}-\text{OH}$  groups. The increase of current density to 80  $\text{mA}/\text{cm}^2$  results in the increase of surface functional nonuniformity with the formation of versatile centers, primarily Lewis acidic sites corresponding to Si atoms, as indicated by selective indicator adsorption in agreement with the disappearance of Si–H bonds in IR spectra and overall disordering of the surface morphology according to REM and AFM data.

Generally, the obtained results demonstrate an approach to a wide range adjustment of por-Si porosity and surface properties to address various specific goals.

## Competing Interests

The authors declare that there are no competing interests regarding the publication of this paper.

## Acknowledgments

This study was supported by the Ministry of Education and Science of the Russian Federation within the framework of the project part of the state assignment for the St. Petersburg Electrotechnical University “LETI” (Project no. 16.2112.2014/K, Preparation and Study of Porous Systems, Functionalized Nanomaterials, Applications in Photonics, Sensor Technology and Medicine).

## References

- [1] R. J. Martín-Palma, M. Manso-Silván, and V. Torres-Costa, “Biomedical applications of nanostructured porous silicon: a review,” *Journal of Nanophotonics*, vol. 4, no. 1, Article ID 042502, 2010.
- [2] B. Gupta, Y. Zhu, B. Guan, P. J. Reece, and J. J. Gooding, “Functionalised porous silicon as a biosensor: emphasis on monitoring cells in vivo and in vitro,” *Analyst*, vol. 138, no. 13, pp. 3593–3615, 2013.
- [3] T. J. Barnes, K. L. Jarvis, and C. A. Prestidge, “Recent advances in porous silicon technology for drug delivery,” *Therapeutic Delivery*, vol. 4, no. 7, pp. 811–823, 2013.
- [4] V. Y. Shevchenko and O. I. Kiselev, Eds., *Chemical, Biological and Medical Aspects of the Synthesis and Application of Porous Nanocontainers for Drugs*, Handbook, Nauka, Saint-Petersburg, Russia, 2015 (Russian).
- [5] J. Rytönen, R. Miettinen, M. Kaasalainen, V.-P. Lehto, J. Salonen, and A. Närvänen, “Functionalization of mesoporous silicon nanoparticles for targeting and bioimaging purposes,” *Journal of Nanomaterials*, vol. 2012, Article ID 896562, 9 pages, 2012.
- [6] D. Liu, L. M. Bimbo, E. Mäkilä et al., “Co-delivery of a hydrophobic small molecule and a hydrophilic peptide by porous silicon nanoparticles,” *Journal of Controlled Release*, vol. 170, no. 2, pp. 268–278, 2013.
- [7] E. Secret, K. Smith, V. Dubljevic et al., “Antibody-functionalized porous silicon nanoparticles for vectorization of hydrophobic drugs,” *Advanced Healthcare Materials*, vol. 2, no. 5, pp. 718–727, 2013.
- [8] W. Xu, J. Riikonen, and V.-P. Lehto, “Mesoporous systems for poorly soluble drugs,” *International Journal of Pharmaceutics*, vol. 453, no. 1, pp. 181–197, 2013.
- [9] E. J. Anglin, L. Cheng, W. R. Freeman, and M. J. Sailor, “Porous silicon in drug delivery devices and materials,” *Advanced Drug Delivery Reviews*, vol. 60, no. 11, pp. 1266–1277, 2008.
- [10] J. L. Coffey, M. A. Whitehead, D. K. Nagesha et al., “Porous silicon-based scaffolds for tissue engineering and other biomedical applications,” *Physica Status Solidi (A)*, vol. 202, no. 8, pp. 1451–1455, 2005.
- [11] H. A. Santos, L. M. Bimbo, B. Herranz, M.-A. Shahbazi, J. Hirvonen, and J. Salonen, “Nanostructured porous silicon in preclinical imaging: moving from bench to bedside,” *Journal of Materials Research*, vol. 28, no. 2, pp. 152–164, 2013.
- [12] R.-X. Liu, L.-L. Chen, H.-Y. Zhang, and Z.-H. Jia, “A label-free single photonic quantum well biosensor based on porous silicon for DNA detection,” *Optoelectronics Letters*, vol. 9, no. 3, pp. 225–228, 2013.
- [13] L. M. Bimbo, O. V. Denisova, E. Mäkilä et al., “Inhibition of influenza A virus infection in vitro by saliphenylhalamide-loaded porous silicon nanoparticles,” *ACS Nano*, vol. 7, no. 8, pp. 6884–6893, 2013.
- [14] C. J. Shearer, F. J. Harding, M. J. Sweetman, J. G. Shapter, and N. H. Voelcker, “Nanostructured biointerfaces created from carbon nanotube patterned porous silicon films,” *Surface and Coatings Technology*, vol. 224, pp. 49–56, 2013.
- [15] S. B.-T. de-Leon, R. Oren, M. E. Spira, N. Korbakov, S. Yitzchaik, and A. Sa’ar, “Porous silicon substrates for neurons culturing and bio-photonic sensing,” *Physica Status Solidi (A): Applications and Materials Science*, vol. 202, no. 8, pp. 1456–1461, 2005.
- [16] A. Yurt, G. G. Daaboul, J. H. Connor, B. B. Goldberg, and M. Selim Ünlü, “Single nanoparticle detectors for biological applications,” *Nanoscale*, vol. 4, no. 3, pp. 715–726, 2012.
- [17] Y. Shang, W. Zhao, E. Xu, C. Tong, and J. Wu, “FTIRIS biosensor based on double layer porous silicon as a LC detector for target molecule screening from complex samples,” *Biosensors and Bioelectronics*, vol. 25, no. 5, pp. 1056–1063, 2010.
- [18] A. M. Noval, V. S. Vaquero, E. P. Quijorna et al., “Aging of porous silicon in physiological conditions: cell adhesion modes on scaled 1D micropatterns,” *Journal of Biomedical Materials Research A*, vol. 100, no. 6, pp. 1615–1622, 2012.
- [19] E. Punzón-Quijorna, V. Sánchez-Vaquero, Á. Muñoz-Noval et al., “Nanostructured porous silicon micropatterns as a tool for substrate-conditioned cell research,” *Nanoscale Research Letters*, vol. 7, article 396, 2012.
- [20] Y. M. Spivak, A. O. Belorus, P. A. Somov, S. S. Tulenin, K. A. Bepalova, and V. A. Moshnikov, “Porous silicon nanoparticles for target drug delivery: structure and morphology,” *Journal of Physics: Conference Series*, vol. 643, no. 1, Article ID 012022, 2015.

- [21] A. S. Lenshin, V. M. Kashkarov, Y. M. Spivak, and V. A. Moshnikov, "Investigations of nanoreactors on the basis of p-type porous silicon: electron structure and phase composition," *Materials Chemistry and Physics*, vol. 135, no. 2-3, pp. 293–297, 2012.
- [22] L. T. Canham, "Bioactive silicon structure fabrication through nanoetching techniques," *Advanced Materials*, vol. 7, no. 12, pp. 1033–1037, 1995.
- [23] C. A. Prestidge, T. J. Barnes, C.-H. Lau, C. Barnett, A. Loni, and L. Canham, "Mesoporous silicon: a platform for the delivery of therapeutics," *Expert Opinion on Drug Delivery*, vol. 4, no. 2, pp. 101–110, 2007.
- [24] B. Unal, "Quenching influence of cell culture medium on photoluminescence and morphological structure of porous silicon," *Applied Surface Science*, vol. 258, no. 1, pp. 207–211, 2011.
- [25] K. Kimoto and T. Arai, "Photoluminescence of rapid thermal treated porous Si in nitrogen atmosphere," *Physica Status Solidi (A)*, vol. 182, no. 1, pp. 133–137, 2000.
- [26] V. Morazzani, J. L. Cantin, C. Ortega et al., "Thermal nitridation of p-type porous silicon in ammonia," *Thin Solid Films*, vol. 276, no. 1-2, pp. 32–35, 1996.
- [27] L. M. Bimbo, O. V. Denisova, and E. Mäkilä, "Inhibition of influenza a virus infection in vitro by saliphenylhalamide-loaded porous silicon nanoparticles," *ACS Nano*, vol. 7, no. 8, pp. 6884–6893, 2013.
- [28] A. O. Belorus, E. V. Maraeva, Y. M. Spivak, and V. A. Moshnikov, "The study of porous silicon powders by capillary condensation," *Journal of Physics: Conference Series*, vol. 586, no. 1, Article ID 012017, 2015.
- [29] A. S. Lenshin, V. M. Kashkarov, P. V. Seredin, Y. M. Spivak, and V. A. Moshnikov, "XANES and IR spectroscopy study of the electronic structure and chemical composition of porous silicon on n- and p-type substrates," *Semiconductors*, vol. 45, no. 9, pp. 1183–1188, 2011.
- [30] A. S. Len'shin, V. M. Kashkarov, Y. M. Spivak, and V. A. Moshnikov, "Study of electronic structure and phase composition of porous silicon," *Glass Physics and Chemistry*, vol. 38, no. 3, pp. 315–321, 2012.
- [31] I. V. Vasil'eva, S. V. Myakin, E. V. Rylova, and V. G. Korsakov, "Electron-beam modification of the surface of oxide materials ( $\text{SiO}_2$  and  $\text{BaTiO}_3$ )," *Russian Journal of Physical Chemistry*, vol. 76, no. 1, pp. 71–76, 2002.
- [32] S. V. Mjakin, M. M. Sychov, and I. V. Vasilieva, Eds., *Electron Beam Modification of Functional Materials*, Petersburg State Transport University, Saint-Petersburg, Russia, 2006.
- [33] K. Imai and H. Unno, "FIPOS technology and its application to LSI's," *IEEE Transactions on Electron Devices*, vol. 31, pp. 297–302, 1984.
- [34] H. Föll, M. Christophersen, J. Carstensen, and G. Hasse, "Formation and application of porous silicon," *Materials Science and Engineering R: Reports*, vol. 39, no. 4, pp. 93–142, 2002.
- [35] M. F. Panov and V. V. Tomaev, "Optical reflection of oxidized PbSe films in the infrared spectral range," *Glass Physics and Chemistry*, vol. 38, no. 4, pp. 419–426, 2012.
- [36] A. A. Kopylov and A. N. Kholodilov, "Infrared absorption in porous silicon obtained in electrolytes containing ethanol," *Semiconductors*, vol. 31, no. 5, pp. 470–472, 1997.
- [37] A. Borghesi, A. Sassella, B. Pivac, and L. Pavesi, "Characterization of porous silicon inhomogeneities by high spatial resolution infrared spectroscopy," *Solid State Communications*, vol. 87, no. 1, pp. 1–4, 1993.
- [38] A. Borghesi, G. Guizzetti, A. Sassella, O. Bisi, and L. Pavesi, "Induction-model analysis of SiH stretching mode in porous silicon," *Solid State Communications*, vol. 89, no. 7, pp. 615–618, 1994.
- [39] V. P. Tolstoy, I. V. Chernyshova, and V. A. Skryshevsky, *Handbook of Infrared Spectroscopy of Ultrathin Films*, Wiley Interscience, 2003.

## Research Article

# Microwave-Assisted Solvent-Free Synthesis of Zeolitic Imidazolate Framework-67

Heng Zhang,<sup>1,2,3</sup> Jing Zhong,<sup>1,2,3</sup> Guoxiang Zhou,<sup>3</sup> Junliang Wu,<sup>3</sup> Zhenyu Yang,<sup>4</sup> and Xianming Shi<sup>5</sup>

<sup>1</sup>Key Laboratory of Structure Dynamic Behavior and Control (Harbin Institute of Technology), Ministry of Education, Harbin, Heilongjiang 150090, China

<sup>2</sup>School of Civil Engineering, Harbin Institute of Technology, Harbin 150090, China

<sup>3</sup>School of Civil Engineering and Architecture, Wuhan Polytechnic University, Wuhan 430023, China

<sup>4</sup>Department of Chemistry, Nanchang University, Nanchang 330031, China

<sup>5</sup>Department of Civil & Environmental Engineering, Washington State University, P.O. Box 642910, Pullman, WA 99164-2910, USA

Correspondence should be addressed to Jing Zhong; [zhongjing@hit.edu.cn](mailto:zhongjing@hit.edu.cn) and Xianming Shi; [xianming.shi@wsu.edu](mailto:xianming.shi@wsu.edu)

Received 17 December 2015; Revised 3 March 2016; Accepted 13 March 2016

Academic Editor: Gurvinder Singh

Copyright © 2016 Heng Zhang et al. This is an open access article distributed under the Creative Commons Attribution License, which permits unrestricted use, distribution, and reproduction in any medium, provided the original work is properly cited.

A microporous metal-organic framework (MOF), cobalt-based zeolitic imidazolate framework-67 (ZIF-67), was synthesized by the combination of solvent-free hand-mill and microwave irradiation, without any organic solvent and within 30 minutes. The hand-milling process can mix the reactants well by the virtue of high moisture/water absorption capacity of reactants. In addition, the outstanding electromagnetic wave absorption capability of cobalt leads to efficient conversion to MOF structures before carbonization. The obtained ZIF-67 possesses high surface area and micropore volume.

## 1. Introduction

Metal-organic frameworks (MOFs) are a family of highly porous crystalline materials, which consist of metal ions and ligands that are coordinated into 3D structures. In light of their unique physicochemical characteristics, MOFs have great potential for applications such as gas storage [1, 2], separation [3], drug delivery [4], heterogeneous catalysts [5], luminescence [6], magnetism [7], biomedical sensors [8], and heating transformation through reversible water adsorption and desorption [9]. MOFs feature very large specific surface area and pores size controllable and adjustable by the proper selection of metal ions and organic linkers [10, 11]. In addition, the organic linkers can be functionalized independently without sacrificing the geometrical characteristics of 3D porous structures, which is another unique advantage [12, 13].

Although MOFs have garnered increasing interests of researchers, there are still several factors limiting their practical applications [14, 15]. The use of organic solvents and long

synthesis time are two of the top challenges. Organic solvents pose the risk to operators and the natural environment, leading to limited autoclave availability, whereas the long synthesis time tends to translate to high energy consumption and cost.

There are several strategies to address challenges in synthesizing MOFs, among which the solvent-free (SF) synthesis and microwave (MW) synthesis are very promising [16, 17]. For instance, Lin et al. reported that the porous metal azolate framework can be synthesized by simply heating the mixture of metal oxide/hydroxide and azole ligand only [18]. Friscic adopted “accelerated aging” to assist the synthesis of multi-gram of metal-organic framework without using solvents, high temperature, or another activation [19]. Nonetheless, with few exceptions [20], SF mixing alone without any subsequent or concurrent treatment, such as hydrothermal process, would not effectively produce MOFs. While it is essential to mix the solid reactants well in order to synthesize uniform MOF particles, this can only be partially achieved

with the aid of ball milling [21, 22]. Microwave-assisted synthesis of MOFs has proven its effectiveness in recent years [23, 24]. Microwave absorption can induce vibration of atoms and molecules and thus convert mechanical energy to thermal energy, which induces chemical reactions very efficiently [25]. The polar solvents, which have high dielectric absorptivity, function as thermal conversion agents to eliminate local superheat spots, promoting fast and homogeneous nucleation over the MOF growth process. In this study, a hypothesis to test is that the efficiency of MW treatment should also depend on the wave absorption capability of the metal ions. This factor, to the best of our knowledge, has not been considered in previous studies.

Zeolitic imidazolate frameworks (ZIFs) are a class of MOFs that are topologically isomorphic with zeolites, in which tetrahedrally coordinated transition metal ions are connected by imidazole linkers [26]. The structure of ZIFs is highly stable, and it can be heated to high temperatures without decomposing, making them suitable for use in hot environments [27]. Tanaka et al. reported a mechanochemical dry conversion of ZnO to ZIF-8 by ball milling, which avoids the use of organic solvents using excess amount of 2-methylimidazole. And the BET surface area of obtained ZIF-8 reached the maximum ( $1480\text{ m}^2\text{ g}^{-1}$ ) after milling for 96 h [28]. Subsequently, Lanchas et al. used 1-butanol, pyridine, and 4-methylpyridine as structure directing agents to generate ZIF single crystals above  $88\text{--}90^\circ\text{C}$  [29]. Lin et al. also reported that the porous metal azolate framework can be synthesized by heating the mixture of metal oxide/hydroxide and azole ligand at  $100^\circ\text{C}$  for 24 h [18]. Although it has been reported that ZIF-67 can be obtained within several minutes by hydrothermal methods, either excess 2-methylimidazole ( $\text{Zn}^{2+} : 2\text{-methylimidazole} : \text{H}_2\text{O} = 1 : 70 : 1238$ ) or additives [30, 31], such as trimethylamine, are needed, which results in the waste of reactants and pollution to the environment. In addition, the samples synthesized within minutes by normal solvothermal/hydrothermal methods generally have lower surface areas and smaller pore volumes. A mechanochemical synthesis of ZIFs in which crystal formation can be completed within several minutes has not been reported. Interestingly, we also noticed that the cobalt ions in ZIFs have excellent electromagnetic wave absorption properties [32–34] and thus may facilitate the fast synthesis of ZIFs via the MW treatment method.

Here, we describe a very rapid method for the synthesis of cobalt-based zeolitic imidazolate framework-67 (ZIF-67), taking the advantages of coupling SF and MW treatments. The goal is to eliminate the use of organic solvent in the process and shorten the synthesis time to less than 30 minutes, including 20 minutes for manual grinding and 5 minutes for the crystallization.

## 2. Experimental Section

**2.1. Materials.** All the reagents, including cobalt nitrate hexahydrate (98%, Sigma-Aldrich), 2-methylimidazole (99%, Sinopharm), and cobalt nitrate hexahydrate (98%, Sigma-Aldrich) were used as received.

**2.2. Preparation of ZIF-67.** The preparation of ZIF-67 consisted of three steps: (1) mixing the starting materials by mechanical attrition at room temperature for 20 min; (2) production of ZIF-67 crystals with MW-irradiation; (3) washing the as-synthesized ZIF-67 with methanol for 3 times. Specifically, 895 mg 2-methylimidazole was finely powdered in an agate mortar for 5 min; then 404.8 mg  $\text{Co}(\text{NO}_3)_2 \cdot 6\text{H}_2\text{O}$  was added and the mixture was ground for another 15 min. The resulting mixture was transferred into a quartz boat and placed in a domestic microwave oven and heated for 5 min. The obtained solid, termed SF\_MW ZIF-67, was washed with methanol for 3 times and then separated by centrifugation. Domestic microwave oven (G90W25M SP-WD) was used, with the power of 900 W.

We also tested whether the addition of cobalt-containing salt to the precursors of Zn-based MOFs can facilitate the formation of Zn-based MOFs. We prepared ZIF-8 with the solvent-free method by adding small amount of cobalt source ( $\text{Co}(\text{NO}_3)_2 \cdot 6\text{H}_2\text{O}$ ) into the starting materials. 785 mg of 2-methylimidazole was ground for 5 minutes, followed by the addition of 642 mg of  $\text{Zn}(\text{NO}_3)_2 \cdot 6\text{H}_2\text{O}$ . Then 166 mg of  $\text{Co}(\text{NO}_3)_2 \cdot 6\text{H}_2\text{O}$  was added and ground for another 15 minutes. The microwave treatment is the same as that of the SF\_MW ZIF-67.

**2.3. Characterization.** The structures of the ZIF-67 crystals were investigated by scanning electron microscopy (HELIOS Nanolab 600i); X-ray diffraction (XRD, Empyrean series 2, PANalytical) and infrared spectrum (IR, Frontier Optical, PE) surface areas were measured by 3H-2000PS1 Specific & Pore Size Analysis Instrument (BeiShiDe Instrument).

## 3. Results and Discussion

During the solvent-free (SF) synthesis of MOF, mechanical grinding is required to promote the reactions between solid reactants through multiple mechanisms, including heating, defects formation, particle size reduction, local melting, and even phase changes to other polymorphs [32]. Ball mill is generally preferred to grind the solid reactants, since it can supply high power, being programmable, and result in smaller particles with small polydispersity [17]. In this study, however, instead of ball mill, we use hand-mill only to accelerate the moisture/water absorption of the solid reactants. Once the two reactants are mixed and ground, the solid mixture turns into blue liquid (Figures 1(a) and 1(b)) within several minutes (which is dependent on the air humidity). It is mainly caused by the high moisture absorption capability of cobalt nitrate hexahydrate. The quantity of absorbed moisture seems large enough to dissolve all reactants (cobalt nitrate hexahydrate and 2-methylimidazole) without any noticeable solid particles, making the reactants well mixed. Upon further hand-milling for several minutes, solid pink particles (Figure 1(c)) gradually precipitated until the whole liquid mixture eventually changed back into solid particles. This is because 2-methylimidazole can gradually absorb water in the liquid mixture as long as it is not saturated. Such solid-liquid-solid phase change during hand-milling

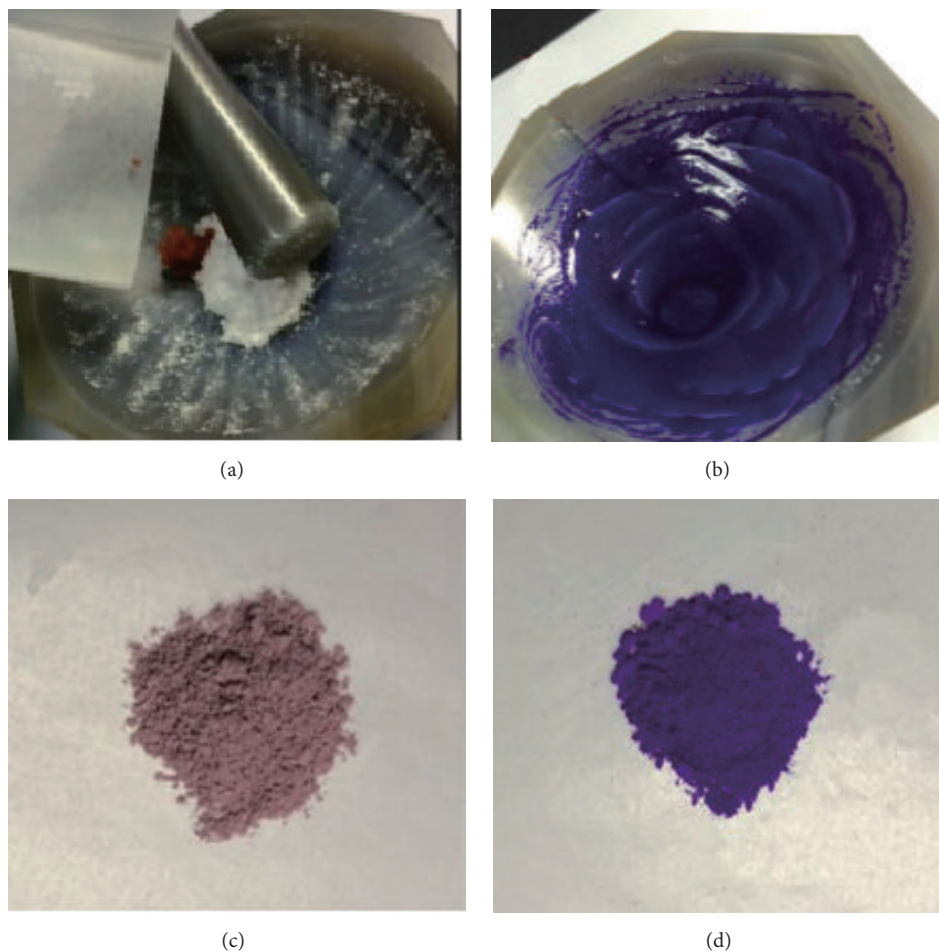


FIGURE 1: Photographs of starting materials (a), the liquid mixtures (b), and products before MW-irradiation (c) and after MW-irradiation (d).

can greatly facilitate the unprecedented uniform mixing of the solid reactants. Since the input energy to the reactants during hand-milling is negligible comparing to ball milling process, the mechanism related to the mechanochemical synthesis probably cannot be applied to the situation of hand-milling. Indeed, as will be discussed in the following, the obtained solid particles after hand-milling do not possess any structural characteristics of ZIF-67. Those pink particles are then treated by MW-irradiation, which is necessary for the synthesis of ZIF-67 in this study. Upon MW treatment, it can be observed that the color of the particles changed from pink to purple (Figures 1(c) and 1(d)). It is worth pointing out that although the MW oven we used in this study is domestic and cheap instead of programmable and expensive industry MW oven, the physical/chemical properties of the obtained ZIF-67 are quite stable for more than five times synthesis and confirm the reproducibility.

Figure 2 presents SEM images of the ZIF-67 samples synthesized by the SF method. The samples maintain the rhombic dodecahedral shape, which is consistent with ZIF-67 prepared by autoclaved method. However, the average size of the SF samples is about 500 nm, which is much

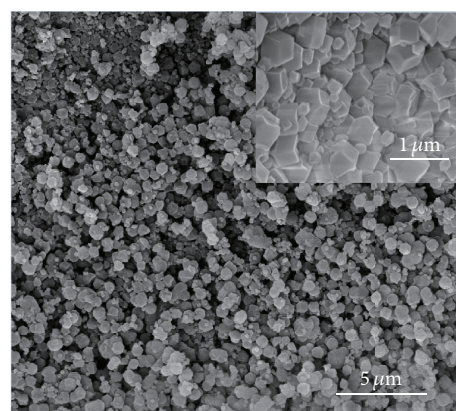


FIGURE 2: SEM images of ZIF-67 crystals.

smaller than the traditional one. This may be due to its short synthesis time resulting in a fast nucleation and short growth rate during the SF process. Figure 3 shows the structures of ZIF-67 at different MW-irradiation time. The structure

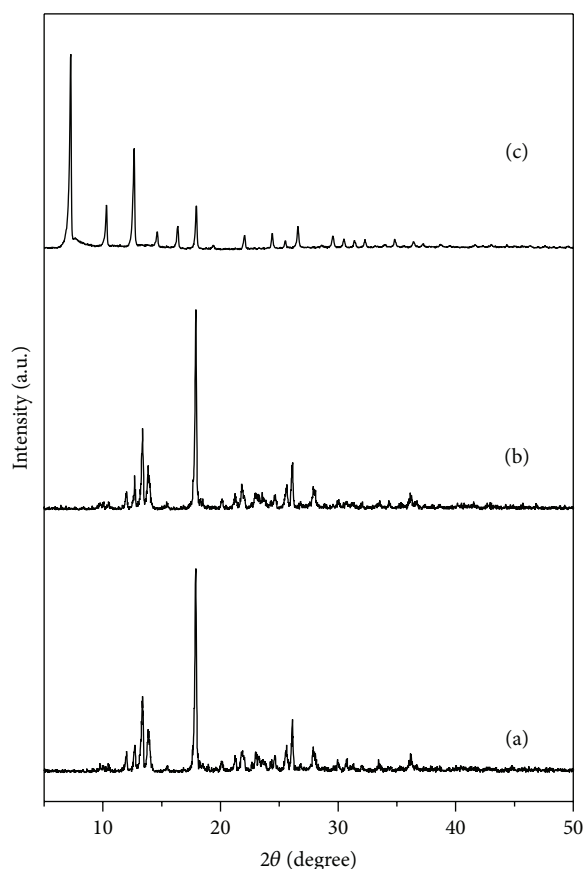


FIGURE 3: XRD patterns of as-synthesized ZIF-67 products under MW-irradiation for 0 min (a), 1 min (b), and 5 min (c).

and high crystallinity of our prepared ZIF-67 product are confirmed by the XRD patterns shown in Figure 3(c). The positions of diffraction peaks agree well with the simulated one. A favorable orientation of (110) direction was observed, from the highest peak at 2 theta value of 7.3 degrees, which represents (110) plane of ZIF-67 crystals. We can see from Figures 3(a) and 3(b) that, with no or not enough MW-irradiation, the peaks of the products do not conform to the simulated one, indicating no ZIF-67 structure was generated. This phenomenon was further certified by FTIR spectroscopy (Figure 4). From the comparison between the samples before and after MW-irradiation, we can see that, before microwave-assisted heating, the as-synthesized ZIF-67 precursors obtained by just grinding exhibit peaks in accordance with 2-methylimidazole as reported in literature [35], implying no ZIF-67 product was prepared. However, after MW treatment, a new absorption band at  $477\text{ cm}^{-1}$  was displayed, manifesting the Co-N stretching, which proved the existence of ZIF-67 structure. On the other hand, the duration of MW-irradiation should be carefully controlled to prevent the overheating of the particles. In this study, the samples are cooled down after each 1 min in MW treatment for the prevention of the collapse of the framework and even its carbonization.

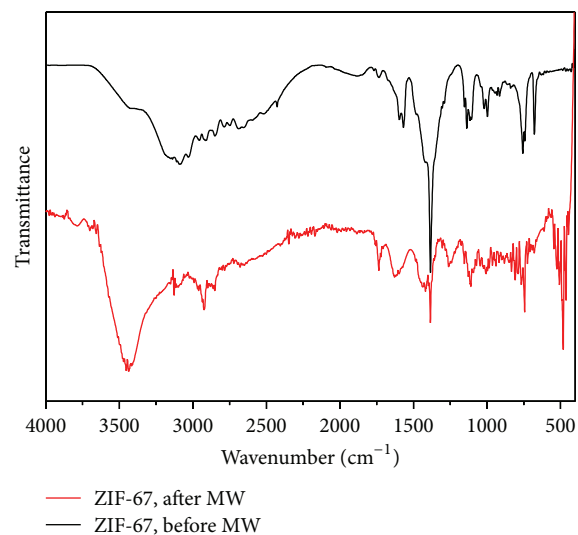


FIGURE 4: IR spectrum of SF\_MW ZIF-67 crystals.

Figure 5(a) shows nitrogen adsorption isotherm of SF\_MW ZIF-67, which is a Type I isotherm, representing a micropore structure. The Brunauer-Emmett-Teller (BET) specific surface area and Langmuir specific surface area of ZIF-67 are calculated to be  $1120\text{ m}^2/\text{g}$  and  $1562\text{ m}^2/\text{g}$ , respectively. A pore size distribution ranging from 1.24 nm to 1.36 nm, based on the Horvath-Kawazoe (H-K) model, is shown as in Figure 5(b). The peak at 1.3 nm probably resulted from the distortion of the second-building unit (SBU), which is formed through the reaction of  $\text{Co}^{2+}$  and 2-MIm during the hand mixing or microwave radiation. Considerable energy will be absorbed by the reaction system during the microwave radiation treatment, and it not only accelerates the formation of MOF but also might be able to distort the already formed SBU. As can be seen from the complementary experiments, in which the microwave radiation time decreased from 1 minute to 30 seconds, the size of the pores decreases obviously and the peak at 1.3 nm disappears. Clearly, the microwave radiation treatment time has some impact on the pore size distribution.

For the solvent-free microwave heating method in this study, we prepared ZIF-67 with the reactant quantity much closer to stoichiometric Co-2MI ratio (1:7.94), in which not only does it improve the reagent utilization efficiency and avoid using of poison reagents, but also the resultant MOFs have higher surface area ( $1120\text{ m}^2/\text{g}$ ) and micropore volume ( $0.52\text{ mL/g}$ ). Actually, those values are similar to the MOFs obtained by traditional solvothermal/hydrothermal samples ( $>100^\circ\text{C}$ , 1 h to 1 month). We further carried out experiments by shortening the heating time during each heating and cooling process. It was found that when the heating time decreases from 1 minute to 30 seconds (Figure 6), the surface area and micropore volume can be enhanced to  $1591\text{ m}^2/\text{g}$  and  $0.74\text{ cm}^3/\text{g}$ , respectively, which fully testified the accessibility of this approach and, by optimizing the preparation conditions, we can synthesize ZIF-67 solids with good quality within several minutes but without using any

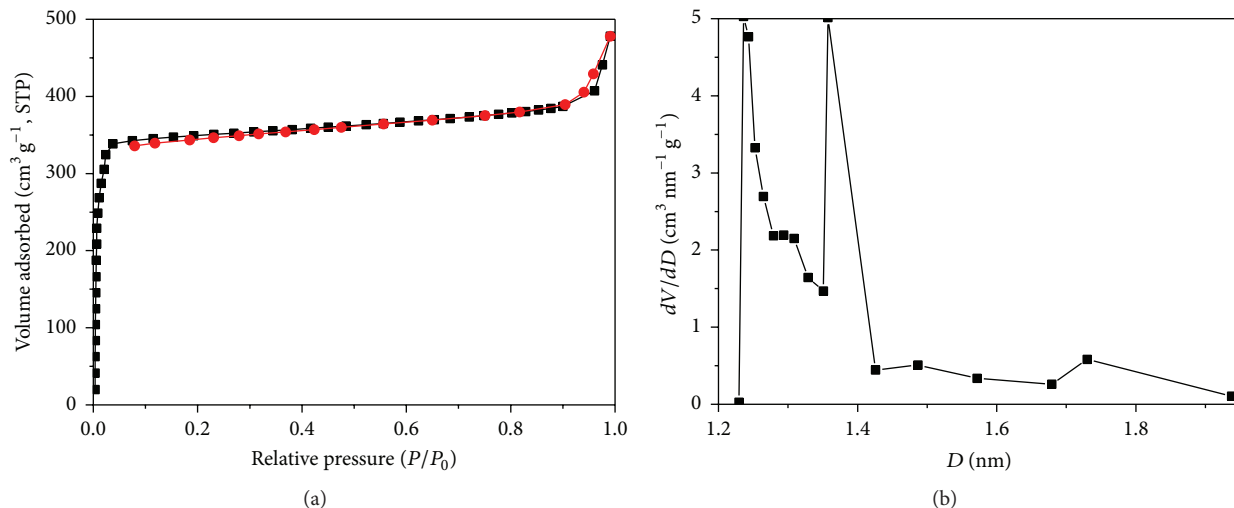


FIGURE 5:  $N_2$  adsorption-desorption isotherms (a) and H-K micropore size distribution (b) of SF\_MW ZIF-67.

TABLE 1: Physical properties of different samples.

Samples	Mean pore size (nm)	$S_{BET}$ ( $m^2/g$ )	Micropore volume ( $cm^3/g$ )
C-ZIF-67	1.17	1725	0.82
SF_MW ZIF-67-1	1.18	1120	0.52
SF_MW ZIF-67-2	1.31	1591	0.74

C-ZIF-67, ZIF-67 samples synthesized by the conventional solvothermal method.

SF\_MW ZIF-67-1, ZIF-67 samples synthesized by the SF\_MW method, in which heating time is 1 minute.

SF\_ZIF-67-2, ZIF-67 samples synthesized by the SF\_MW method, in which heating time is 30 s.

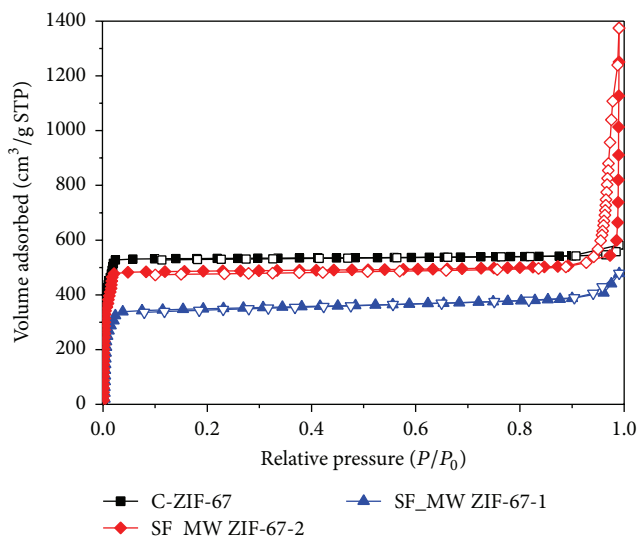


FIGURE 6:  $N_2$  adsorption isotherms of different samples.

poisonous reagent or waste of reactants. We also compare the porous structures of ZIF-67 obtained via MW treatment with conventional solvothermal method. From Figure 7, the lattice distance of the SF\_MW ZIF-67 increased, while the particle size reduced from 800 nm to 500 nm, implying that the pore size increased through MW treatment. This was confirmed by the pore size distribution by  $N_2$  adsorption testing in Table 1,

which shows a pore size distribution ranging from 1.24 nm to 1.36 nm and a median pore diameter of 1.31 nm. This is much larger than the conventional ones with a median pore diameter of 1.17 nm and pore volume (at  $P/P_0 = 0.024$ ) of  $0.82 \text{ cm}^3/g$ . In addition, the pore volume of the MW samples can be increased by tuning the heating time from 1 minute to 30 s (total MW heating time is the same, i.e., 5 min) in every MW heating interval (63%,  $P/P_0 = 0.038$ ,  $0.52 \text{ cm}^3/g$  versus 90%,  $P/P_0 = 0.021$ ,  $0.74 \text{ cm}^3/g$ ). Meanwhile, the mean pore size also decreases to 1.18 nm, which is similar with the traditional ones. This phenomenon illustrates that the porosity can be tuned by varying the heating intervals during the SF\_MW process, which can facilitate the generation of hierarchical pores.

We also apply the same procedure to synthesize ZIF-8. However, MW-irradiation directly converts the particles into amorphous carbon instead of ZIF-8, and the addition of extra water to the precursors of ZIF-8 during hand mix still cannot prevent the carbonization (Figure 8). Further, we testified whether our method applies to those ZIF or MOF systems that can only be synthesized in solvothermal conditions, in which we tried the synthesis of MOF-5. Unfortunately, there is no MOF-5 generated according to the XRD analysis (Figure 9). Such distinct comparison clearly illustrates the importance of electromagnetic wave absorption capability of metal ions. Cobalt is one of the most effective electromagnetic wave absorbents. When irradiated by electromagnetic waves, cobalt ions act as superheat spots and trigger

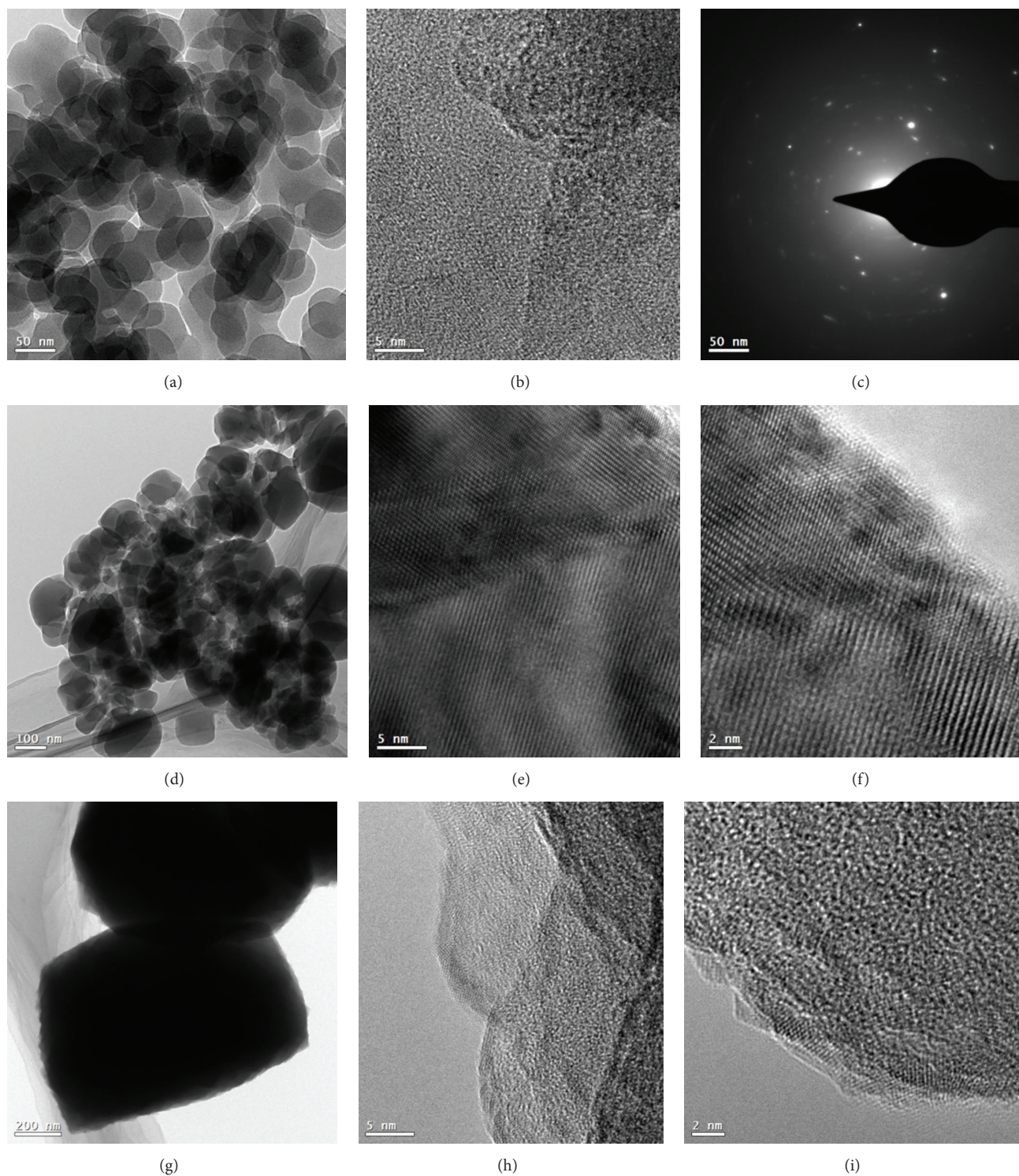


FIGURE 7: TEM images of the as-synthesized SF\_MW ZIF-8 particles (a, b, c), SF\_MW ZIF-67 particles (d, e, f), and C-ZIF-67 particles (g, h, i).

the complexation between the metal ions and ligands to form stable 3D microporous MOF structures. Therefore, the MOF formation mechanism during MW treatment in this study should be very different from the conventional ones where it is the organic solvent that acts as heating spot

as we discussed previously. In addition, we expected that the existence of cobalt would facilitate the production of ZIF-8 due to its microwave-absorbing properties. We added a minimum of  $\text{Co}(\text{NO}_3)_2 \cdot 6\text{H}_2\text{O}$  to the precursors for the synthesis of ZIF-8, and the results of this experiment testified

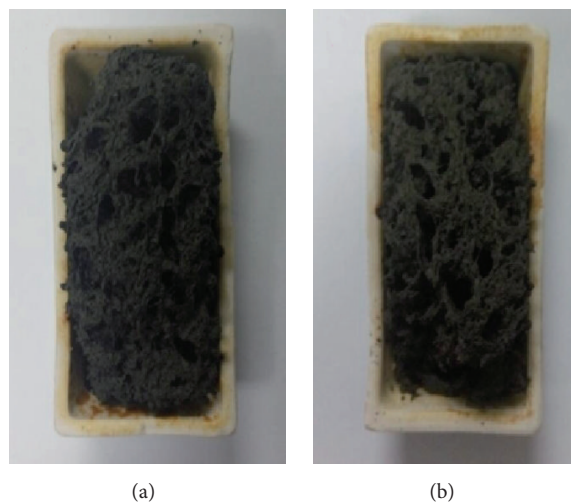


FIGURE 8: Images for the samples obtained by the microwave radiation for the precursors of ZIF-8 with extra (a) 10 mL water and (b) 100 mL water.

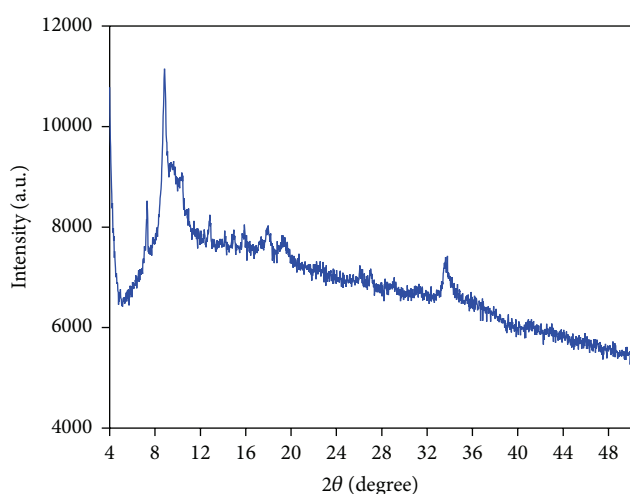


FIGURE 9: XRD for the samples obtained by hand mixing and microwave treatment for the precursors of MOF-5.

our assumption. It can be clearly seen from Figure 10 that there is a peak at  $417\text{ cm}^{-1}$  in the IR spectrum of SF\_MW ZIF-8/ZIF-67, which represented the Zn-N stretching, implying the formation of ZIF-8 structure. When compared to the IR spectrum of SF\_MW ZIF-67, the difference was evident between  $400\text{ cm}^{-1}$  and  $500\text{ cm}^{-1}$ . In SF\_MW ZIF-67, as exemplified in Figure 4, the adsorption band is at  $477\text{ cm}^{-1}$ , which is the characteristic for Co-N stretching. Therefore, ZIF-8 was prepared successfully with the existence of cobalt nitrate. The TEM images in Figure 7(a) revealed that the particle size of ZIF-8 was about 50 nm with hexagonal shape.

#### 4. Conclusions

In this study, we combine hand-milling with MW-irradiation methods to synthesize ZIF-67. This avoids the use of organic

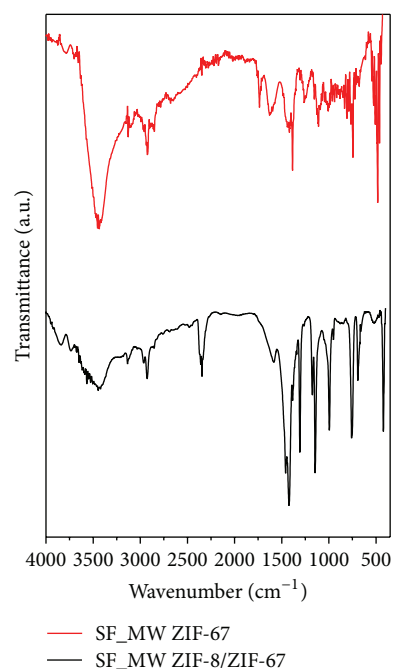


FIGURE 10: IR spectrum of SF\_MW ZIF-67 (red) and SF\_MW ZIF-8/ZIF-67 (black).

solvent and shortens the synthesis time to less than 30 minutes. The hand-milling process is to mix the solid reactants well, whereas the MW-irradiation successfully converts the participating reactant particles to ZIF-67. The synthesized ZIF-67 features high surface area and micropore volume. We also show that the electromagnetic wave absorption capability of metal ions plays a key role in the successful conversion of reactants to MOFs, which merits further investigation.

## Competing Interests

The authors have confirmed that there are no competing interests related to this paper.

## Acknowledgments

The research was financially supported by the National Science Foundation of China (no. 51402074 and no. 21263016), Jiangsu Postdoctoral Science Foundation (1402129C), the Six Talent Peaks Program of Jiangsu Province (2013-ZBZZ-032), and the Lianyungang Scientific Plan-Joint Project of Industry-Academia-Research (CXY1405).

## References

- [1] S. Kitagawa, R. Kitaura, and S.-I. Noro, "Functional porous coordination polymers," *Angewandte Chemie—International Edition*, vol. 43, no. 18, pp. 2334–2375, 2004.
- [2] J. G. Bünzli and C. Piguet, "Taking advantage of luminescent lanthanide ions," *Chemical Society Reviews*, vol. 34, no. 12, pp. 1048–1077, 2005.
- [3] S. Ma, D. Sun, M. Ambrogio, J. A. Fillinger, S. Parkin, and H.-C. Zhou, "Framework-catenation isomerism in metal-organic frameworks and its impact on hydrogen uptake," *Journal of the American Chemical Society*, vol. 129, no. 7, pp. 1858–1859, 2007.
- [4] G. Férey, "Hybrid porous solids: past, present, future," *Chemical Society Reviews*, vol. 37, no. 1, pp. 191–214, 2008.
- [5] J. A. Real, E. Andrés, M. C. Muñoz et al., "Spin crossover in a catenane supramolecular system," *Science*, vol. 268, no. 5208, pp. 265–267, 1995.
- [6] J. W. Han and C. L. Hill, "A coordination network that catalyzes O<sub>2</sub>-based oxidations," *Journal of the American Chemical Society*, vol. 129, no. 49, pp. 15094–15095, 2007.
- [7] H. A. Habib, J. Sanchiz, and C. Janiak, "Magnetic and luminescence properties of Cu(II), Cu(II)<sub>4</sub>O<sub>4</sub> core, and Cd(II) mixed-ligand metal-organic frameworks constructed from 1,2-bis(1,2,4-triazol-4-yl)ethane and benzene-1,3,5-tricarboxylate," *Inorganica Chimica Acta*, vol. 362, no. 7, pp. 2452–2460, 2009.
- [8] M. Müller, S. Hermes, K. Kähler, M. W. van den Berg, M. Muhler, and R. A. Fischer, "Loading of MOF-5 with Cu and ZnO nanoparticles by gas-phase infiltration with organometallic precursors: properties of Cu/ZnO@MOF-5 as catalyst for methanol synthesis," *Chemistry of Materials*, vol. 20, no. 14, pp. 4576–4587, 2008.
- [9] O. R. Evans and W. Lin, "Crystal engineering of NLO materials based on metal-organic coordination networks," *Accounts of Chemical Research*, vol. 35, no. 7, pp. 511–522, 2002.
- [10] J. G. Vitillo, "Magnesium-based systems for carbon dioxide capture, storage and recycling: from leaves to synthetic nanostructured materials," *RSC Advances*, vol. 5, no. 46, pp. 36192–36239, 2015.
- [11] N. L. Rosi, J. Eckert, M. Eddaoudi et al., "Hydrogen storage in microporous metal-organic frameworks," *Science*, vol. 300, no. 5622, pp. 1127–1129, 2003.
- [12] M. Eddaoudi, J. Kim, D. Vodak et al., "Geometric requirements and examples of important structures in the assembly of square building blocks," *Proceedings of the National Academy of Sciences of the United States of America*, vol. 99, no. 8, pp. 4900–4904, 2002.
- [13] M. P. Suh, Y. E. Cheon, and E. Y. Lee, "Syntheses and functions of porous metallosupramolecular networks," *Coordination Chemistry Reviews*, vol. 252, no. 8–9, pp. 1007–1026, 2008.
- [14] B. Chen, C. Liang, J. Yang et al., "A microporous metal-organic framework for gas-chromatographic separation of alkanes," *Angewandte Chemie-International Edition*, vol. 45, no. 9, pp. 1390–1393, 2006.
- [15] J. D. Evans, C. J. Sumby, and C. J. Doonan, "Post-synthetic metalation of metal-organic frameworks," *Chemical Society Reviews*, vol. 43, no. 16, pp. 5933–5951, 2014.
- [16] N. Stock and S. Biswas, "Synthesis of metal-organic frameworks (MOFs): routes to various MOF topologies, morphologies, and composites," *Chemical Reviews*, vol. 112, no. 2, pp. 933–969, 2012.
- [17] A. Pichon, A. Lazuen-Garay, and S. L. James, "Solvent-free synthesis of a microporous metal-organic framework," *CrysoEngComm*, vol. 8, no. 3, pp. 211–214, 2006.
- [18] J.-B. Lin, R.-B. Lin, X.-N. Cheng, J.-P. Zhang, and X.-M. Chen, "Solvent/additive-free synthesis of porous/zeolitic metal azolate frameworks from metal oxide/hydroxide," *Chemical Communications*, vol. 47, no. 32, pp. 9185–9187, 2011.
- [19] C. M. Mottillo, Y. Lu, M. H. Pham, M. J. Cliffe, T. Do, and T. Friščić, "Mineral neogenesis as an inspiration for mild, solvent-free synthesis of bulk microporous metal-organic frameworks from metal (Zn, Co) oxides," *Green Chemistry*, vol. 15, no. 8, pp. 2121–2131, 2013.
- [20] Z. Ni and R. I. Masel, "Rapid production of metal-organic frameworks via microwave-assisted solvothermal synthesis," *Journal of the American Chemical Society*, vol. 128, no. 38, pp. 12394–12395, 2006.
- [21] O. K. Farha and J. T. Hupp, "Rational design, synthesis, purification, and activation of metal-organic framework materials," *Accounts of Chemical Research*, vol. 43, no. 8, pp. 1166–1175, 2010.
- [22] T. Friščić, I. Halasz, P. J. Beldon et al., "Real-time and *in situ* monitoring of mechanochemical milling reactions," *Nature Chemistry*, vol. 5, pp. 66–73, 2013.
- [23] J. Klinowski, F. A. Almeida Paz, P. Silva, and J. Rocha, "Microwave-assisted synthesis of metal-organic frameworks," *Dalton Transactions*, vol. 40, no. 2, pp. 321–330, 2011.
- [24] S. T. Meek, J. A. Greathouse, and M. D. Allendorf, "Metal-organic frameworks: a rapidly growing class of versatile nanoporous materials," *Advanced Materials*, vol. 23, no. 2, pp. 249–267, 2011.
- [25] E. R. Parnham and R. E. Morris, "Ionothermal synthesis of zeolites, metal-organic frameworks, and inorganic-organic hybrids," *Accounts of Chemical Research*, vol. 40, no. 10, pp. 1005–1013, 2007.
- [26] G. Lu and J. T. Nupp, "Metal-organic frameworks as sensors: a ZIF-8 based Fabry-Pérot device as a selective sensor for chemical vapors and gases," *Journal of the American Chemical Society*, vol. 132, no. 23, pp. 7832–7833, 2010.
- [27] K. S. Park, Z. Ni, A. P. Cote et al., "Exceptional chemical and thermal stability of zeolitic imidazolate frameworks," *Proceedings of the National Academy of Sciences of the United States of America*, vol. 103, no. 27, pp. 10186–10191, 2006.
- [28] S. Tanaka, K. Kida, T. Nagaoka, T. Ota, and Y. Miyake, "Mechanochemical dry conversion of zinc oxide to zeolitic imidazolate framework," *Chemical Communications*, vol. 49, no. 72, pp. 7884–7886, 2013.
- [29] M. Lanchas, D. Vallejo-Sánchez, G. Beobide et al., "A direct reaction approach for the synthesis of zeolitic imidazolate frameworks: template and temperature mediated control on

- network topology and crystal size,” *Chemical Communications*, vol. 48, no. 79, pp. 9930–9932, 2012.
- [30] Y. Pan, Y. Liu, G. Zeng, L. Zhao, and Z. Lai, “Rapid synthesis of zeolitic imidazolate framework-8 (ZIF-8) nanocrystals in an aqueous system,” *Chemical Communications*, vol. 47, no. 7, pp. 2071–2073, 2011.
- [31] A. F. Gross, E. Sherman, and J. J. Vajo, “Aqueous room temperature synthesis of cobalt and zinc sodalite zeolitic imidazolate frameworks,” *Dalton Transactions*, vol. 41, no. 18, pp. 5458–5460, 2012.
- [32] A. Lew, P. O. Krutzik, M. E. Hart, and A. R. Chamberlin, “Increasing rates of reaction: microwave-assisted organic synthesis for combinatorial chemistry,” *Journal of Combinatorial Chemistry*, vol. 4, no. 2, pp. 95–105, 2002.
- [33] J. A. Gerbec, D. Magana, A. Washington, and G. F. Strouse, “Microwave-enhanced reaction rates for nanoparticle synthesis,” *Journal of the American Chemical Society*, vol. 127, no. 45, pp. 15791–15800, 2005.
- [34] K. J. Rao, B. Vaidhyanathan, M. Ganguli, and P. A. Ramakrishnan, “Synthesis of inorganic solids using microwaves,” *Chemistry of Materials*, vol. 11, no. 4, pp. 882–895, 1999.
- [35] X. Li, X. Gao, L. Ai, and J. Jiang, “Mechanistic insight into the interaction and adsorption of Cr(VI) with zeolitic imidazolate framework-67 microcrystals from aqueous solution,” *Chemical Engineering Journal*, vol. 274, pp. 238–246, 2015.

## Research Article

# Porous Gold Films Fabricated by Wet-Chemistry Processes

Aymeric Pastre,<sup>1</sup> Odile Cristini,<sup>2</sup> Alexandre Boe,<sup>1</sup> Katarzyna Raulin,<sup>1</sup> Bertrand Grimbert,<sup>1</sup> Fernand Chassagneux,<sup>3</sup> Nathalie Rolland,<sup>4</sup> and Remy Bernard<sup>2</sup>

<sup>1</sup>*Institut d'Electronique de Microélectronique et de Nanotechnologie (IEMN), CNRS, UMR 8520, Université Lille 1, 59658 Villeneuve d'Ascq Cedex, France*

<sup>2</sup>*Physique des Lasers Atomes et Molécules (PhLAM), CNRS, UMR 8523, Université Lille 1, 59655 Villeneuve d'Ascq Cedex, France*

<sup>3</sup>*Laboratoire des Multimatériaux et Interfaces (LMI), CNRS, UMR 5615, Université Lyon 1, 69622 Villeurbanne Cedex, France*

<sup>4</sup>*Institut de Recherche sur les Composants Logiciels et Matériels pour l'Information et la Communication Avancée (IRCICA), CNRS, USR 3380, Université Lille 1, 59658 Villeneuve d'Ascq Cedex, France*

Correspondence should be addressed to Aymeric Pastre; [aymeric.pastre@univ-lille1.fr](mailto:aymeric.pastre@univ-lille1.fr)

Received 5 November 2015; Revised 29 January 2016; Accepted 7 February 2016

Academic Editor: Gurvinder Singh

Copyright © 2016 Aymeric Pastre et al. This is an open access article distributed under the Creative Commons Attribution License, which permits unrestricted use, distribution, and reproduction in any medium, provided the original work is properly cited.

Porous gold films presented in this paper are formed by combining gold electroless deposition and polystyrene beads templating methods. This original approach allows the formation of conductive films ( $2 \times 10^6 \text{ } (\Omega \cdot \text{cm})^{-1}$ ) with tailored and interconnected porosity. The porous gold film was deposited up to  $1.2 \mu\text{m}$  on the silicon substrate without delamination. An original zirconia gel matrix containing gold nanoparticles deposited on the substrate acts both as an adhesion layer through the creation of covalent bonds and as a seed layer for the metallic gold film growth. Dip-coating parameters and gold electroless deposition kinetics have been optimized in order to create a three-dimensional network of 20 nm wide pores separated by 20 nm thick continuous gold layers. The resulting porous gold films were characterized by GIXRD, SEM, krypton adsorption-desorption, and 4-point probes method. The process is adaptable to different pore sizes and based on wet-chemistry. Consequently, the porous gold films presented in this paper can be used in a wide range of applications such as sensing, catalysis, optics, or electronics.

## 1. Introduction

The combination of the intrinsic properties of gold and of those of a porous material makes porous gold films (PGFs) an interesting material in many applications. These films are conductive [1] and chemically stable [2], present good wettability in electrolyte solutions [3], and exhibit a large specific surface area. Thus, porous gold films are increasingly used for electrochemical devices such as electric double-layer capacitors (EDLC) [4–7], Li-ion batteries [4, 8], or fuel cells [9, 10]. PGFs are also used as bio/chemical sensing electrode systems [2, 11–14], based on their nontoxic and biocompatible nature [12] and on the presence of active sites for biomaterials. In addition, these films present a high electrocatalytic activity, rapid mass transport, and a good thermal stability, which makes them suitable for (electro)catalytic applications [12, 15–17]. Finally, PGFs exhibit excellent properties concerning Surface-Enhanced Raman Spectroscopy (SERS),

Fluorescence, and Surface Plasmon Resonance (SPR), making them an attractive material for optical applications [18–20].

The pore size (from the nm to the mm scale), the pore modality (mono- or multimodal), and the presence of accessible and interconnected pores are essential parameters to be taken into account in relation to the targeted application. Some applications require small pore sizes (nm scale) in order to have a large specific surface area and thus increasing the active surface of the material. On the other hand, some other applications need large pore sizes ( $\mu\text{m}$  scale) to ensure a better mass transport [14, 21, 22]. Developing processes to fabricate porous gold films with tailorable properties is of undeniable interest.

PGFs are currently fabricated using mainly either a top-down dealloying method or a bottom-up templating method. The dealloying process consists in selectively etching the less-noble metal from a binary alloy (mostly  $\text{Ag}_x\text{Au}_{1-x}$ ) [11, 23].

The alloy is either directly bought from a supplier in the form of a metallic ribbon [6, 10, 18, 24] or fabricated using mainly cosputtering deposition [1, 5, 25, 26], electrodeposition [4, 9, 19], vapor/thermal deposition [22, 27, 28], or more rarely electroless deposition [15, 29]. The sample is then chemically or electrochemically selectively etched, leading to the formation of a porous framework of the remaining metal, composed of metallic ligaments and pore channels [23, 29]. Porous gold films fabricated by this method are tunable in thickness and pore size but present some weaknesses. First of all, they mostly require costly dedicated equipment and/or conductive substrate for the binary alloy fabrication (sputtering or electrodeposition methods). Then, the films are not systematically deposited on substrates, which could limit the scope of application. If deposited on substrates they require costly and constraining sputtering of Cr/Au or Ta/Au adhesion layers in order to prevent delamination of the film during etching [26]. Moreover, the dealloying process requires concentrated acid treatments to remove the less-noble metal from the alloy. The dealloyed films often contain some remains of this less-noble metal, degrading their catalytic properties [16]. Finally, PGFs contain pore sizes within the nm range, limited by the size of the less-noble metal aggregates composing the alloy. The templating method, on the other hand, is a simple and cost-effective way to create porous gold films of controlled pore sizes (from nm to  $\mu\text{m}$  scale) [17, 30]. This technique allows the formation of a porous film of a controlled thickness by a totally wet approach. It is based on the deposition of an assembly of spherical particles (template), followed by the filling of the interstitial spaces between the spheres by the material of our choice (which is gold here). The final step consists in removing the template (either by calcination or by dissolution (solvent or acid)), revealing the porous structure of the filling material. Various types of templates exist, allowing us to choose the pore sizes desired (from the nm to the mm scale): colloidal crystals (e.g., silica spheres) [31, 32], polymers (e.g., polystyrene beads) [15, 33–35], surfactants [13, 14, 36], hydrogen [21, 37], or biomaterials [38, 39]. Filling the interstices between the spheres is mainly achieved by electrodeposition method [13, 21, 32, 34, 37], which consists in an electrochemical growth of a selected metal on a conductive substrate. A variant of electrodeposition is the electroless deposition technique. It allows depositing metallic films, while avoiding the constraining use of a conductive substrate. Only a few papers [14, 31, 33, 35] are reporting the combined use of electroless deposition method and templating technique to create porous gold films so far.

In this paper, we present an original totally wet-chemistry approach to fabricate gold films with controlled and interconnected porosity using alternate of templating and electroless deposition processes. PS beads have been used here as template, since they allow the tailoring of the pores and are highly monodisperse, easily autoassembled, and easily removable. Gold electroless deposition method has been chosen to embed the PS beads in this conductive metal as we are able to control the thickness of the deposited film. An original Au/ZrO<sub>2</sub> film is deposited on a silicon substrate. It is composed of a zirconia (ZrO<sub>2</sub>) gel matrix embedding

gold nanoparticles. The inorganic matrix anchors the gold nanoparticles to the substrate. It creates Si-O-Zr bridges with the functionalized silicon substrate surface as a replacement for organic linkers previously reported in the literature [40]. The gold nanoparticles act as growth seeds for the growth of the gold film. Electrical, chemical, and structural properties of such films have been investigated during this work.

## 2. Materials and Methods

All the materials were purchased from Sigma-Aldrich (France). To avoid any purification, deoxygenated milli-Q water (18.2 M $\Omega$ -cm) was used in all the preparations. All reactions were carried out under argon atmosphere. All the glassware dedicated to the gold nanoparticles embedded in zirconia matrix synthesis is washed with aqua regia prior to use.  $3 \times 2 \text{ cm}^2$  P-doped (5–10  $\Omega$ ) pieces of Si (100) wafers are used as substrates. First, they are thermally oxidized (110°C) creating a 200 nm thick SiO<sub>2</sub> layer.

*2.1. Preparation of the Au/ZrO<sub>2</sub> Sol.* The gold nanoparticles embedded in zirconia matrix (Au/ZrO<sub>2</sub>) were synthesized according to a previous work [41]. A solution containing equimolar (0.011 mol) amount of zirconium(IV) propoxide solution (Zr(OC<sub>3</sub>H<sub>7</sub>)<sub>4</sub>, 70 wt.% in 1-propanol) and acetylacetone (CH<sub>3</sub>COCH<sub>2</sub>COCH<sub>3</sub>,  $\geq 99\%$ ) was prepared into a 250 mL three-necked flask. The mixture was stirred for 30 minutes under air to ensure the homogeneity of the solution and to allow the protection of the zirconium alkoxide by chelation with a  $\beta$ -diketone (acetylacetone) in order to slow down hydrolysis reaction [42]. 1 mM Gold(III) chloride trihydrate (HAuCl<sub>4</sub>·3H<sub>2</sub>O,  $\geq 99.9\%$  trace metal basis) in 2-propanol ((CH<sub>3</sub>)<sub>2</sub>CHOH absolute, over molecular sieve,  $\geq 99.5\%$ ) gold solution and 13 mM of sodium borohydride (NaBH<sub>4</sub>,  $\geq 96\%$ ) in a mixture of water/2-propanol reducing agent solution were prepared on a side. The gold solution was added into the flask, and after a few minutes of stirring, the reducing agent solution was added under vigorous stirring. The yellowish solution takes instantly a blood-red colour. The stirring of the solution was carried on during 3 hours under air. Hexane (CH<sub>3</sub>(CH<sub>2</sub>)<sub>4</sub>CH<sub>3</sub> anhydrous,  $\geq 95\%$ ) was added to the Au/ZrO<sub>2</sub> sol and was centrifuged at 2500 rpm during 30 min at 0°C. The upper organic phase was thrown out and the Au/ZrO<sub>2</sub> solid phase redispersed in ethanol (CH<sub>3</sub>CH<sub>2</sub>OH absolute,  $\geq 99.8\%$ ). DLS measurements and TEM analyses showed that the gold nanoparticles formed are approximately 5 nm in diameter.

*2.2. Preparation of the PS Beads.* The PS beads were synthesized by a modified microemulsion polymerization method [43]. 1 g of sodium dodecyl sulfate (CH<sub>3</sub>(CH<sub>2</sub>)<sub>11</sub>OSO<sub>3</sub>Na,  $\geq 99.0\%$ ) is dissolved in 90 mL of water in a 250 mL three-necked flask topped with a reflux condenser and connected to argon. The temperature is raised to 80°C and 0.15 g of potassium persulfate (K<sub>2</sub>S<sub>2</sub>O<sub>8</sub>,  $\geq 99.0\%$ ) dissolved in 10 mL of water is added to the reaction batch. A mixture of 1.5 g of styrene (C<sub>6</sub>H<sub>5</sub>CH=CH<sub>2</sub>,  $\geq 99\%$ ) and 0.1 g of 1-butanol (CH<sub>3</sub>(CH<sub>2</sub>)<sub>3</sub>OH,  $\geq 99.4\%$ ) is added drop by drop under mild

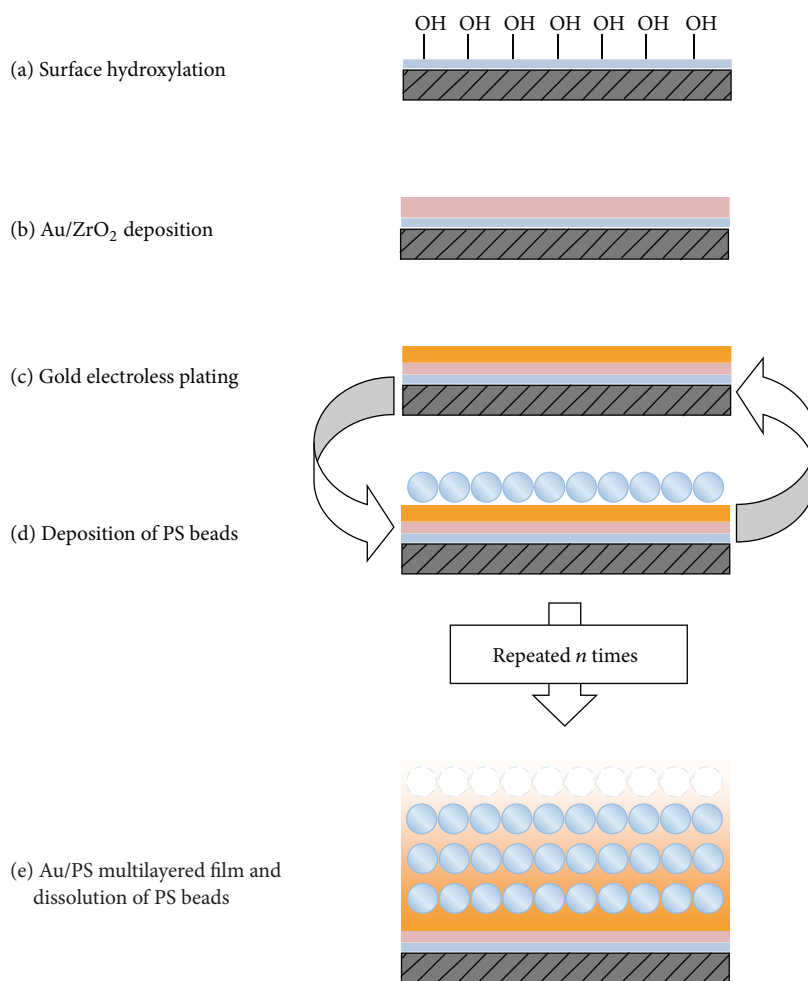


FIGURE 1: Schematic diagram of the porous gold film fabrication.

agitation (200 rpm) for 30 min. Then, 3.5 g of styrene is added all at once to the batch and is stirred for 1 hour. The solution is heated at 85°C for 1 hour before being cooled down to room temperature (RT). The bluish solution contains PS beads with a diameter of about 20 nm (determined by DLS measurements).

**2.3. Fabrication of the Porous Gold Film.** The fabrication process of such a film includes five steps. These steps are presented in Figure 1 and will be detailed in the following subsections.

**2.3.1. Surface Hydroxylation.** The oxidized silicon substrate is cleaned by soaking in a Piranha solution during 2 hours at RT followed by the immersion in a boiling solution containing hydrogen peroxide solution (H<sub>2</sub>O<sub>2</sub>, 30 wt.% in H<sub>2</sub>O) and a few drops of ammonium hydroxide solution (NH<sub>4</sub>OH, 28–30% NH<sub>3</sub> basis). This cleaning process allows the creation of hydroxyl groups on the surface of the silicon substrate (Figure 1(a)). The substrates can be stored in mQ-water until used (up to a month) [44].

**2.3.2. Au/ZrO<sub>2</sub> Seed Layer Deposition.** The seed layer, avoiding delamination of the film and containing gold nanoparticles, is deposited by dip-coating technique. The functionalized substrate is rinsed with mQ-water and dried vertically in air at RT. It is immersed in the Au/ZrO<sub>2</sub> stock solution during 10 s and withdrawn at a constant speed of 100 mm·min<sup>-1</sup>. The substrates are dried vertically in air at RT for 2 hours (Figure 1(b)). The Au/ZrO<sub>2</sub> film, after the deposition and drying processes, has a bluish tint and is about 300 nm thick.

**2.3.3. Gold Electroless Plating.** The Au/ZrO<sub>2</sub>-coated silicon substrate is immersed in an aqueous solution containing 4 mL of the ionic gold precursor (HAuCl<sub>4</sub>, 0.1 wt.%) and 0.25 mL of hydrogen peroxide solution (H<sub>2</sub>O<sub>2</sub>, 30 wt.% in H<sub>2</sub>O) for 2 minutes while agitated continuously. The Au/ZrO<sub>2</sub> film takes progressively a violet and then black colour. Finally, a goldish tint appears on the film (Figure 1(c)).

**2.3.4. Deposition of the PS Beads Template.** The PS beads were assembled on the gold-coated substrate by dip-coating method. The sample was immersed in the PS stock solution

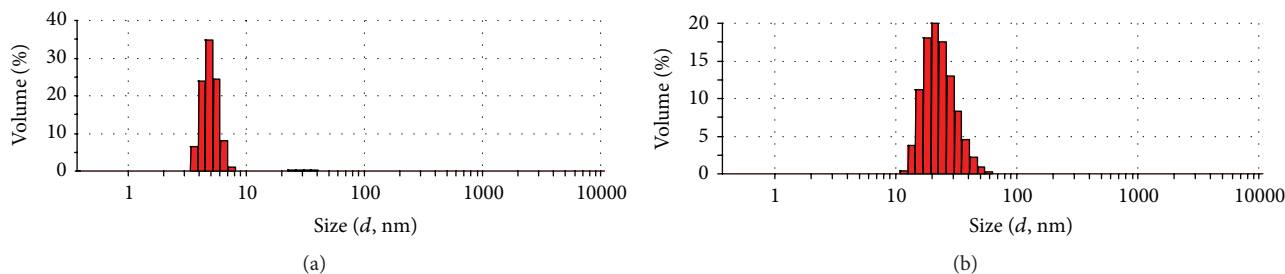


FIGURE 2: Size distribution by volume of (a) diluted ethanolic solution of Au/ZrO<sub>2</sub> and (b) diluted aqueous solution of PS beads.

for 10 min and withdrawn at a constant speed of 2 mm·min<sup>-1</sup>. It is dried vertically in air at RT overnight [45]. The film deposited is opalescent and colourless (Figure 1(d)).

**2.3.5. Au/PS Multilayered Film and Dissolution of PS Beads.** The gold electroless plating and the deposition of the PS beads template steps were reproduced  $n$  times to form a multilayered film. The sample is finally immersed in toluene (C<sub>6</sub>H<sub>5</sub>CH<sub>3</sub>, ≥95%) for 1 hour to remove the PS beads and create consequently porosity within the film (Figure 1(e)).

### 3. Results and Discussion

**3.1. DLS Analysis.** To determine the particle size and size distribution of the gold nanoparticles, Dynamic Light Scattering (DLS) analyses were performed using a Malvern Zetasizer Nano-S90 on diluted samples. The size distribution is expressed by volume, and the particle size is calculated as the average value of three successive measurements. The results represented below indicate that the ethanolic solution of Au/ZrO<sub>2</sub> contains gold nanoparticles with a mean diameter of 4.9 nm. The distribution is comprised between 2 nm and 8 nm with a maximum centered on 4.9 nm (Figure 2(a)). The solution is considered to be monodisperse in size since the peak is narrow. The same analyses have been conducted on a diluted aqueous solution of PS beads. The sample is monodisperse in size with a mean diameter of the bead equal to 26.1 nm (Figure 2(b)).

Polystyrene beads used as templates present the advantages of being tunable in size [46] (from 20 nm [43] to 400 nm [47]) and easily removable by soaking in toluene. They allow choosing the size of the pores created in our material according to the considered application while preserving their internal structure. The withdrawal speed chosen allows the formation of an assembly of polystyrene beads on the surface of the gold-coated sample. It is indeed observable on the inset of Figure 5(a) as the porous network is well-organized within the final material.

**3.2. TEM Analysis.** High Resolution Transmission Electron Microscopy (HRTEM) was carried out using a TOPCON EM002B TEM, operating at 200 kV. The TEM analysis performed on a diluted sample of Au/ZrO<sub>2</sub> confirms the size of the gold nanoparticles contained in the ethanolic solution (Figure 3). It shows as well that spherical gold nanoparticles

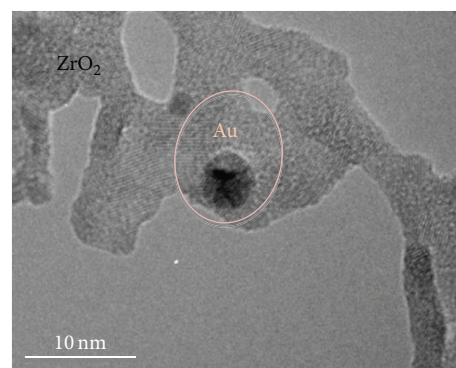
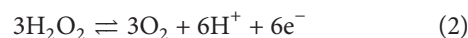
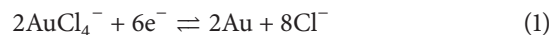


FIGURE 3: TEM picture of a gold nanoparticle embedded in zirconia matrix.

are indeed embedded in a zirconia matrix (light-grey in the picture).

**3.3. Formation Mechanism of the Gold Film by Electroless Plating.** The deposition of the Au/ZrO<sub>2</sub> seed layer by dip-coating technique allows us to control the thickness and the mechanical properties of the film. The withdrawal speed and the drying process are the main parameters to control in order to do this. The withdrawal speed chosen (100 mm·min<sup>-1</sup>) allowed us to obtain the appropriate thickness of the film (300 nm). The film is uniformly deposited and continuous. The drying process (2 hours in air at RT) avoids the presence of cracks in the film and the delamination of the film. Gold nanoparticles are immobilized onto the silicon substrate thanks to the creation of strong Si-O-Zr bridges between the hydroxylated silica surface and the ZrO<sub>2</sub> matrix embedding these nanoparticles [42]. The H<sub>2</sub>O<sub>2</sub> introduced during the electroless plating process acts as a reducing agent. It reduces the Au<sup>3+</sup> from the ionic gold precursor (HAuCl<sub>4</sub>) into Au<sup>0</sup> (reaction (3)) as explained in previous work [40]:



Gold atoms (Au<sup>0</sup>) reduced by the H<sub>2</sub>O<sub>2</sub> in the gold plating bath contribute to the growth of the gold nanoparticles immobilized onto the substrate. These nanoparticles act

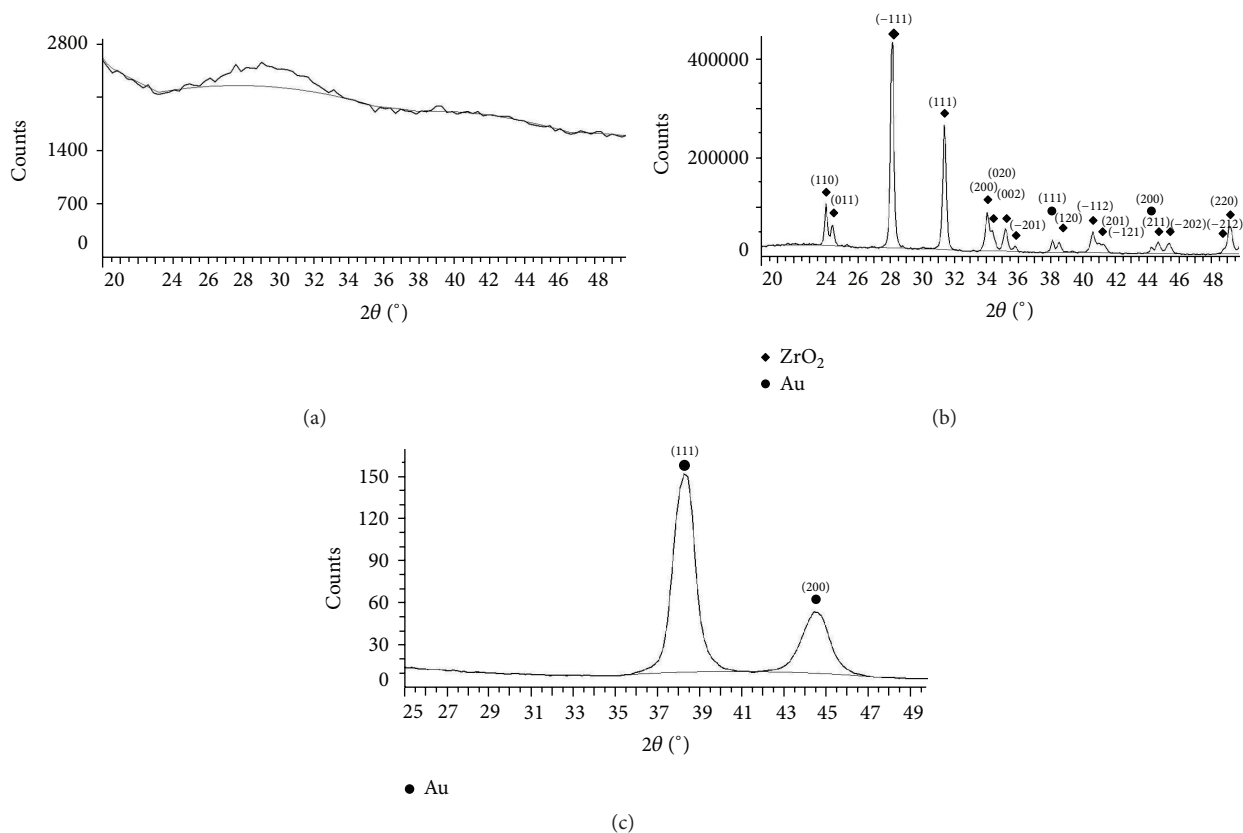


FIGURE 4: GIXRD diagrams of (a) amorphous Au/ZrO<sub>2</sub> at RT, (b) crystallized Au/ZrO<sub>2</sub> treated thermally at 1200°C, and (c) Au/PS 10-layered film.

as nucleation sites. Particles growth is followed by their coalescence to form a continuous metallic gold film. The nucleation/growth/coalescence process is visually noticeable as it induces a change of colour on the gold film [48]. The reaction kinetics has been optimized in order to obtain continuous gold films. The key parameters are the gold precursor concentration and the  $V_{\text{HAuCl}_4}/V_{\text{H}_2\text{O}_2}$  ratio. The thickness of the gold film mostly depends on the reaction time [49, 50]. We have set this parameter to 2 min, in order to obtain continuous conductive metallic films of controlled thickness (20 nm) between each PS assembly layers. Similar results have been obtained elsewhere [40]. In this work, Hu et al. employed a multistep process to ensure adherence of gold nanoparticles to the substrate. Their process consisted in functionalizing the glass surface with organic linkers (APTMS), followed by the use of citrate-stabilized gold nanoparticles as nucleation sites. The functionalizing step lasted 16 hours under inert atmosphere, followed by the immersion during 6 hours in the gold-citrate solution. The alternative process we are presenting is a time-efficient one-step method based on a sol-gel process.

**3.4. XRD Characterization.** The Au/ZrO<sub>2</sub> seed layer was analyzed by Grazing Incidence X-Ray Diffraction (GIXRD) (Figure 4(a)). The diagrams were recorded with a Bruker AXS

D8 diffractometer using a Cu K<sub>α</sub> radiation source (40 kV and 40 mA) and equipped with a Lynxeye XE 1D detector. Experiments were carried out between  $2\theta = 25^\circ$  and  $50^\circ$ . The angle of incidence was fixed at  $2^\circ$ . The presence of a large peak on the diagram between  $2\theta = 24^\circ$  and  $33^\circ$  is characteristic of the amorphous phase of the zirconia. This observation is consistent with the fact that ZrO<sub>2</sub> presents a crystal structure only at high temperature [51] and remains amorphous at RT. The low-intensity peak situated at  $2\theta = 38.65^\circ$  could be attributed to the cubic gold crystal structure. In order to confirm the presence of gold nanoparticles embedded in the ZrO<sub>2</sub> matrix, the film was treated at 1200°C under air (Figure 4(b)). One can observe the characteristic peaks of the monoclinic ZrO<sub>2</sub> crystal structure at  $2\theta = 24.00^\circ$ ;  $24.36^\circ$ ;  $28.00^\circ$ ;  $31.46^\circ$ ;  $34.14^\circ$ ;  $34.39^\circ$ ;  $35.28^\circ$ ;  $35.87^\circ$ ;  $38.54^\circ$ ;  $38.80^\circ$ ;  $39.41^\circ$ ;  $39.95^\circ$ ;  $40.70^\circ$ ;  $41.13^\circ$ ;  $41.37^\circ$ ;  $44.80^\circ$ ;  $45.49^\circ$ ;  $48.90^\circ$ ; and  $49.24^\circ$  according to the ICDD card reference 00-037-1484. The presence of gold particles is also evidenced by the diffraction peaks at  $2\theta = 38.18^\circ$  and  $2\theta = 44.39^\circ$  (ICDD card reference 00-004-0784). No additional phase is observed. The GIXRD diagram of the Au/PS 10-layered film (Figure 4(c)) exhibits diffraction peaks at  $2\theta = 38.18^\circ$  and  $2\theta = 44.39^\circ$  corresponding to the (111) and (200) lattice planes of the cubic gold crystal structure (ICDD card reference 00-004-0784). The relative intensity of the diffraction peaks shows that there

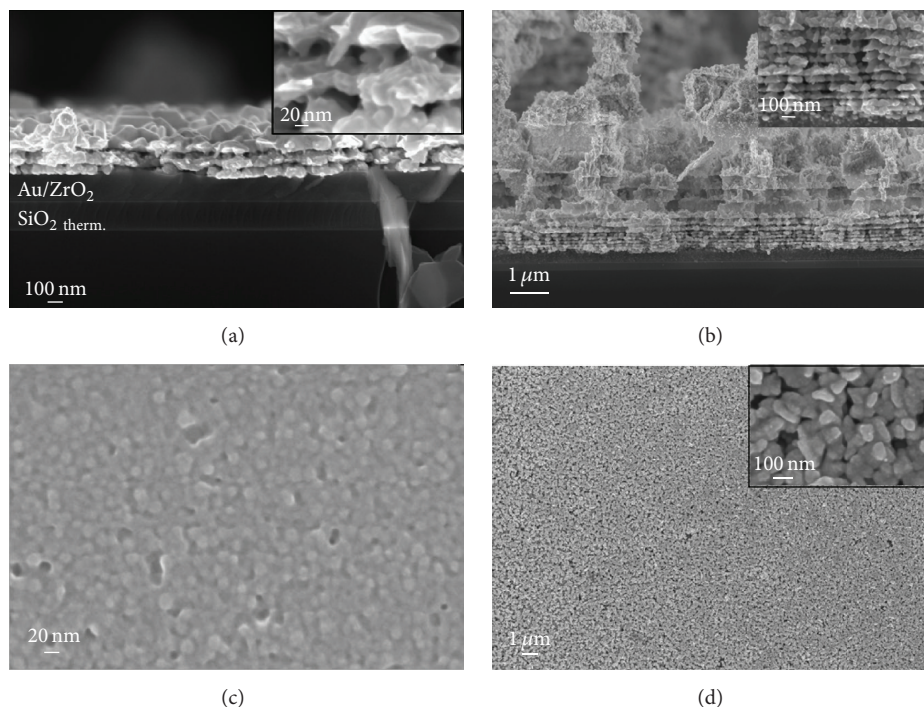


FIGURE 5: SEM micrographs of (a) PGF after two PS layers, (b) PGF after twenty PS layers, (c) PS beads assembly, and (d) top view of the ten PS layers film.

is no preferential orientation during the formation of the gold film onto the silicon substrate. No additional crystal phase is observed.

**3.5. SEM Analysis.** Scanning Electron Microscopy (SEM) analyses were carried out using a Zeiss Ultra 55. Images of the porous gold films at different steps of the deposition process are shown in Figure 5. The different layers deposited during the process can be seen in Figure 5(a). The lower 200 nm thick layer corresponds to the thermally oxidized silicon ( $\text{SiO}_2_{\text{therm.}}$ ), coated with the 300 nm thick seed layer ( $\text{Au/ZrO}_2$ ) on top of which we find the PGF. This porous film is composed of two layers of PS beads assemblies coated with 20 nm thick gold thin films. The inset of Figure 5(a) (zoom on the porous film) shows the porosity created within the film. The hole size fits the diameter of the PS beads obtained by DLS measurements. The deposition of ten successive PS beads assemblies/gold thin film is represented in the inset of Figure 5(b). No change in the structure of the overall film was noticed. The pore size and the gold thin film thicknesses stayed unchanged during all the process. At this point, the porous gold film reaches a thickness of about  $1.2 \mu\text{m}$ , while presenting no delamination. In order to increase the thickness of the porous gold film, the deposition of 10 additional Au/PS layers was experimented. The first 10 Au/PS layers are uniformly deposited. However, the deposition of the last 10 Au/PS layers revealed the presence of large (about  $3.6 \mu\text{m}$  thick) blocks of stacked alternative Au/PS layers (Figure 5(b)). This behaviour may be related to internal mechanical stress within the material. Experimentally, we observed that the

10 upper layers are thicker and thicker as we carry on with the PS beads deposition/electroless plating steps. We can deduce from these observations that we have reached a limit in the PGF growth by electroless deposition after 10 successive Au/PS layers. The same result was obtained after each experiment conducted, showing the reproducibility of the structure beyond the critical point. A SEM picture of the PS beads assembly is presented in Figure 5(c). We can notice that the PS beads are uniformly deposited on the gold-coated substrate. Figure 5(d) shows the surface state of the 10-layered film and a zoom on this surface state in the inset. The final layer is homogeneous, continuous, and crackless and contains low porosity. The gold layers between porous layers are connected altogether and are about 20 nm thick. Such a thickness allows the film to be continuous and conductive. All the pores of the material are considered to be interconnected since there are no remaining PS beads after toluene treatment, even the ones situated close to the substrate.

**3.6. AFM Analysis.** Atomic-Force Microscopy (AFM) analyses were performed using a Bruker Edge atomic force microscope. Figures 6(a) and 6(b) show the 2D and 3D  $1 \mu\text{m} \times 1 \mu\text{m}$  images, respectively, of the PS beads assembly. From these figures, we can observe that the PS beads are spherical and form a continuous film. The homogeneity of contrast highlights the fact that the PS beads composing the film are on the same level. The absence of volume effect, as the layer exhibits a high density, is confirmed by the extracted profile (based on the white line from Figure 6(a)) (Figure 6(c)). The RMS roughness calculated (from Figure 6(a)) is 6.64 nm,

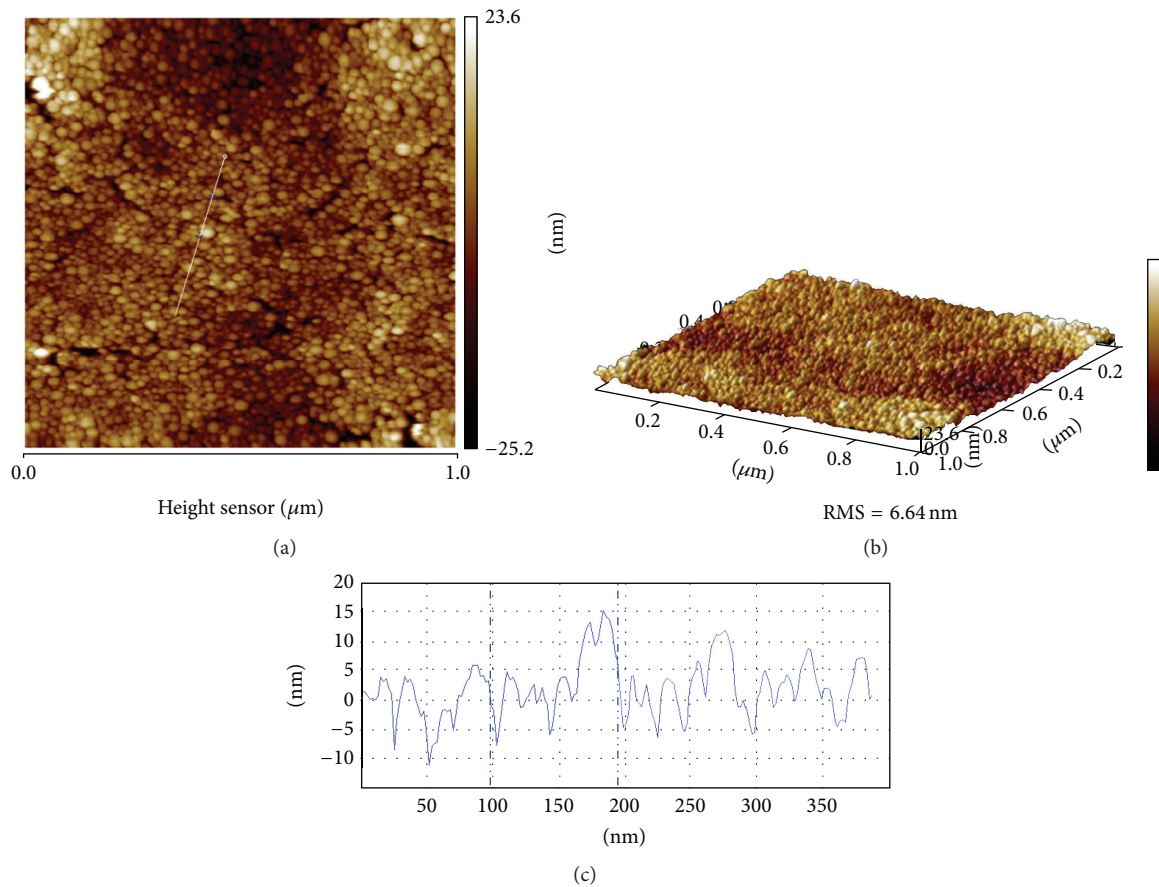


FIGURE 6: (a) AFM 2D  $1\ \mu\text{m} \times 1\ \mu\text{m}$  image, (b) AFM 3D  $1\ \mu\text{m} \times 1\ \mu\text{m}$  image, and (c) extracted line profiles from the  $1\ \mu\text{m} \times 1\ \mu\text{m}$  image.

which is low. This result shows that the distribution of the PS beads is homogeneous. The morphology of the PS beads assembly studied by AFM confirmed the observations previously made by SEM (Figure 5(c)).

**3.7. Krypton Adsorption-Desorption Isotherms.** The Brunauer-Emmett-Teller (BET) specific surface areas ( $S_{\text{BET}}$ ) were determined from krypton adsorption-desorption at 77.35 K using a Bel Japan Belsorp Max Instrument. Prior to the experiments, the samples were outgassed at RT for several hours under secondary vacuum. The PGFs exhibit a  $S_{\text{BET}}$  of  $4\ \text{m}^2\cdot\text{g}^{-1}$ , which is considered to be high for such a material [1, 37]. However, we were not able to determine an accurate pore size as the sample mass characterized was too low (3.3 mg compared to the few hundred milligrams commonly required).

**3.8. Electrical Characterization.** The electrical conductivity of a  $1\ \mu\text{m}$  thick porous gold thin film has been measured using a Jandel RM2 four-point probes system (Figure 7). The probes exhibit a 1.0 mm spacing and a  $125\ \mu\text{m}$  tip radius. The value of the conductivity has been assessed to be  $2 \pm 0.2 \times 10^6\ (\Omega\cdot\text{cm})^{-1}$ , which is about 20 times less than dense gold. Similar results of PGFs conductivity have been found in the literature. Maarroof et al. stated that the electrical conductivity

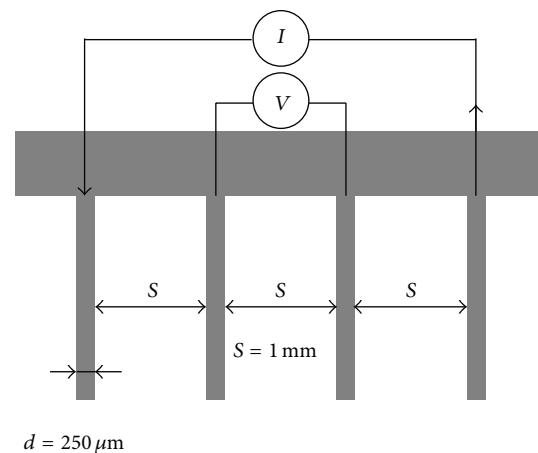


FIGURE 7: Drawing of a four-point probes system.

of porous gold films is in the range  $1 \times 10^5 - 3 \times 10^6\ (\Omega\cdot\text{m})^{-1}$  [1]. The decrease in the conductivity value is due to the presence of pores in the material and hence the presence of air, which is an insulating medium. As a comparison, the carbon exhibits an electrical conductivity of  $6.1 \times 10^4\ (\Omega\cdot\text{cm})^{-1}$ .

## 4. Conclusion

The fabrication of porous gold films by an original “bottom-up” approach through combined PS beads templating and gold electroless deposition methods has been achieved. All the techniques employed in the fabrication of the PGFs are totally wet-chemistry processes. The deposition of an original sol-gel-based Au/ZrO<sub>2</sub> adhesion/seed layer onto a silicon substrate has been presented in this paper. Dip-coating and drying parameters have been optimized in order to deposit a uniform, continuous, and crackless film. The ZrO<sub>2</sub> matrix anchors the Au nanoparticles to the substrate and prevents the delamination of the final material (PGF) up to a thickness of 1.2 μm. Simultaneously, the gold nanoparticles embedded in the ZrO<sub>2</sub> matrix act as growth seeds for the following gold electroless deposition. An autoassembly of PS beads (template) has been deposited onto the Au/ZrO<sub>2</sub> film by dip-coating technique. Gold electroless deposition kinetics parameters have been optimized in order to obtain continuous conductive gold thin films of controlled thickness between PS layers. The process described is conducted several times and the PS layers are removed by dissolution. SEM pictures showed a three-dimensional network of interconnected and size-tailored 20 nm wide pores separated by 20 nm thick continuous gold layers. Krypton adsorption-desorption isotherms demonstrated a specific surface area ( $S_{\text{BET}}$ ) of about 4 m<sup>2</sup>·g<sup>-1</sup>. The fabrication process described in this paper allows the deposition of a material exhibiting at the same time a good conductivity value ( $2 \times 10^6$  (Ω·cm)<sup>-1</sup>) and well-defined 20 nm wide pores. Such material is a promising candidate for electric double-layer capacitor electrodes or bio-/chemical sensors, for instance.

## Disclosure

Katarzyna Raulin is now working at Ethera, 7 Parvis Louis Néel, CS 20050, 38040 Grenoble Cedex 9.

## Competing Interests

The authors declare that they have no competing interests.

## Acknowledgments

This work was supported by the ERDF (European Regional Development Fund), by the Nord-Pas-de-Calais Region (France) through the CIA Project (2009–2013), and by the ANR through the INPACT Project (2014–2017) and the AMPEROR Project (2014–2017). This work was also partly supported by the Equipex FLUX through the Programme Investissements d’Avenir.

## References

- [1] A. I. Maarouf, M. B. Cortie, A. Gentle, and G. B. Smith, “Mesoporous gold sponge as a prototype ‘metamaterial,’” *Physica B: Condensed Matter*, vol. 394, no. 2, pp. 167–170, 2007.
- [2] D. Van Noort and C.-F. Mandenius, “Porous gold surfaces for biosensor applications,” *Biosensors and Bioelectronics*, vol. 15, no. 3–4, pp. 203–209, 2000.
- [3] P. S. Liu and G. F. Chen, *Porous Materials Processing and Applications*, Elsevier Science Butterworth-Heinemann, Oxford, UK, 2014.
- [4] C. Mele, M. Catalano, A. Taurino, and B. Bozzini, “Electrochemical fabrication of nanoporous gold-supported manganese oxide nanowires based on electrodeposition from eutectic urea/choline chloride ionic liquid,” *Electrochimica Acta*, vol. 87, pp. 918–924, 2013.
- [5] Z. Zeng, X. Long, H. Zhou, E. Guo, X. Wang, and Z. Hu, “On-chip interdigitated supercapacitor based on nanoporous gold/manganese oxide nanowires hybrid electrode,” *Electrochimica Acta*, vol. 163, pp. 107–115, 2015.
- [6] X. Lang, A. Hirata, T. Fujita, and M. Chen, “Nanoporous metal/oxide hybrid electrodes for electrochemical supercapacitors,” *Nature Nanotechnology*, vol. 6, no. 4, pp. 232–236, 2011.
- [7] T. Fujita, H. Okada, K. Koyama, K. Watanabe, S. Maekawa, and M. W. Chen, “Unusually small electrical resistance of three-dimensional nanoporous gold in external magnetic fields,” *Physical Review Letters*, vol. 101, no. 16, Article ID 166601, 2008.
- [8] Y. Yu, L. Gu, X. Lang et al., “Li storage in 3D nanoporous au-supported nanocrystalline tin,” *Advanced Materials*, vol. 23, no. 21, pp. 2443–2447, 2011.
- [9] L. C. Nagle and J. F. Rohan, “Nanoporous gold anode catalyst for direct borohydride fuel cell,” *International Journal of Hydrogen Energy*, vol. 36, no. 16, pp. 10319–10326, 2011.
- [10] X. B. Ge, R. Y. Wang, P. P. Liu, and Y. Ding, “Platinum-decorated nanoporous gold leaf for methanol electrooxidation,” *Chemistry of Materials*, vol. 19, no. 24, pp. 5827–5829, 2007.
- [11] J. Erlebacher, M. J. Aziz, A. Karma, N. Dimitrov, and K. Sieradzki, “Evolution of nanoporosity in dealloying,” *Nature*, vol. 410, no. 6827, pp. 450–453, 2001.
- [12] Y. Xia, W. Huang, J. Zheng, Z. Niu, and Z. Li, “Nonenzymatic amperometric response of glucose on a nanoporous gold film electrode fabricated by a rapid and simple electrochemical method,” *Biosensors and Bioelectronics*, vol. 26, no. 8, pp. 3555–3561, 2011.
- [13] C. S. Oh, H. Kim, S. Rengaraj, and Y. Kim, “In situ detection and removal of metal ion by porous gold electrode,” *Microporous and Mesoporous Materials*, vol. 147, no. 1, pp. 1–4, 2012.
- [14] H. Kim, Y. Kim, J. B. Joo, J. W. Ko, and J. Yi, “Preparation of coral-like porous gold for metal ion detection,” *Microporous and Mesoporous Materials*, vol. 122, no. 1–3, pp. 283–287, 2009.
- [15] G. W. Nyce, J. R. Hayes, A. V. Hamza, and J. H. Satcher, “Synthesis and characterization of hierarchical porous gold materials,” *Chemistry of Materials*, vol. 19, no. 3, pp. 344–346, 2007.
- [16] A. Wittstock, V. Zielasek, J. Biener, C. M. Friend, and M. Bäumer, “Nanoporous gold catalysts for selective gas-phase oxidative coupling of methanol at low temperature,” *Science*, vol. 327, no. 5963, pp. 319–322, 2010.
- [17] Y. Deng, W. Huang, X. Chen, and Z. Li, “Facile fabrication of nanoporous gold film electrodes,” *Electrochemistry Communications*, vol. 10, no. 5, pp. 810–813, 2008.
- [18] S. O. Kucheyev, J. R. Hayes, J. Biener, T. Huser, C. E. Talley, and A. V. Hamza, “Surface-enhanced Raman scattering on nanoporous Au,” *Applied Physics Letters*, vol. 89, no. 5, Article ID 053102, 2006.
- [19] H.-O. Lee, E.-M. Kim, H. Yu, J.-S. Jung, and W.-S. Chae, “Advanced porous gold nanofibers for highly efficient and stable molecular sensing platforms,” *Nanotechnology*, vol. 20, no. 32, Article ID 325604, 2009.

- [20] S. Y. Gao, H. J. Zhang, X. M. Wang et al., "Unique gold sponges: biopolymer-assisted hydrothermal synthesis and potential application as surface-enhanced Raman scattering substrates," *Nanotechnology*, vol. 16, no. 11, pp. 2530–2535, 2005.
- [21] S. Cherevko and C.-H. Chung, "Direct electrodeposition of nanoporous gold with controlled multimodal pore size distribution," *Electrochemistry Communications*, vol. 13, no. 1, pp. 16–19, 2011.
- [22] M. E. Cox and D. C. Dunand, "Bulk gold with hierarchical macro-, micro- and nano-porosity," *Materials Science and Engineering A*, vol. 528, no. 6, pp. 2401–2406, 2011.
- [23] A. J. Forty, "Corrosion micromorphology of noble metal alloys and depletion gilding," *Nature*, vol. 282, no. 5739, pp. 597–598, 1979.
- [24] Y. Ding and J. Erlebacher, "Nanoporous metals with controlled multimodal pore size distribution," *Journal of the American Chemical Society*, vol. 125, no. 26, pp. 7772–7773, 2003.
- [25] K. Wagner, S. R. Brankovic, N. Dimitrov, and K. J. Sieradzki, "Dealloying below the critical potential," *Journal of the Electrochemical Society*, vol. 144, no. 10, pp. 3545–3555, 1997.
- [26] Y. Sun, K. P. Kucera, S. A. Burger, and T. John Balk, "Microstructure, stability and thermomechanical behavior of crack-free thin films of nanoporous gold," *Scripta Materialia*, vol. 58, no. 11, pp. 1018–1021, 2008.
- [27] A. J. Forty and P. Durkin, "Micromorphological study of the dissolution of silver-gold alloys in nitric acid," *Philosophical Magazine A*, vol. 42, no. 3, pp. 295–318, 1980.
- [28] I. C. Oppenheim, D. J. Trevor, C. E. D. Chidsey, P. L. Trevor, and K. Sieradzki, "In situ scanning tunneling microscopy of corrosion of silver-gold alloys," *Science*, vol. 254, no. 5032, pp. 687–689, 1991.
- [29] T. Bryce C, S. Stephen A III, and E. P. Luther, "Nanoporous metal foams," *Angewandte Chemie—International Edition*, vol. 49, no. 27, pp. 4544–4565, 2010.
- [30] O. D. Velev and A. M. Lenhoff, "Colloidal crystals as templates for porous materials," *Current Opinion in Colloid & Interface Science*, vol. 5, no. 1-2, pp. 56–63, 2000.
- [31] P. Jiang, J. Cizeron, J. F. Bertone, and V. L. Colvin, "Preparation of macroporous metal films from colloidal crystals," *Journal of the American Chemical Society*, vol. 121, no. 34, pp. 7957–7958, 1999.
- [32] R. Szamocki, S. Reculosa, S. Ravaine, P. N. Bartlett, A. Kuhn, and R. Hempelmann, "Tailored mesostructuring and biofunctionalization of gold for increased electroactivity," *Angewandte Chemie—International Edition*, vol. 45, no. 8, pp. 1317–1321, 2006.
- [33] O. D. Velev, P. M. Tessier, A. M. Lenhoff, and E. W. Kaler, "A class of porous metallic nanostructures," *Nature*, vol. 401, no. 6753, p. 548, 1999.
- [34] Y. Bai, W. Yang, Y. Sun, and C. Sun, "Enzyme-free glucose sensor based on a three-dimensional gold film electrode," *Sensors and Actuators B: Chemical*, vol. 134, no. 2, pp. 471–476, 2008.
- [35] H. Kim and Y. Kim, "Preparation of nanoporous gold using PS bead, Ludox and nanoporous alumina as physical templates," *Current Applied Physics*, vol. 9, no. 1, pp. S88–S90, 2009.
- [36] H. Zhang, I. Hussain, M. Brust, and A. I. Cooper, "Emulsion-templated gold beads using gold nanoparticles as building blocks," *Advanced Materials*, vol. 16, no. 1, pp. 27–30, 2004.
- [37] H. Du Toit and M. Di Lorenzo, "Electrodeposited highly porous gold microelectrodes for the direct electrocatalytic oxidation of aqueous glucose," *Sensors and Actuators B: Chemical*, vol. 192, pp. 725–729, 2014.
- [38] R. Seshadri and F. C. Meldrum, "Bioskeletons as templates for ordered, macroporous structures," *Advanced Materials*, vol. 12, no. 15, pp. 1149–1151, 2000.
- [39] F. C. Meldrum and R. Seshadri, "Porous gold structures through templating by echinoid skeletal plates," *Chemical Communications*, no. 1, pp. 29–30, 2000.
- [40] J. Hu, W. Li, J. Chen, X. Zhang, and X. Zhao, "Novel plating solution for electroless deposition of gold film onto glass surface," *Surface & Coatings Technology*, vol. 202, no. 13, pp. 2922–2926, 2008.
- [41] A. Le Rouge, H. El Hamzaoui, B. Capoen et al., "Synthesis and nonlinear optical properties of zirconia-protected gold nanoparticles embedded in sol-gel derived silica glass," *Materials Research Express*, vol. 2, no. 5, Article ID 055009, 2015.
- [42] J. C. Debsikdar, "Transparent zirconia gel-monomolith from zirconium alkoxide," *Journal of Non-Crystalline Solids*, vol. 86, no. 1-2, pp. 231–240, 1986.
- [43] K. Liu and Z. Wang, "A novel method for preparing monodispersed polystyrene nanoparticles," *Frontiers of Chemistry in China*, vol. 2, no. 1, pp. 17–20, 2007.
- [44] T. Ung, L. M. Liz-Marzán, and P. Mulvaney, "Gold nanoparticle thin films," *Colloids and Surfaces A: Physicochemical and Engineering Aspects*, vol. 202, no. 2-3, pp. 119–126, 2002.
- [45] Y. Fu, Z. Jin, Z. Liu, and W. Li, "Preparation of ordered porous SnO<sub>2</sub> films by dip-drawing method with PS colloid crystal templates," *Journal of the European Ceramic Society*, vol. 27, no. 5, pp. 2223–2228, 2007.
- [46] J. Zhang, Z. Chen, Z. Wang, W. Zhang, and N. Ming, "Preparation of monodisperse polystyrene spheres in aqueous alcohol system," *Materials Letters*, vol. 57, no. 28, pp. 4466–4470, 2003.
- [47] Z. Liu, J. Ya, Y. Xin, J. Ma, and C. Zhou, "Assembly of polystyrene colloidal crystal templates by a dip-drawing method," *Journal of Crystal Growth*, vol. 297, no. 1, pp. 223–227, 2006.
- [48] G. W. Qin, J. Liu, T. Balaji et al., "A facile and template-free method to prepare mesoporous gold sponge and its pore size control," *The Journal of Physical Chemistry C*, vol. 112, no. 28, pp. 10352–10358, 2008.
- [49] L. A. Nagahara, T. Ohmori, K. Hashimoto, and A. Fujishima, "The influence of hydrofluoric acid concentration on electroless copper deposition onto silicon," *Journal of Electroanalytical Chemistry*, vol. 333, no. 1-2, pp. 363–369, 1992.
- [50] L. A. Nagahara, T. Ohmori, K. Hashimoto, and A. Fujishima, "Effects of HF solution in the electroless deposition process on silicon surfaces," *Journal of Vacuum Science & Technology A*, vol. 11, no. 4, pp. 763–767, 1993.
- [51] J. D. McCullough and K. N. Trueblood, "The crystal structure of baddeleyite (monoclinic ZrO<sub>2</sub>)," *Acta Crystallographica*, vol. 12, no. 7, pp. 507–511, 1959.

## Research Article

# Template Transfer Nanoimprint for Uniform Nanopores and Nanopoles

Jianjun Li,<sup>1</sup> Weiwei Zhang,<sup>1</sup> Yujun Song,<sup>1,2</sup> Weiting Yin,<sup>2</sup> and Tao Zhang<sup>2</sup>

<sup>1</sup>Center for Modern Physics Technology, Engineering Center for Weak Magnetic Detection Beijing, Department of Physics, School of Mathematics and Physics, University of Science and Technology Beijing, Beijing 100083, China

<sup>2</sup>School of Materials Science and Engineering, Beihang University, Beijing 100191, China

Correspondence should be addressed to Yujun Song; [songyj@ustb.edu.cn](mailto:songyj@ustb.edu.cn)

Received 11 November 2015; Revised 29 December 2015; Accepted 30 December 2015

Academic Editor: Mahaveer Kurkuri

Copyright © 2016 Jianjun Li et al. This is an open access article distributed under the Creative Commons Attribution License, which permits unrestricted use, distribution, and reproduction in any medium, provided the original work is properly cited.

A new methodology is developed for the fabrication of nanostructures on substrate based on anodized Al<sub>2</sub>O<sub>3</sub> (AAO) porous template transfer process. It includes (1) forming amorphous alloy, negative UV-resist resin (i.e., SU-8), or PMMA (polymethylmethacrylate) plate nanorod arrays by hot-press molding amorphous alloy, negative UV-resist resin (i.e., SU-8), or PMMA plate into the anodized Al<sub>2</sub>O<sub>3</sub> porous substrates; (2) removing AAO templates by chemical etching process after suitable posttreatment (annealing and/or irradiation) to improve the mechanical strength of the nanorod arrays; (3) reforming nanopore films by hot-embossing the nanorod arrays into a thin layer of polymer film on substrates (e.g., silica); (4) cleaning the bottom residues in pores of the films by oxygen plasmon. The results indicate that the diameters of amorphous alloy (or negative UV-resist resin or PMMA) nanorod arrays can be ranged from 32 nm to 200 nm. The diameters of the imprinted ILR-1050 photoresist nanopores are about 94.5 ± 12.2 nm and the diameters of the imprinted or SU-8 resin on glass slides nanopores are about 207 ± 26.4 nm, which inherit the diameters of AAO templates. This methodology provides a general method to fabricate nanorods arrays and/or thin nanopore films by template transfer nanoimprint process.

## 1. Introduction

Nanostructural materials with defined size (from 1 nm to 1000 nm), shapes (e.g., triangle, square, or pores), and structures (e.g., monolayer, multilayers, and hierarchical arrays) have shown unique properties for advanced applications [1–4]. For instance, the ordered Ag nanopole arrays on Si wafer preserve surface-enhanced Raman scattering, which can be used for ultrasensitive bio/chemical sensing [5]. The surface-confined Ag NPs (nanoparticles) show distinct blue shift in the UV-Vis absorption [2]. Periodic nanoporous films constructed by multilayered Ag/CoFeB/Ag structures have enhanced magneto-optical effects [6]. Controlled fabrication of nanostructural materials at large scale is the base for their applications. For this goal, lots of methods have been developed, such as nanoimprint, template fabrication, lithography using electron beam, ion beam, X-ray beam, and laser beam. Among them, nanoimprint is powerful due to its large-scale ability at low cost.

The success of nanoimprint critically depends on the fabrication of robust and durable master molds and/or the development of economical fabrication technologies for these molds or direct imprinting [7–11]. Even though the conventional fabrication methods including electron, ion, X-ray, laser-beam or optical lithography can be used to fabricate the master molds besides directly conducting nanoimprint for some desired nanostructures, they are limited by either their feature sizes or patterned area scales [12–16]. Most of the current polymer master molds are not so strong and durable for increased repeating times and crystalline metal master molds are limited by their grain sizes [17, 18]. Silicon or quartz based molds can retain their high strength over a wide temperature range and can be lithographically patterned. However, they are brittle and have limited longevity [7]. Recently, template-assisted lithography has been further developed for large-scale fabrication of defined nanostructures at low cost. Particularly, anodized porous alumina makes it possible to prepare porous master molds with areas as large as 28 × 45 cm<sup>2</sup>

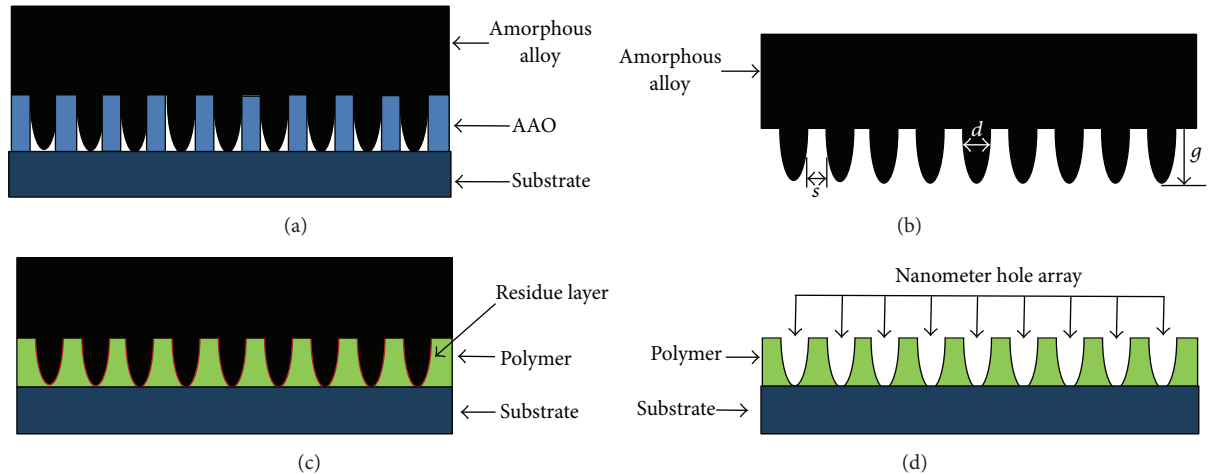


FIGURE 1: Scheme of the template transfer imprinting process for the preparation of nanopore structures. Forming amorphous alloy (or PMMA) nanorod arrays by hot-press molding amorphous alloy (or PMMA) into AAO porous substrates (a); removing AAO templates by chemical etching process (b); reforming nanopore films by hot-embossing the nanorod arrays into polymer film on substrates (c); cleaning the bottom residues in pores of the films by oxygen plasmon (d).

and feature sizes as small as 13 nm (products brochure of Synkera Technologies Inc.). However, most of the templates are disposable and the nanoimprint process in which we use the master molds made of traditional materials does not improve replicability, which significantly affect the stability and reliability of the final products.

It is well-known that amorphous metals and thermal-setting polymers are intrinsically free from grain size limitations and they are robust enough [8, 19–23]. Furthermore, amorphous metals present superior mechanical properties and some thermal-plastic polymers can become thermal-setting by posttreatment at high temperature and/or irradiation (i.e., UV photoresist) after they form the desired patterns [1–4, 8]. In this paper, a new method termed as template transfer nanoimprint is developed for the fabrication of nanostructures on substrate based on AAO template transfer process in which a kind of amorphous metal alloy (i.e., Pt-based amorphous alloy) or a kind of robust epoxy resin photoresist (i.e., SU-8) is used.

## 2. Experiment

**2.1. Chemicals and Materials.** Double-side anodized  $\text{Al}_2\text{O}_3$  (AAO) porous templates with pore sizes of 35 nm, 90 nm, and 200 nm were purchased from Synkera Technologies. Photoresist SU-8-2050 was purchased from MicroChem Inc. Platinum, copper, and nickel bulk with purity of 99.99% were purchased from Zhongnuo Advanced Material Company. Red phosphorus (99.99%) and 1,1,1,3,3,3-hexamethyldisilazane (HMDS) were purchased from Alfa Aesa. PMMA (polymethylmethacrylate) is purchased from Alibaba. Positive photoresist ILR-1050 was purchased from Research Semiconductor Company.

**2.2. Preparation of Pt-Based Bulk Amorphous Alloy.** The Pt-based amorphous plates ( $\phi 4 \text{ mm} \times 1 \text{ mm}$ ) were prepared by

cutting the Pt-based amorphous rods that were prepared by a rapid solidification process after pressing the molten alloy into a copper mold of diameter of 4 mm. An ingot with composition of  $\text{Pt}_{57.5}\text{Cu}_{14.7}\text{Ni}_{5.3}\text{P}_{22.5}$  (atom%) [23–25] was prepared, using a high-frequency induction melting (HFIM) process (NEW-ADR-05) in which bulk platinum, copper, nickel, and red phosphorus were melted together to produce an alloy. To ensure chemical and structural homogeneity and purification, the ingot was remelted 3–5 times with  $\text{B}_2\text{O}_3$  under Ar atmosphere in an arc melting furnace. Then, the ingot was remelted again and Pt amorphous rods with a diameter of 4 mm were prepared by copper mold casting process. These rods were cut into 1 mm thick pieces, which will be polished and cleaned in acetone, ethanol, and deionized water for further use.

**2.3. Template Transfer Process for the Fabrication of Nanopore Structures.** Figure 1 gives the scheme of the template transfer imprint process for the preparation of nanopore arrays using amorphous alloy as constructing materials. The AAO templates are firstly cleaned before using as follows: immersing in acetone for 15 mins and then in ethanol at  $70^\circ\text{C}$  for 15 mins, and then washing in deionized water, drying by  $\text{N}_2$  flow, and then placing in an oven at  $80^\circ\text{C}$  for 10 mins. Then, the Pt-based amorphous plate ( $\phi 4 \text{ mm} \times 1 \text{ mm}$ ) is pressed into the cleaned AAO template at the temperature higher than its  $T_g$  (glass transition temperature) but lower than its  $T_x$  (the initial crystallization temperature) under a certain pressure that can overcome the capillary forces (a). And then the AAO template and the amorphous plate are immersed in 35% KOH etching solution at  $80^\circ\text{C}$  for 30 mins to remove the AAO template, leading to the formation of nanorod arrays with desired diameter and interrod spacing (b). After that, the formed nanorod arrays can be used as master mold to form nanopore arrays again by hot embossing into a layer of polymer (e.g., positive photoresist ILR-1050 or SU-8) on substrates (c).

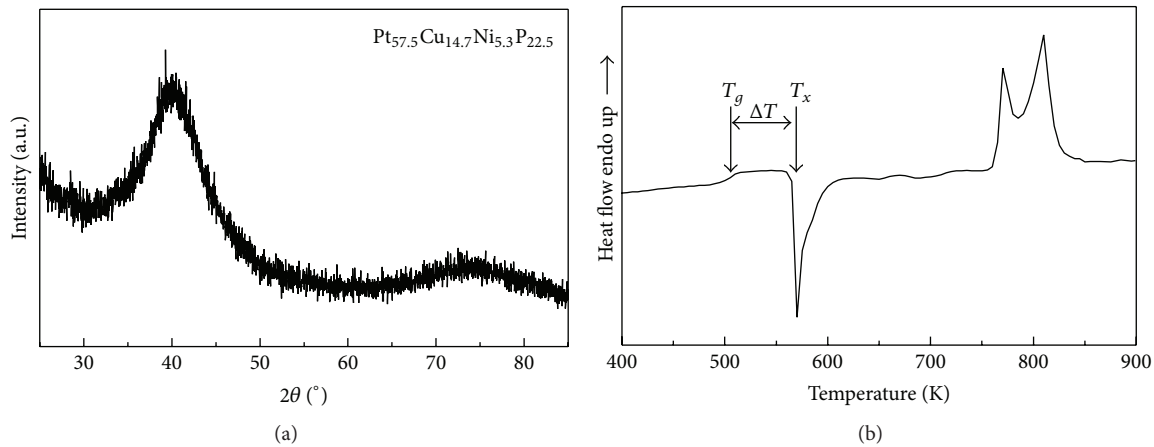


FIGURE 2: XRD pattern for the  $\text{Pt}_{57.5}\text{Cu}_{14.7}\text{Ni}_{5.3}\text{P}_{22.5}$  amorphous alloy (a); DSC curves for the  $\text{Pt}_{57.5}\text{Cu}_{14.7}\text{Ni}_{5.3}\text{P}_{22.5}$  bulk metallic glasses (b).

Finally, the bottom residues in nanopores after the master mold is released can be removed by oxygen plasma to obtain bottom clean nanopore arrays for further application (d). The Pt-based amorphous plate can be replaced by SU-8 based or PMMA based plate to fabricate nanorod arrays, which can also be used to prepare the nanopore structures.

### 3. Results and Discussion

In order to make sure the Pt-based alloy be in amorphous phase, X-ray diffraction (XRD) of the Pt-based alloy rods was performed. As shown in Figure 2(a), two broadly diffused peaks at  $41.0^\circ$  and  $74.8^\circ$  appear in the XRD pattern, indicating that amorphous  $\text{Pt}_{57.5}\text{Cu}_{14.7}\text{Ni}_{5.3}\text{P}_{22.5}$  alloy rods are prepared [23–25]. In order to find the suitable temperature range for the hot press process, the differential scanning calorimetry (DSC) is conducted. As shown in Figure 2(b), there is a typical glass transition at 502 K ( $T_g$ ) and the initial crystallization appears at 570 K ( $T_x$ ) for the amorphous  $\text{Pt}_{57.5}\text{Cu}_{14.7}\text{Ni}_{5.3}\text{P}_{22.5}$  alloy. Thus, the super cooled liquid region is about 68 K, which provides us with a wide enough temperature range to do the hot press.

In the template transfer process, the cleaned AAO template covered with Pt-based amorphous alloy plate is preheated at the temperature between  $T_g$  and  $T_x$  (i.e., 533 K). Then, pressure (80~130 MPa) is applied on the amorphous alloy plate and maintained about 60 seconds. And then the sample is removed from the oven and quenched in cold water. If the aspect ratio (length to diameter ratio:  $L/d$ ) of the nanorods is low ( $<7$ ), the amorphous alloy plate can be easily separated from the AAO template due to their different thermal coefficients (usually, Pt-based amorphous alloy is smaller than AAO). For high aspect ratio, the AAO template can be dissolved into hot concentrated KOH solution ( $80^\circ\text{C}$ , 35 wt%). It is found that the applied pressure is increased as the diameter of AAO template decreases. For example, the applied pressure is about 80 MPa for AAO templates with diameter of 200 nm and the pressure has to be increased up to 130 MPa for AAO templates with diameter of 35 nm.

Figure 3 gives the SEM images of the formed Pt-based amorphous alloy nanorod arrays transferred from AAO templates of different diameters. The nanorod arrays almost inherit the size and size distribution features of the nanopores. The diameter of nanorod arrays is about  $199.8 \pm 25.8$  nm if AAO templates with diameter of  $202.4 \pm 27.8$  nm are used (Figure 3(a)). The diameter of the nanorods is  $87.8 \pm 6.7$  nm if AAO templates with diameter of  $88.6 \pm 6.8$  nm are used (Figure 3(c)). The diameter of nanorod arrays is about  $32.0 \pm 2.3$  nm if AAO templates with diameter of  $34.8 \pm 2.4$  nm are used (Figure 3(e)). As observed from the angle-tilt image of some nanorod arrays (Figure 3(b) and inset of Figure 3(d)), the aspect ratio can reach about 5-6, indicating that the  $\text{Pt}_{57.5}\text{Cu}_{14.7}\text{Ni}_{5.3}\text{P}_{22.5}$  amorphous alloy has good super-plastic forming ability in its cooled liquid region, which endows it excellent filling ability even in very small pores.

We also try to obtain thermosetting polymer nanorod arrays using AAO template transfer process in which a kind of UV curing epoxy resin (i.e., SU-8) or PMMA plates is used as constructing materials [26, 27]. If using PMMA plates as construction materials, the similar process as using Pt-based amorphous alloys can be performed for the PMMA nanorod arrays, only by adjusting the imprinting temperature to  $160^\circ\text{C}$  and the imprinting pressure at about 25 MPa. If using liquid SU-8 resin, the process is followed below. The liquid SU-8 resin of 0.5~1 mm thick is spin-coated on the glass substrate and dried by heating at  $90^\circ\text{C}$  for 35 mins, respectively. Then the SU-8 resin is placed on the AAO template and pressure gradually up to 1.5 MPa is applied on the substrate and is maintained for 5 mins. After that, the sample is exposed under UV-light for 10 mins and thermal-cured at  $90^\circ\text{C}$  for 35 mins to complete cross-linking. Finally, the AAO template is removed by dissolving into 35 wt% KOH solution or peeled mechanically to obtain nanorod arrays made of highly cross-linked SU-8 resin. Figures 4(a) and 4(b) give the SEM images of nanorod arrays made of SU8 resin transferred from AAO template pore diameter of  $82.4 \pm 3.4$  nm. The diameter of these nanorods is about  $82.1 \pm 3.2$  nm, almost the same as that of the AAO template. Figures 4(c) and 4(d) give the SEM

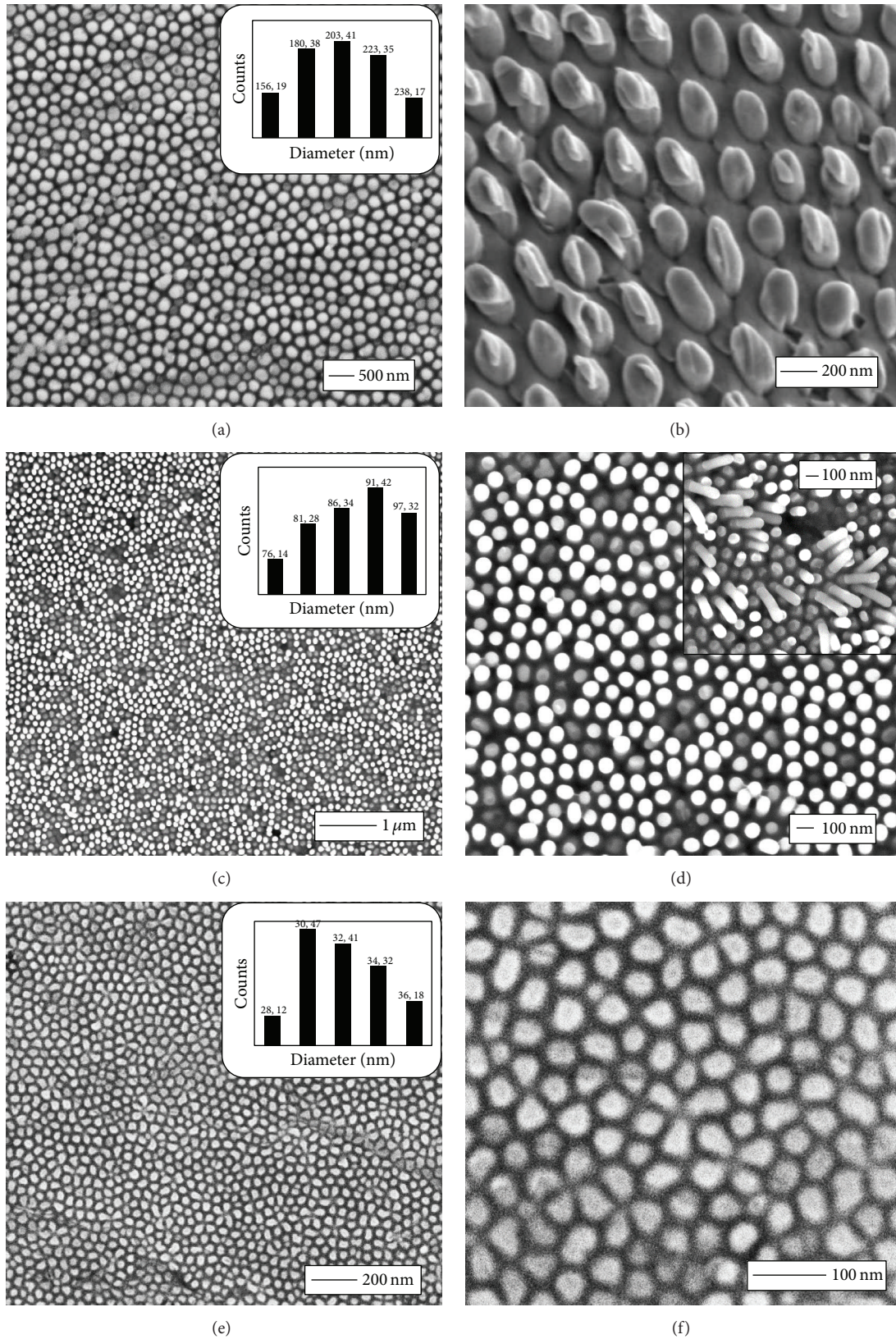


FIGURE 3: SEM images of the Pt-based amorphous nanorods arrays prepared from AAO template with different diameters. (a) and (b):  $202.4 \pm 27.8$  nm; (c) and (d):  $88.6 \pm 6.8$  nm; (e) and (f):  $34.8 \pm 2.4$  nm. The insets in (a), (c), and (e) give the diameter histograms of nanorods. (b), (d), and (f) are the magnified local images or angle-tilt images of these nanorods.

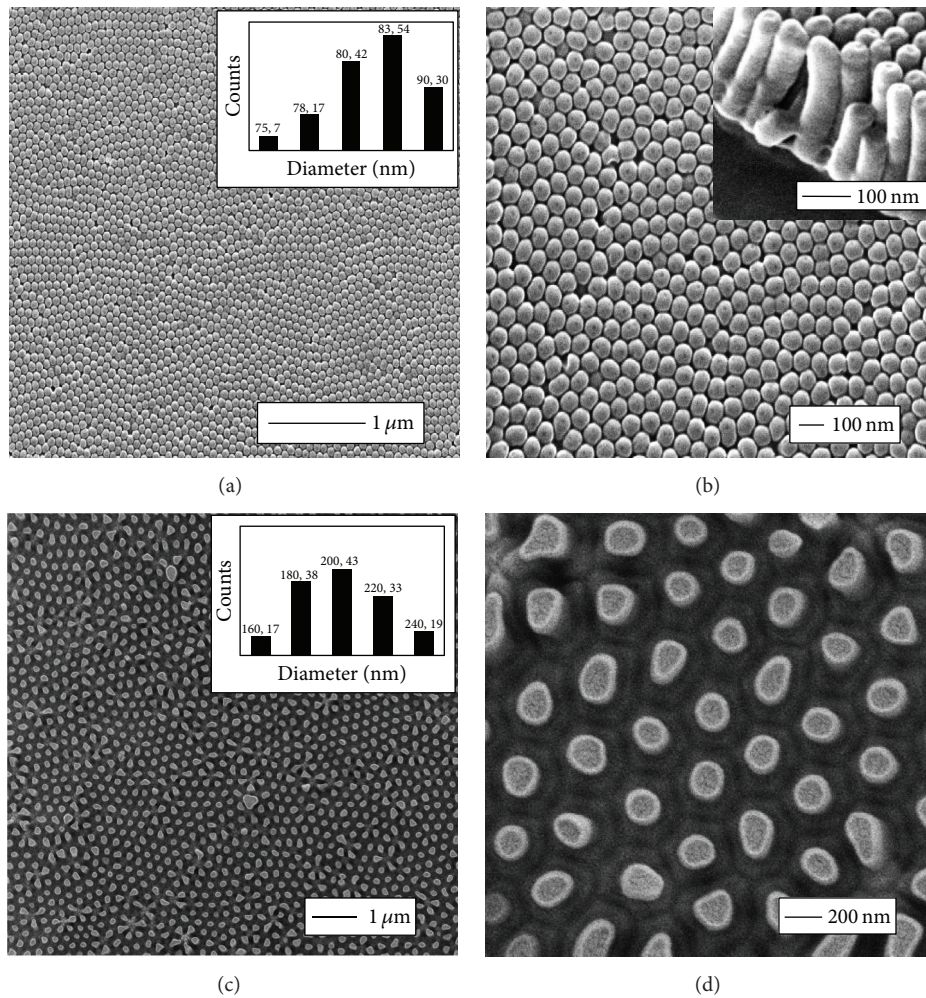


FIGURE 4: SEM images of the nanorod arrays of SU-8 resin transferred from the AAO template with pore diameter of  $82.4 \pm 3.4$  nm ((a) and (b)). The inset is the magnified local images of these nanorods. SEM images of the nanorod arrays of PMMA transferred from the AAO template with pore diameter of  $198.7 \pm 31.5$  nm ((c) and (d)).

images of nanorod arrays made of PMMA plate transferred from AAO template pore diameter of  $202.4 \pm 25.4$  nm. The diameter of these nanorods is about  $198.7 \pm 31.5$  nm. The side view of SU-8 nanorod arrays gives an aspect ratio about 6, indicating that the SU-8 resin has a good filling ability.

The nanopore films can be further prepared using these nanorod arrays as master molds. The fabrication procedure using Pt-based nanorod arrays as master molds is demonstrated as below. The HMDS of about 100–200 nm (used as tackifier) and the positive photoresist ILR-1050 resin of about 300~400 nm are spin-coated on the Si wafer successively. Then, the Si wafer with these resins is heated at  $100^\circ\text{C}$  for 30 mins. After that, a Pt-based amorphous alloy plate with nanorod arrays is placed on the dry ILR-1050 resin and heated to  $140^\circ\text{C}$  (just above  $T_g$  of ILR-1050 resin). Then, pressure about 15~20 MPa is applied on the Pt-based amorphous plate for 20 mins. And then, the Pt-based amorphous alloy master mold and the ILR-1050 resin are gradually cooled to room temperature by conventional air flow and the Pt-based

amorphous alloy master mold is released from the ILR-1050 resin mechanically. Finally, the surface of the nanopore arrays made of ILR-1050 resin is cleaned by oxygen plasma and the shallow nanopore arrays are obtained. Figures 5(a) and 5(b) give typical SEM images of the nanopore arrays fabricated by diameter of  $88.6 \pm 6.8$  nm Pt-based amorphous alloy nanorod arrays; Figures 5(c) and 5(d) give typical SEM images of the nanopore arrays fabricated by diameter of  $198.7 \pm 31.5$  nm PMMA nanorod arrays. The insets in Figures 5(a) and 5(c) show that the diameters of the nanopores are about  $94.5 \pm 12.2$  nm and  $207 \pm 26.4$  nm, which are slightly larger than those of nanorods due to the oxygen plasma cleaning and the thermal expansion effect of nanorods at high temperature. These shallow nanopore arrays have great potentials for the ultra-sensitive biosensing after further treatment (chemical functionalization of solid-state nanopores and nanopore arrays and applications thereof) [28] or as masks for deep nanoholes. Nanoparticle arrays can be further fabricated using these nanopore films as templates again. Control

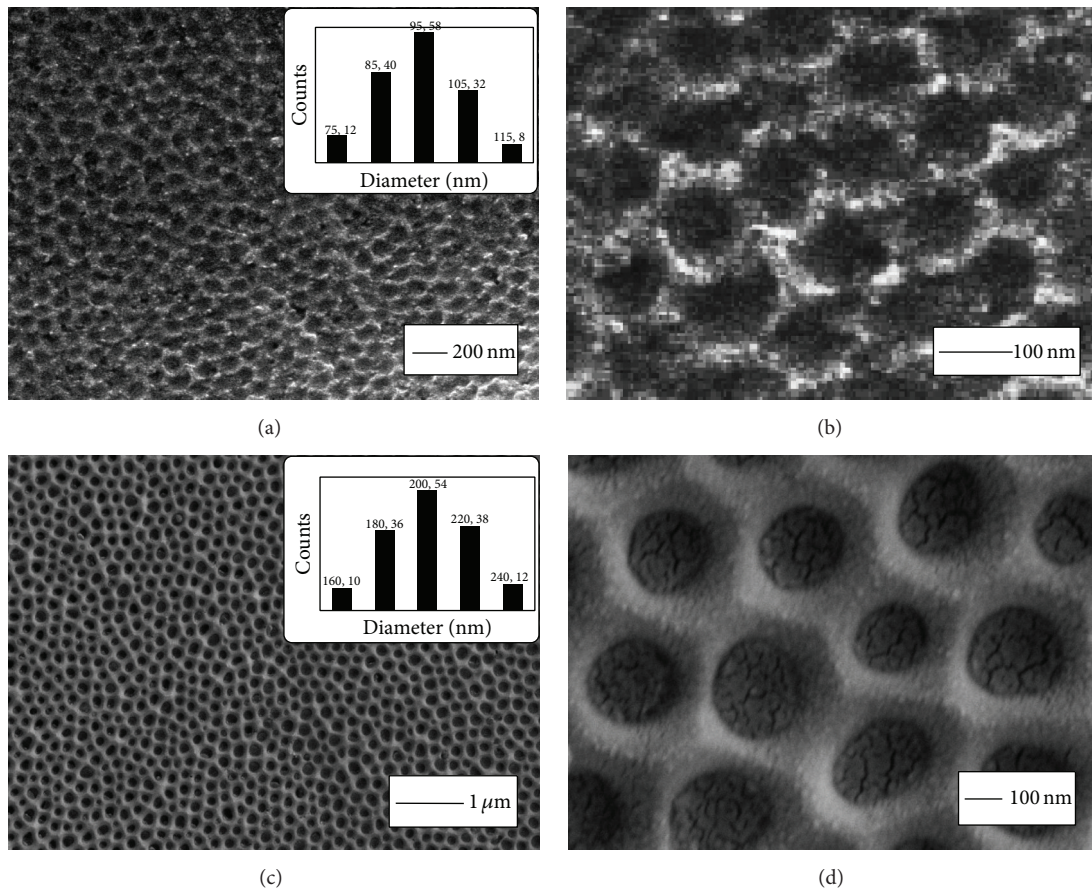


FIGURE 5: SEM image of the type ILR-1050 photoresist nanopore arrays prepared from Pt-based nanorod arrays. (a) and (b):  $94.5 \pm 12.2$  nm. SEM image of the SU-8 photoresist nanopore arrays prepared from PMMA-based nanorod arrays. (c) and (d):  $207 \pm 26.4$  nm. The insets in (a) and (c) give the diameter histograms of nanopores. (b) and (d) are the magnified local images of these nanopores.

of the depth of these nanopores is in progress by tuning the fabrication conditions (e.g., imprinting pressure and temperature, sizes, and interspacing of nanorod arrays).

#### 4. Conclusions

The nanorod arrays made of Pt-based amorphous alloys or UV-curing thermosetting epoxy resin are successfully fabricated using AAO template transfer process. Using these nanorod arrays as master molds, the nanopore arrays can be successively transferred into another kind of material, such as ILR-1050 resin on Si wafers (or SU-8 resin on glass slides). This method is suitable for the preparation of shallow nanopore arrays on substrate. This newly developed process enables large-scale fabrication of uniform nanostructures (nanopores or nanorods) based on the template transfer process in which both robust metallic amorphous alloys and thermosetting polymers can be used as constructing materials of master molds.

#### Conflict of Interests

The authors declare that there is no conflict of interests regarding the publication of this paper.

#### Acknowledgments

This work was supported by NSFC (Grant no. 51371018) and the Fundamental Research Funds for the Central Universities (FRF-BR-15-027A and FRF-BR-14-001B).

#### References

- [1] C. L. Haynes and R. P. Van Duyne, "Nanosphere lithography: a versatile nanofabrication tool for studies of size-dependent nanoparticle optics," *Journal of Physical Chemistry B*, vol. 105, no. 24, pp. 5599–5611, 2001.
- [2] Y. Song and H. E. Elsayed-Ali, "Aqueous phase Ag nanoparticles with controlled shapes fabricated by a modified nanosphere lithography and their optical properties," *Applied Surface Science*, vol. 256, no. 20, pp. 5961–5967, 2010.
- [3] G. W. Meng, Y. J. Jung, A. Y. Cao, R. Vajtai, and P. M. Ajayan, "Controlled fabrication of hierarchically branched nanopores, nanotubes, and nanowires," *Proceedings of the National Academy of Sciences of the United States of America*, vol. 102, no. 20, pp. 7074–7078, 2005.
- [4] M. A. S. Chong, Y. B. Zheng, H. Gao, and L. K. Tan, "Combinational template-assisted fabrication of hierarchically ordered nanowire arrays on substrates for device applications," *Applied Physics Letters*, vol. 89, no. 23, Article ID 233104, 2006.

- [5] I. Lombardi, P. L. Cavallotti, C. Carraro, and R. Maboudian, "Template assisted deposition of Ag nanoparticle arrays for surface-enhanced Raman scattering applications," *Sensors and Actuators, B: Chemical*, vol. 125, no. 2, pp. 353–356, 2007.
- [6] Y. Song, W. Yin, Y.-H. Wang et al., "Magneto-plasmons in periodic nanoporous structures," *Scientific Reports*, vol. 4, article 4991, 2014.
- [7] S. Y. Chou, C. Keimel, and J. Gu, "Ultrafast and direct imprint of nanostructures in silicon," *Nature*, vol. 417, no. 6891, pp. 835–837, 2002.
- [8] G. Kumar, H. X. Tang, and J. Schroers, "Nanomoulding with amorphous metals," *Nature*, vol. 457, no. 7231, pp. 868–872, 2009.
- [9] S. Zankovych, T. Hoffmann, J. Seekamp, J.-U. Bruch, and C. M. Sotomayor Torres, "Nanoimprint lithography: challenges and prospects," *Nanotechnology*, vol. 12, no. 2, pp. 91–95, 2001.
- [10] M. T. Rahman, H. Wang, and J.-P. Wang, "Exploration of the direct use of anodized alumina as a mold for nanoimprint lithography to fabricate magnetic nanostructure over large area," *Journal of Nanotechnology*, vol. 2011, Article ID 961630, 5 pages, 2011.
- [11] K. O. Aung, C. Shankaran, R. Sbiaa, E. L. Tan, S. K. Wong, and S. N. Piramanayagam, "Achieving high aspect ratio of track length to width in molds for discrete track recording media," *Research Letters in Nanotechnology*, vol. 2008, Article ID 765398, 4 pages, 2008.
- [12] B. Ai, Y. Yu, H. Möhwald, G. Zhang, and B. Yang, "Plasmonic films based on colloidal lithography," *Advances in Colloid and Interface Science*, vol. 206, pp. 5–16, 2014.
- [13] Y. Song, "Fabrication of multi-level 3-dimension microstructures by phase inversion process," *Nano-Micro Letters*, vol. 2, no. 2, pp. 95–100, 2010.
- [14] W. Li, L. Xu, W.-M. Zhao, P. Sun, X.-F. Huang, and K.-J. Chen, "Fabrication of large-scale periodic silicon nanopillar arrays for 2D nanomold using modified nanosphere lithography," *Applied Surface Science*, vol. 253, no. 22, pp. 9035–9038, 2007.
- [15] F. Zhang, J. Chan, and H. Y. Low, "Biomimetic, hierarchical structures on polymer surfaces by sequential imprinting," *Applied Surface Science*, vol. 254, no. 10, pp. 2975–2979, 2008.
- [16] X. Yang, S. Xiao, Y. Hsu, M. Feldbaum, K. Lee, and D. Kuo, "Directed self-assembly of block copolymer for bit patterned media with areal density of 1.5 Teradot/Inch<sup>2</sup> and beyond," *Journal of Nanomaterials*, vol. 2013, Article ID 615896, 17 pages, 2013.
- [17] M. Okada, H. Miyake, S. Iyoshi et al., "Double patterning in nanoimprint lithography," *Microelectronic Engineering*, vol. 112, pp. 139–142, 2013.
- [18] Y. Shen, L. Yao, Z. Li et al., "Double transfer UV-curing nanoimprint lithography," *Nanotechnology*, vol. 24, no. 46, Article ID 465304, 2013.
- [19] Y. J. Song, C. S. S. R. Kumar, and J. Hormes, "Fabrication of an SU-8 based microfluidic reactor on a PEEK substrate sealed by a 'flexible semi-solid transfer' (FST) process," *Journal of Micromechanics and Microengineering*, vol. 14, no. 7, pp. 932–940, 2004.
- [20] J. Schroers, "Processing of bulk metallic glass," *Advanced Materials*, vol. 22, no. 14, pp. 1566–1597, 2010.
- [21] S. Mridha, D. L. Jaeger, H. S. Arora, R. Banerjee, and S. Mukherjee, "Atomic distribution in catalytic amorphous metals," *Journal of Nanomaterials*, vol. 2015, Article ID 632138, 7 pages, 2015.
- [22] D. R. Barbero, M. S. M. Saifullah, P. Hoffmann et al., "High resolution nanoimprinting with a robust and reusable polymer mold," *Advanced Functional Materials*, vol. 17, no. 14, pp. 2419–2425, 2007.
- [23] B. A. Legg, J. Schroers, and R. Busch, "Thermodynamics, kinetics, and crystallization of Pt<sub>57.3</sub>Cu<sub>14.6</sub>Ni<sub>5.3</sub>P<sub>22.8</sub> bulk metallic glass," *Acta Materialia*, vol. 55, no. 3, pp. 1109–1116, 2007.
- [24] J. Schroers, "On the formability of bulk metallic glass in its supercooled liquid state," *Acta Materialia*, vol. 56, no. 3, pp. 471–478, 2008.
- [25] J. Schroers, B. Lohwongwatana, W. L. Johnson, and A. Peker, "Precious bulk metallic glasses for jewelry applications," *Materials Science and Engineering A*, vol. 448–451, pp. 235–238, 2007.
- [26] M. Aryal, F. Buyukserin, K. Mielczarek et al., "Imprinted large-scale high density polymer nanopillars for organic solar cells," *Journal of Vacuum Science & Technology B*, vol. 26, no. 6, pp. 2562–2566, 2008.
- [27] F. Buyukserin, M. Aryal, J. M. Gao, and W. C. Hu, "Fabrication of polymeric nanorods using bilayer nanoimprint lithography," *Small*, vol. 5, no. 14, pp. 1632–1636, 2009.
- [28] A. Meller and M. Wanunu, "New chemical functionalization of solid-state nanopore, useful for characterizing an analyte, identifying a biomolecule, sensing a chemical environmental, detecting biopolymers, immobilizing enzymes, and localized pH sensing," US Patent: US 9121843-B2, 2015.